


July 2019

Modulating Dopant-Defect Interactions in Transition Metal Doped Colloidal Strontium Titanate Nanocrystals

William Harrigan

Follow this and additional works at: https://scholarworks.umass.edu/dissertations_2

 Part of the [Inorganic Chemistry Commons](#), [Materials Chemistry Commons](#), and the [Physical Chemistry Commons](#)

Recommended Citation

Harrigan, William, "Modulating Dopant-Defect Interactions in Transition Metal Doped Colloidal Strontium Titanate Nanocrystals" (2019). *Doctoral Dissertations*. 1623.
https://scholarworks.umass.edu/dissertations_2/1623

This Open Access Dissertation is brought to you for free and open access by the Dissertations and Theses at ScholarWorks@UMass Amherst. It has been accepted for inclusion in Doctoral Dissertations by an authorized administrator of ScholarWorks@UMass Amherst. For more information, please contact scholarworks@library.umass.edu.

**MODULATING DOPANT-DEFECT INTERACTIONS IN TRANSITION METAL
DOPED COLLOIDAL STRONTIUM TITANATE NANOCRYSTALS**

A Dissertation Presented

by

WILLIAM LOUIS HARRIGAN

Submitted to the Graduate School of the
University of Massachusetts Amherst in partial fulfillment
of the requirements for the degree of

DOCTOR OF PHILOSOPHY

May 2019

Department of Chemistry

© Copyright by William Louis Harrigan 2019

All Rights Reserved

**MODULATING DOPANT-DEFECT INTERACTIONS IN TRANSITION METAL
DOPED COLLOIDAL STRONTIUM TITANATE NANOCRYSTALS**

A Dissertation Presented

by

WILLIAM LOUIS HARRIGAN

Approved as to style and content by:

Kevin R. Kittilstved, Chair

Richard W. Vachet, Member

Sankaran Thayumanavan, Member

Wei Fan, Member

Richard W. Vachet, Department Head
Department of Chemistry

DEDICATION

To my family and friends who have provided their endless support through the years.

ACKNOWLEDGMENTS

My journey through graduate school has been quite a trip and I would not have made it this far without the support of so many people. I would like to first and foremost thank my advisor Professor Kevin R. Kittilstved for his patience, guidance, and support during my time here, both inside and outside of the lab. I am very grateful for everything he has done.

I would also like to thank my other committee members Prof. Richard W. Vachet, Prof. Sankaran Thayumanavan and Prof. Wei Fan for their support and guidance throughout this process. I appreciate all of their efforts in helping me arrive to this point.

I want to thank the members of Kevin's research group both past and present for their support during my time at UMASS. Whether it was a 24-hour MCD run or a late-night practice prospectus talk, it was a lot of fun. I would like to especially thank former members, Kim-Ngan Hua, Swamy Pittala, Keith Lehuta, Dongming Zhou and Jenileigh Harris for everything they've taught me and have done for me. I would like to thank my undergraduate student Sam Michaud, who has worked alongside me for a few years and has helped tremendously during my time at UMASS. I would also like to thank the current members of Kevin's group. I would like to thank Fumitoshi Kato for being someone who can provide interesting conversations at the drop of a hat and Jillian Denhardt for providing some comedic relief when things got stressful, without even trying. The three of us had a lot of fun whether it was grabbing a beer on a random Friday night, going to dinner to celebrate someone's birthday or going on our annual hike. I would also like to thank Haneen Mansoor and Enes Buz for their continuous support and an open ear to listen.

I would like to thank the different collaborators I had the opportunity to work with while I was at UMASS. It was really fun and a great experience working with Satyan Choudhary from Alfred J. Crosby's group in the polymer science department and Jiaying Wang from Stephen S. Nonnenmann's group in the chemical engineering department. I would also like to thank Mark Turnbull from Clark University for providing access to their PXRD when ours would inevitably break down. I would also like to thank Elizabeth Young originally at Amherst college for allowing me to use the electrochemical equipment and transient absorption spectrometer. I would also like to thank Rafael Cassaro, a post-doc. from Prof. Paul Lahti's research group for imparting his EPR knowledge to me.

Finally, I would like to give thanks to the NSF funding (DMR-1747593) for supporting my research.

My family has been enormously supportive of me throughout this process. I am extremely grateful for everything they've done and continue to do. I would not be the person I am today without their guidance, love, and support. I would like to thank my dad for always encouraging me to do the best that I can, without killing myself in the process. I would like to thank my sister who always lets me know how proud she is of what I'm doing, whenever we talk. I also would like to thank my aunt Bernadette and aunt Doreen for being there when I needed it the most or offering their great and quiet three season room to work remotely, peacefully. I would lastly like to take this moment to give a special thanks to two very important people in particular who started this journey with me but could not be here to see this accomplishment. I want to thank my mom for her never-ending positivity and always going above and beyond for me and my aunt Mary for always knowing what to do or say to make me feel better and to never give up.

Lastly, I would like to thank all of my friends for being a fantastic support system for me through graduate school. I would not have been able to do this without all of their great influences. I would especially like to thank my best friends Amina Oluwo, Joe Leonardi and Vanessa Castro along with her two daughters, Sophia, and Renee for sticking with me through thick and thin. I couldn't have asked for better friends. I would like to thank last, but not least a really good friend of mine Erin Phillips, for always unconditionally offering her support whenever I would need it. I truly and deeply appreciate all my friends have done for me.

ABSTRACT

MODULATING DOPANT-DEFECT INTERACTIONS IN TRANSITION METAL DOPED COLLOIDAL STRONTIUM TITANATE NANOCRYSTALS

MAY 2019

WILLIAM LOUIS HARRIGAN, B.S., BINGHAMTON UNIVERSITY

Ph.D., UNIVERSITY OF MASSACHUSETTS AMHERST

Directed by: Professor Kevin R. Kittilstved

Perovskites such as strontium titanate, a wide band gap semiconductor have been widely studied due to the multitude of potential applications in photocatalysis, multiferroics, sensing, and microelectronics. Various novel optical, electrical and magnetic properties can be imparted through the introduction of different transition metal dopant ions. The introduction of these impurities has been shown to impart functionality for various applications. The use of Cr^{3+} has been shown to introduce defect levels into the band structure of SrTiO_3 and increase visible light utilization for photocatalysis. Transition metal doped highly crystalline colloidal SrTiO_3 nanocrystals (NC) were synthesized using two modified hydrothermal (HT) synthesis methods and subsequently characterized. Structural characterization techniques such as powder X-ray diffraction (XRD), tunneling electron microscopy (TEM) and high-resolution tunneling electron microscopy (HR-TEM) proved vital in confirming the successful synthesis of highly crystalline sub-10 nm nanocubes. The use of transition metal doped colloidal nanocrystals will look to better understand dopant incorporation and subsequent defect formation and their interactions on the nm scale.

The use of dopant specific spectroscopies such as electron paramagnetic resonance (EPR) spectroscopy was crucial in determining both the transition metal dopant oxidation state and dopant position in the colloidal NCs. Through the use of EPR spectroscopy the dopants and defects were unambiguously identified and characterized. Various surface related oxygen defects were identified and correlated to emerge under specific synthetic conditions. Site-selective internal doping of Cr or Mn was achieved through either modified HT methods.

The extent of the dopant-defect interactions was studied using a photodoping technique. Under anaerobic conditions and in the presence of a hole quencher, the interactions of the photoinduced electron with SrTiO₃ were monitored. The photoinduced changes were tracked using electronic absorption spectroscopy and EPR spectroscopy. An in-depth EPR analysis showed the photoinduced electron localizes on titanium atoms and undergoes cross relaxation with neighboring Cr ions.

TABLE OF CONTENTS

	Page
ACKNOWLEDGMENTS	v
ABSTRACT	viii
LIST OF TABLES	xii
LIST OF FIGURES	xiii
 CHAPTER	
1. INTRODUCTION INTO PEROVSKITE BASED MATERIALS AND THEIR	
MULTIFUNCTIONALITY	1
1.1. Introduction to spintronics	1
1.2. Spin relaxation processes	3
1.3. Strontium Titanate: Perovskite basics	4
1.4. Types of lattices and synthesis methods	5
1.5. The impact of doping in SrTiO ₃	6
1.6. Colloidal SrTiO ₃ nanocrystals	7
1.7. References.....	8
2. TUNABLE ELECTRONIC STRUCTURE AND SURFACE DEFECTS IN	
CHROMIUM-DOPED STRONTIUM TITANATE NANOCRYSTALS	15
2.1. Introduction.....	15
2.2. Experimental Methods	17
2.3. Results and Discussion	19

2.4. Conclusions.....	27
2.5. Supplementary Information	27
2.6. References.....	32
3. REVERSIBLE CONTROL OVER THE MANGANESE OXIDATION STATE IN COLLOIDAL STRONTIUM TITANATE NANOCRYSTALS.....	36
3.1. Introduction.....	36
3.2. Experimental Methods	37
3.3. Results and Discussion	39
3.4. Conclusions.....	47
3.5. References.....	48
4. REVERSABLE MODULATION OF THE Cr ³⁺ SPIN DYNAMICS IN COLLOIDAL SrTiO ₃ NANOCRYSTALS	52
4.1. Introduction.....	52
4.2. Results and Discussion	54
4.3. Conclusions.....	65
4.4. Supplementary Information	66
4.5. References.....	71
5. CONCLUSIONS AND FUTURE DIRECTIONS	75
BIBLIOGRAPHY.....	80

LIST OF TABLES

Table	Page
2.1 Comparison of measured Cr content (x) for $\text{Sr}(\text{Ti}_{1-x}\text{Cr}_x)\text{O}_{3-\delta}$ NCs prepared by methods A and B as a function of varying nominal x	32
4.1 Temperature dependence of the spin-spin relaxation time (T_2) using the deconvoluted Lorentzian width from fitting each CW EPR spectra to a first derivative pseudo-Voigt line profile.	70

LIST OF FIGURES

Figure	Page
1.1 Schematic representation of the spin based electronic devices.	2
1.2 Structural depiction of SrTiO ₃ . The Sr ²⁺ ions (blue) occupy the corners. The Ti ⁴⁺ (green) lies in the center of and octahedra of O ²⁻ ions (orange)....	5
1.3 Schematic representation of the doping process. Dopant incorporation can lead to novel optical, magnetic and electrical properties.....	7
2.1 Room temperature electronic absorption spectra of (a) concentrated and (b) dilute suspensions of SrTiO _{3-δ} - A (thin lines) and SrTiO _{3-δ} - B (thick lines) NCs in hexanes. (b) Uncorrected emission spectra (dashed) excited at 300 nm.	20
2.2 Room-temperature electronic absorption spectra of concentrated Sr(Ti _{1-x} Cr _x)O _{3-δ} suspensions prepared by (a) method A and (b) method B. The nominal Cr content is $x = 0$ (dashed) and $x = 0.1\%$ (solid). Color photos of SrTiO _{3-δ} and Sr(Ti _{1-x} Cr _x)O _{3-δ} colloidal suspensions are shown in the right panels.	21
2.3 Variable-temperature emission spectra of Sr(Ti _{1-x} Cr _x)O _{3-δ} ($x_{\text{nom}} = 0.1\%$) NCs prepared by (a) method A and (b) method B . Note that the energy scale changes at 1.65 eV in order to show the Cr ³⁺ PL on an expanded energy scale. The intensity scale, however, is not scaled in the different panels except for the 14.1 K and 152 K spectra in (b) that are also shown scaled by 5. Samples were excited by the 488 nm line of an Ar-ion laser.....	23
2.4 Room-temperature X-band EPR spectra of (a) Sr(Ti _{1-x} Cr _x)O _{3-δ} - A and (b) Sr(Ti _{1-x} Cr _x)O _{3-δ} - B with $x = 0$ (dashed line) and 0.01% (solid line)..	26
2.5 Powder X-ray diffraction patterns of SrTiO _{3-δ} - B (top) and nominally 0.1% Sr(Ti _{1-x} Cr _x)O _{3-δ} - B (bottom). The grain sizes estimated from the Scherrer equation are 15 nm for SrTiO _{3-δ} - B and 9 nm for nominally 0.1% Sr(Ti _{1-x} Cr _x)O _{3-δ} - B . Red lines indicate the powder pattern of bulk SrTiO ₃	28
2.6 Representative TEM images of (a) SrTiO _{3-δ} - A and (b) SrTiO _{3-δ} - B NCs. (c) Particle size distribution and (d) aspect ratios obtained from analysis of TEM data for SrTiO _{3-δ} - A and SrTiO _{3-δ} - B	29

2.7 (a) Representative high-resolution TEM image and (b) rectangular color profile of the Sr(Ti _{1-x} Cr _x)O _{3-δ} - B NC shown in (a). The analysis was performed by first rotating the image so that the lattice fringes are vertical and then using the “plot profile” analysis function in ImageJ software on a rectangle encompassing the entire nanocrystal. The average lattice spacing is 2.76 ± 0.08 Å and agrees well with the 2.76 Å d-spacing of the (110) plane of SrTiO ₃	30
2.8 Variable-temperature photoluminescence spectrum of (a) Sr(Ti _{1-x} Cr _x)O _{3-δ} - A and (b) Sr(Ti _{1-x} Cr _x)O _{3-δ} - B NC powders. The spectra were collected with 488-nm laser excitation and the emitted light was detected using a Fourier transform (FT) spectrometer with 488 nm and 633 nm notch filters. The 633 nm notch filter is to remove laser emission from the HeNe alignment laser of the FT spectrometer.	30
2.9 Low-temperature ² E→ ⁴ A ₂ emission Sr(Ti _{1-x} Cr _x)O _{3-δ} - B nanocrystal powders as a function of nominal Cr content, x. Excitation was the 488 nm line from an Ar ⁺ ion laser (JDS Uniphase). The literature emission from a 0.001% Cr ³⁺ -doped SrTiO ₃ single crystal at 20.4 K is included for comparison.	31
2.10 Comparison of the relative PL intensities of the visible STE emission for Sr(Ti _{1-x} Cr _x)O _{3-δ} - B NCs with nominal values of x = 0.1% and 0.5%. The intensities of the ² E→ ⁴ A ₂ transition for the two spectra are normalized. The broad STE-related emission from the undoped SrTiO _{3-δ} - B NC population in the ensemble is significantly reduced with the increase in nominal Cr ³⁺ concentration. Excitation was the 488 nm line from an Ar ⁺ ion laser (JDS Uniphase). Sample temperatures are given in figure.....	31
2.11 Room-temperature EPR spectra of “Cr ₂ O ₃ ” and Sr(Ti _{1-x} Cr _x)O _{3-δ} - A nanocrystals where nominal x = 0.01% (dotted line) and 1% (solid line). The linewidth is much broader in “Cr ₂ O ₃ ” from the antiferromagnetically-coupled Cr ³⁺ ions.	32
3.1 Powder X-ray diffraction pattern of as prepared-0.1% Mn-SrTiO ₃ . Particle sizes calculated from the Scherrer equation yield ~ 8 nm particles. (b) The HRTEM indicates ~ 7 nm cubic nanocrystals. (c) Fast Fourier transform (FFT) displaying the (111), (211) and (222) planes with measured d-spacings of 2.2 Å, 1.6 Å, and 1.1 Å respectively. (d) The rectangular color plot profile analysis performed in ImageJ is shown in (b). The calculated interplanar spacings 2.20 ± 0.02 Å agrees well with 2.25 Å, the d-spacing of the (111) plane.	40
3.2 Concentrated electronic absorption spectra of 0.1% Mn:SrTiO ₃ method A and B colloidal NCs. The broad absorption into the visible region in B is due to various oxygen related defects.	41
3.3 Room temperature EPR of two sets of synthesized method A and B, Mn:SrTiO ₃ samples. A ₁ and B ₁ were measured immediately after being synthesized. A ₂ and B ₂ were measured a week after being synthesized and stored in ambient light.	43

3.4 Room temperature EPR of colloidal as prepared and after photoirradiation, (a) A ₁ and B ₁ (b) A ₂ and B ₂ . Each sample was irradiated with a 75 W lamp for 3 hours and then measured immediately.	44
3.5 Photo-reversibility of Mn:SrTiO ₃ -A ₁ in both light and dark conditions. The sample was left in the dark for 7 days and then measured.	45
3.6 Room temperature EPR spectra of colloidal Mn ²⁺ :SrTiO ₃ -A ₁ (top). EPR spectra of colloidal Mn ²⁺ :SrTiO ₃ -A ₁ at 120 K (bottom). Impurities from the cryostat at low temperatures are marked with an asterisk.....	46
3.7 Room temperature EPR spectra of 0.1% Mn:SrTiO ₃ bulk powders reduced at 300° C using NaBH ₄ as a reductant (top). Photo-irradiated 0.1% Mn:SrTiO ₃ -A ₁ NCs (bottom)..	47
4.1 Electronic absorption spectra of air-free (a) SrTiO ₃ and (b) 0.1% Cr:SrTiO ₃ suspensions in hexane collected after different UV irradiation times. The spectra collected before irradiation (black line), and after irradiation at 0.05 <i>t_f</i> (blue line) and <i>t_f</i> (purple line) are highlighted by colors. The spectra taken after reopening the cuvette to air is also shown (dashed red line). The <i>t_f</i> is arbitrarily defined as the time needed for the MMCT transition to reach an optical density equal to 0.87.	55
4.2 Room-temperature EPR spectra of 0.1% Cr:SrTiO ₃ NCs in hexanes before (red) and after anaerobic photodoping (black), and after reoxidation (purple). Corresponding color photographs of representative Cr:SrTiO ₃ samples in EPR tubes is included to the right of each EPR spectra.....	57
4.3 Variable-temperature EPR spectra collected on photodoped 0.1% Cr:SrTiO ₃ NCs and 4.2 K spectrum of photodoped SrTiO ₃ NCs. The spectra for photodoped Cr:SrTiO ₃ were collected first at 295 K (red), and then decreased to 130 K (green) and 77 K (blue) followed by warming the sample again to 295 K (black dotted).	58
4.4 Representative CW-EPR spectra of (a) as-prepared Cr:SrTiO ₃ , (b) photodoped SrTiO ₃ , and (c) photodoped Cr:SrTiO ₃ NCs at 4.2 K (frozen suspension) and selected microwave powers. Definitions for the signal intensities for the different EPR-active species in the different sets of spectra are included graphically in the panels.....	60
4.5 Normalized CW-EPR intensities (ΔY or $ Y $) as a function of incident microwave power (h_1) at 4.2 K for Cr ³⁺ (red) and Ti ³⁺ (blue) EPR signals in the following samples: Cr ³⁺ in as-prepared Cr:SrTiO ₃ (empty circles), Ti ³⁺ in photodoped SrTiO ₃ (empty squares), and the Cr ³⁺ and Ti ³⁺ signals in photodoped Cr:SrTiO ₃ (filled circles and squares, respectively). The dashed curves through the data points are best fits to eq 1a (shaded regions are error bars on the fits).....	62

4.6 Temperature dependence of P_2 , for Cr^{3+} (circles) and Ti^{3+} (squares) in before (open) and after (filled) photodoping either $\text{Cr}:\text{SrTiO}_3$ or SrTiO_3 NCs. Both signals have an increase in the spin dynamics overall relaxation rates increase when Ti^{3+} is present in the lattice. Lines are guides to the eye.	63
4.7 Mid IR spectra of UD STO-A before and after photo-irradiation. There is no change in the absorption spectra after irradiating the sample in a KBr demountable cell with a 0.05 mm path length using a 1000 W lamp for 1 hr.	67
4.8 EPR spectra of AP-nominal 0.1% $\text{Cr}:\text{SrTiO}_3$ as a function of temperature. The inset shows the temperature dependence of the total peak to peak line width.	68
4.9 EPR spectra of photodoped undoped SrTiO_3 showing the Ti^{3+} signal as a function of temperature. The inset shows the temperature dependence of the total peak to peak line width.	68
4.10 EPR spectra of 0.1% $\text{Cr}:\text{SrTiO}_3$ NCs collected at 4.2 K before photodoping as a function of microwave power. The red and blue lines are the partitioned signals obtained from fitting the spectra to a double pseudo-Voigt. The Lorentzian widths obtained from red lines were used to calculate the actual T_2	69
4.11 EPR spectra collected at 4.2 K of photodoped SrTiO_3 as a function of microwave power. The red and blue lines are the partitioned signals obtained from fitting the spectra to two pseudo-Voigt profiles to account for the g -anisotropy of the distorted Ti^{3+} defect. The Lorentzian widths obtained from red lines were used to calculate the actual T_2	69
4.12 EPR signal intensity of Cr^{3+} before photodoping as a function of microwave power at different temperatures. The microwave power in which the signal saturates increases with temperature.	70
4.13 Room temperature EPR spectra of 0.1% $\text{Cr}^{3+}:\text{SrTiO}_3$ nanocrystals in hexanes before (red) and after (blue) UV irradiation. Inset: reversible EPR intensity of the Cr^{3+} maximum at 356 mT under aerobic conditions in the EPR spectrometer. Note the initial <i>decrease</i> of Cr^{3+} EPR intensity begins immediately upon light irradiation. This experiment is also done for short irradiation times, which does not result in total disappearance of the Cr^{3+} EPR signal (the y-axes of the main spectrum and inset are the equivalent). This result is consistent with initial formation of Ti^{3+} and not with reduction of EPR-silent and higher-valent Cr ions such as Cr^{4+} or Cr^{6+}	71

CHAPTER 1

INTRODUCTION INTO PEROVSKITE BASED MATERIALS AND THEIR MULTIFUNCTIONALITY

1.1 Introduction to spintronics

The discovery of the giant magnetoresistive effect was the beginning of the field of Spin transport electronics or Spintronics.¹⁻³ Alternating thin film layers of ferromagnetic with a nonmagnetic layer in between is the basic structure in which the giant magnetoresistive effect is utilized (figure 1.1). The resistance is lowest when the spins are aligned in parallel in the ferromagnetic layers and the resistance is highest when they are antiparallel.⁴ Spintronics is a rapidly developing field which studies the spin-carrier interactions between magnetic transition metal dopants in wide bandgap semiconductors and free charge carriers. The development of spintronics over the years has been focused on several aspects. The focus was on generating new novel magnetic nanomaterials, optical spin manipulation in magnetic nanomaterials,⁵ magnetoelectronics and magneto-optical properties, pattern recognition and instrument engineering.⁶ Important objectives in spintronics have been to optimize the electron spin lifetime, detect spin coherence times in nanoscale materials, and attempts to transport the polarized spins across macroscopic lengths.⁷ These objectives have led to three major questions: (1) what are effective ways to polarize spin states, (2) how long do these polarized spin states last, and (3) how can these changes in spin be measured.

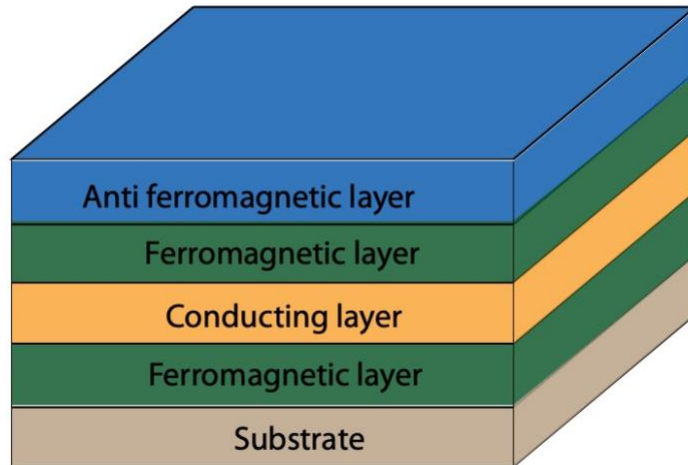


Figure 1.1. Schematic representation of the spin based electronic devices.

Electron spin can be polarized by several methods, but not limited to optic, electric and magnetic excitation means.⁸ Optical methods such as time-resolved faraday rotation (TRFR) are used to study the spin coherency. TRFR is a pump-probe spectroscopic technique which uses circularly polarized light to excite spin-polarized electrons in semiconductors. The resulting magnetization is monitored as a function of time. The time it takes for the magnetization to dissipate yields spin coherence data.⁹⁻¹¹ Electric methods to create spin-polarized electrons were reported possible through the application of an electric field.¹² Other electric methods such as spin-polarized inelastic scanning tunneling spectroscopy (SP-ISTS) have been used.¹³ In SP-ISTS, characteristic spin excitation energies are used to identify magnetic dopant sites. A decrease and then subsequent increase in the bias voltage corresponds to the energy required to excite an electron from the ground state to the excited state. Spin relaxation times from these measurements are extracted from matching the data to perturbation theory simulations.¹⁴ Magnetic methods such as electron paramagnetic resonance spectroscopy (EPR) first produce coherent electrons by applying a magnetic field to paramagnetic materials.¹⁵ Line width analyses

allow spin decoherence times to be obtained and power saturation studies yield spin-lattice relaxation times. EPR enables a facile way to measure spin relaxation dynamics. The spin decoherence and spin-lattice relaxation times are two important concepts in spintronics.

1.2 Spin relaxation processes

Spin dynamics and relaxation times and mechanisms are important in the field of spintronics. To be a viable option in electronics, long spin relaxation times are necessary for encoded information to travel long distances.¹⁶ Typical ranges for these relaxation times have been found to vary from as short as nanoseconds to as long as microseconds.⁸ The length of these relaxation times is dependent on the mechanism and timescale of spin depolarization.

Two important energy relaxation pathways that are studied are spin-lattice relaxation times (T_1) and spin-spin times (spin decoherence time, T_2). The spin-lattice relaxation time is defined as the thermal equilibration of the spin population and the spin decoherence time is the time it takes for the spin state to lose its phase.¹⁷ The longer these relaxation times, the more useful the device will be since the information stored in the spin state would be able to travel further without dissipating.¹⁸ Therefore it is important to minimize pathways for spins decoherence. Spin coherency refers to electrons solely in the conduction band. The presence of holes is detrimental to the polarized spin. The exchange between electrons and holes results in the decoherence of both types of carriers. To counter this, measurements on spin relaxation must be done in the absence of holes. In quantum dot semiconductors, the magnitude of T_1 is typically nanoseconds at room temperature but can be enhanced in II-VI and III-V quantum dot systems.¹⁸⁻²⁰ Other metallic systems find spin relaxation times to be as short as femtoseconds or as long as microseconds at low

temperatures.^{13, 21} For spintronic applications, relaxation times in the nanoseconds are considered “long” spin relaxation times. Both the spin-lattice relaxation time and spin-spin relaxation time are important values to be modulated in the field of spintronics.

The work on spintronics has been primarily focused on Mn doping into II-VI and III-V quantum dot materials such as GaAs and CdTe.^{16, 22} One of the major issues with II-VI semiconductors is due to the necessity of low temperature operations.⁶ These paramagnetic materials lose their magnetization as the temperature increases. Mixed valance perovskites and manganates like $\text{La}_{0.70}\text{Sr}_{0.30}\text{MnO}_3$ and other oxide-based materials such as Co-doped TiO_2 have been transitioning into spin based applications.²³⁻²⁴ Magnetically doped perovskite-based materials containing the necessary magnetic and optical properties could be a promising material to study spin-based phenomena for spintronic applications.

1.3 Strontium titanate: Perovskite basics

SrTiO_3 is an archetypal cubic perovskite having a general chemical formula of ABX_3 . The ionic radius of the cationic A site is typically larger than the B site and X is the anion. In SrTiO_3 , the A-site Sr^{2+} lies on the corners of the unit cell and is surrounded by 12 O^{2-} anions resulting in a pseudo-dodecahedral coordination. The B-site Ti^{4+} is in the center and is octahedrally coordinated by 6 O^{2-} anions (figure 1.2). At room temperature, SrTiO_3 is cubic and undergoes a phase transformation to tetragonal below 105.5 K.²⁵

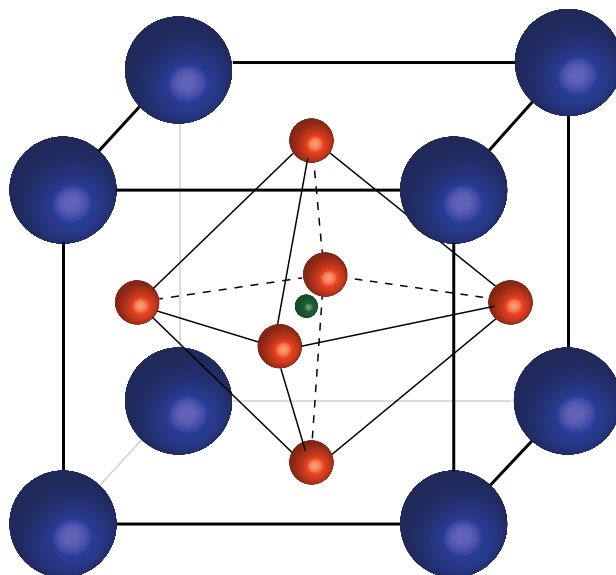


Figure 1.2. Structural depiction of SrTiO₃. The Sr²⁺ ions (blue) occupy the corners. The Ti⁴⁺ (green) lies in the center of and octahedra of O²⁻ ions (orange).

1.4 Types of lattices and synthesis methods

SrTiO₃ can be found in a multitude of different size and morphologies such as ceramic bulk powders,²⁶⁻²⁸ nanoparticles,²⁹⁻³² single crystals,³³⁻³⁷ or colloidal suspensions.³⁸⁻⁴² Each different form requires a different synthetic approach to successfully synthesize. Bulk SrTiO₃ is typically synthesized using a high-temperature solid-state calcination.⁴³⁻⁴⁴ Single crystalline SrTiO₃ can be synthesized using the flame fusion verneuil method⁴⁵⁻⁴⁷ or the floating zone method.⁴⁸⁻⁴⁹ SrTiO₃ nanoparticles (NP) can involve a solvothermal approach of using metal alkoxides in non-aqueous solvents at high temperatures and pressures.⁵⁰ Another method used to make SrTiO₃ NPs is a microwave-assisted hydrothermal method in which microwaves are used to reduce both the reaction time and temperatures required.⁵¹ Lastly, colloidal analogs of SrTiO₃ NPs can be synthesized using simple hydrothermal methods in strongly alkaline mediums.³⁸⁻⁴⁰ The size of the material matters. The properties of the material changes as size decreases due to

quantum confinement effects.⁵² As a result, the intrinsic and extrinsic defects such as dopants should differ in bulk versus nanosized particles where the surface properties are more pronounced.

1.5 The impact of doping in SrTiO₃

Doping is a process that imparts novel properties by intentionally introducing defects into the host lattice.⁵³ Aliovalent dopants will require some form of charge compensation to maintain charge neutrality. The most common forms of charge balance are oxygen vacancies,⁵⁴⁻⁵⁶ strontium vacancies⁵⁷⁻⁵⁸ or conduction band electrons.^{33, 59-60} There are two main types of dopants, donor and acceptor. Donor dopants typically introduce free electrons into the lattice as charge compensation thus creating n-type materials. Acceptor dopants typically induce the formation of oxygen vacancies, creating p-type materials. In SrTiO₃ donor dopants such as La³⁺ for Sr²⁺ and Nb⁵⁺ for Ti⁴⁺ increases the conductivity of the hosts and can even become superconducting at low temperatures.⁶¹⁻⁶³ This phenomenon is accomplished through creating reduced SrTiO₃, either through forming Ti³⁺ and/or oxygen vacancies.²⁷ The variable conductive properties in these donor doped materials make them good choices as conductive substrates.⁶⁴⁻⁶⁵ Acceptor dopants such as Cr³⁺, Fe³⁺, or Mn²⁺ preferentially substitute for Ti⁴⁺ due to similarities in their ionic radii and typically require stoichiometric amounts of oxygen vacancies as charge compensation. Introducing these aliovalent dopants induce various optical,⁶⁶⁻⁷⁰ electrical^{41, 71-72} and magnetic⁷³⁻⁷⁵ properties to SrTiO₃ (figure 1.3). Due to these dopant dependent based properties, SrTiO₃ has a multitude of applications it can have potential applications in various fields such as photocatalysis, thermoelectrics, or spintronics. Control over these

defects are important because they can either be beneficial or detrimental to the designated application.

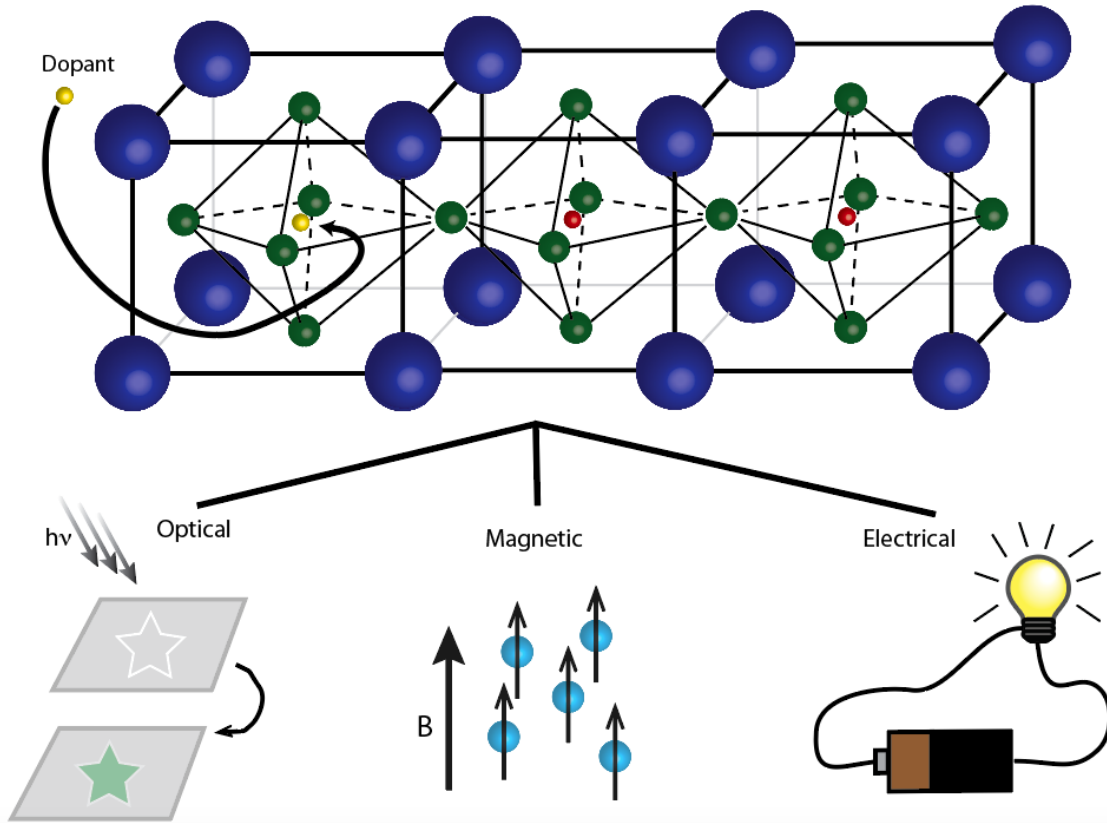


Figure 1.3. Schematic representation of the doping process. Dopant incorporation can lead to novel optical, magnetic and electrical properties.

1.6 Colloidal SrTiO₃ nanocrystals

Colloidal NCs are extremely versatile materials. They can be used a variety of manufacturing methods not available to powders. They can be used to make thin films or as a solution source for ink-jet printing. There are very little reports of synthesized doped colloidal SrTiO₃ NCs in the literature and it is not well understood how electrons in colloidal SrTiO₃ NCs interact with dopants and defects. These colloidal materials open up better possibilities of characterization that are were not limited by bulk materials such as photodoping.

The work herein focuses on the incorporation and characterization of magnetic dopant ions into Colloidal SrTiO₃ NCs. The oxidation state and dopant position will be studied through dopant specific characterization techniques such as electron paramagnetic resonance (EPR) spectroscopy. Cr³⁺ was chosen as a starting point due to the spectroscopic signatures for facile characterizations of internal doping. Mn⁴⁺ was chosen next because it is isovalent with Ti⁴⁺ and isoelectronic with Cr³⁺. Cr³⁺ would need charge compensation, whereas Mn⁴⁺ wouldn't and therefore the induced defects should be different. The intrinsic and extrinsic defects will be investigated through photodoping to gain a better understanding of dopant-defect interactions in colloidal SrTiO₃ and to demonstrate control over dopant-charge carrier interactions. These colloidal NCs were used as a new model to gain a fundamental understanding of spin relaxation dynamics in magnetically doped colloidal SrTiO₃ NCs for spintronic applications.

1.7 References

1. Baibich, M. N.; Broto, J. M.; Fert, A.; Nguyen Van Dau, F.; Petroff, F.; Etienne, P.; Creuzet, G.; Friederich, A.; Chazelas, J., Giant magnetoresistance of (001)Fe/(001)Cr magnetic superlattices. *Phys. Rev. Lett.* **1988**, *61* (21), 2472-2475.
2. Barnaś, J.; Fuss, A.; Camley, R. E.; Grünberg, P.; Zinn, W., Novel magnetoresistance effect in layered magnetic structures: Theory and experiment. *Phys. Rev. B* **1990**, *42* (13), 8110-8120.
3. Wolf, S. A.; Chtchelkanova, A. Y.; Treger, D. M., Spintronics—A retrospective and perspective. *IBM J. Res. Dev.* **2006**, *50* (1), 101-110.
4. Prinz, G. A., Magnetoelectronics. *Science* **1998**, *282* (5394), 1660-1663.
5. Wolf, S. A.; Awschalom, D. D.; Buhrman, R. A.; Daughton, J. M.; von Molnar, S.; Roukes, M. L.; Chtchelkanova, A. Y.; Treger, D. M., Spintronics: a spin-based electronics vision for the future. *Science* **2001**, *294* (5546), 1488-95.

6. Ivanov, V. A.; Aminov, T. G.; Novotortsev, V. M.; Kalinnikov, V. T., Spintronics and spintronics materials. *Russ. Chem. Bull.* **2004**, *53* (11), 2357-2405.
7. Wu, M. W.; Jiang, J. H.; Weng, M. Q., Spin dynamics in semiconductors. *Phys. Rep.* **2010**, *493* (2-4), 61-236.
8. Žutić, I.; Fabian, J.; Das Sarma, S., Spintronics: Fundamentals and applications. *Rev. Mod. Phys.* **2004**, *76* (2), 323-410.
9. Ghosh, S.; Sih, V.; Lau, W. H.; Awschalom, D. D.; Bae, S. Y.; Wang, S.; Vaidya, S.; Chapline, G., Room-temperature spin coherence in ZnO. *Appl. Phys. Lett.* **2005**, *86* (23).
10. Crooker, S. A.; Awschalom, D. D.; Baumberg, J. J.; Flack, F.; Samarth, N., Optical spin resonance and transverse spin relaxation in magnetic semiconductor quantum wells. *Phys. Rev. B* **1997**, *56* (12), 7574-7588.
11. Crooker, S. A.; Baumberg, J. J.; Flack, F.; Samarth, N.; Awschalom, D. D., Terahertz Spin Precession and Coherent Transfer of Angular Momenta in Magnetic Quantum Wells. *Phys. Rev. Lett.* **1996**, *77* (13), 2814-2817.
12. Magarill, L. I.; Chaplik, A. V.; Éntin, M. V., Spin response of 2D electrons to a lateral electric field. *Semiconductors* **2001**, *35* (9), 1081-1087.
13. Hermenau, J.; Ternes, M.; Steinbrecher, M.; Wiesendanger, R.; Wiebe, J., Long Spin-Relaxation Times in a Transition-Metal Atom in Direct Contact to a Metal Substrate. *Nano. Lett.* **2018**, *18* (3), 1978-1983.
14. Ternes, M., Spin excitations and correlations in scanning tunneling spectroscopy. *New J. Phys.* **2015**, *17* (6).
15. Cerletti, V.; Coish, W. A.; Gywat, O.; Loss, D., Recipes for spin-based quantum computing. *Nanotechnology* **2005**, *16* (4), R27-R49.
16. Ohno, Y.; Young, D. K.; Beschoten, B.; Matsukura, F.; Ohno, H.; Awschalom, D. D., Electrical spin injection in a ferromagnetic semiconductor heterostructure. *Nature* **1999**, *402* (6763), 790-792.
17. Hanson, R.; Awschalom, D. D., Coherent manipulation of single spins in semiconductors. *Nature* **2008**, *453* (7198), 1043-9.
18. Das Sarma, S.; Fabian, J.; Hu, X.; Žutić, I., Spintronics: electron spin coherence, entanglement, and transport. *Superlattices Microstruct.* **2000**, *27* (5-6), 289-295.
19. Awschalom, D. D.; Kikkawa, J. M., Electron Spin and Optical Coherence in Semiconductors. *Phys. Today* **1999**, *52* (6), 33-38.

20. Fabian, J.; Sarma, S. D., Spin relaxation of conduction electrons. *J. Vac. Sci. Technol. B* **1999**, *17* (4).
21. Kolbe, W., Spin Relaxation Time of Conduction Electrons in Bulk Sodium Metal. *Phys. Rev. B* **1971**, *3* (2), 320-323.
22. Furdyna, J. K., Diluted magnetic semiconductors. *J. Appl. Phys.* **1988**, *64* (4), R29-R64.
23. Coey, J. M. D.; Viret, M.; von Molnár, S., Mixed-valence manganites. *Adv. Phys.* **1999**, *48* (2), 167-293.
24. Matsumoto, Y., Room-Temperature Ferromagnetism in Transparent Transition Metal-Doped Titanium Dioxide. *Science* **2001**, *291* (5505), 854-856.
25. Salje, E. K. H.; Gallardo, M. C.; Jiménez, J.; Romero, F. J.; Cerro, J. d., The cubic-tetragonal phase transition in strontium titanate: excess specific heat measurements and evidence for a near-tricritical, mean field type transition mechanism. *J. Phys.: Condens. Matter* **1998**, *10* (25), 5535-5543.
26. Rice, W. D.; Ambwani, P.; Bombeck, M.; Thompson, J. D.; Haugstad, G.; Leighton, C.; Crooker, S. A., Persistent optically induced magnetism in oxygen-deficient strontium titanate. *Nat. Mater.* **2014**, *13* (5), 481-7.
27. Neagu, D.; Irvine, J. T. S., Enhancing Electronic Conductivity in Strontium Titanates through Correlated A and B-Site Doping. *Chem. Mater.* **2011**, *23* (6), 1607-1617.
28. Moos, R.; Hardtl, K. H., Defect Chemistry of Donor-Doped and Undoped Strontium Titanate Ceramics between 1000° and 1400°C. *J. Am. Ceram. Soc.* **2005**, *80* (10), 2549-2562.
29. Zhan, H.; Chen, Z.-G.; Zhuang, J.; Yang, X.; Wu, Q.; Jiang, X.; Liang, C.; Wu, M.; Zou, J., Correlation between Multiple Growth Stages and Photocatalysis of SrTiO₃ Nanocrystals. *J. Phys. Chem. C* **2015**, *119* (7), 3530-3537.
30. Chen, D.; Jiao, X.; Zhang, M., Hydrothermal synthesis of strontium titanate powders with nanometer size derived from different precursors. *J. Eur. Ceram. Soc.* **2000**, *20* (9), 1261-1265.
31. Balaya, P.; Ahrens, M.; Kienle, L.; Maier, J.; Rahmati, B.; Lee, S. B.; Sigle, W.; Pashkin, A.; Kuntscher, C.; Dressel, M., Synthesis and Characterization of Nanocrystalline SrTiO₃. *J. Am. Ceram. Soc.* **2006**, *0* (0), 2804-2811.

32. Park, N.-H.; Wang, Y.; Seo, W.-S.; Dang, F.; Wan, C.; Koumoto, K., Solution synthesis and growth mechanism of SrTiO₃ mesocrystals. *Cryst. Eng. Comm.* **2013**, *15* (4), 679-685.
33. Hanzig, J.; Abendroth, B.; Hanzig, F.; Stöcker, H.; Strohmeyer, R.; Meyer, D. C.; Lindner, S.; Grobosch, M.; Knupfer, M.; Himcinschi, C.; Mühle, U.; Munnik, F., Single crystal strontium titanate surface and bulk modifications due to vacuum annealing. *J. Appl. Phys.* **2011**, *110* (6).
34. Enterkin, J. A.; Subramanian, A. K.; Russell, B. C.; Castell, M. R.; Poeppelmeier, K. R.; Marks, L. D., A homologous series of structures on the surface of SrTiO₃ (110). *Nat. Mater.* **2010**, *9* (3), 245-8.
35. Yumashev, K. V.; Prokoshin, P. V.; Malyarevich, A. M.; Mikhailov, V. P., Transient bleaching/induced absorption in reduced SrTiO₃ under picosecond excitation. *J. Opt. Soc. Am. B: Opt. Phys.* **1997**, *14* (2).
36. Kan, D.; Kanda, R.; Kanemitsu, Y.; Shimakawa, Y.; Takano, M.; Terashima, T.; Ishizumi, A., Blue luminescence from electron-doped SrTiO₃. *Appl. Phys. Lett.* **2006**, *88* (19).
37. Szot, K.; Speier, W., Surfaces of reduced and oxidized SrTiO₃ from atomic force microscopy. *Phys. Rev. B* **1999**, *60* (8), 5909-5926.
38. Park, K.; Son, J. S.; Woo, S. I.; Shin, K.; Oh, M.-W.; Park, S.-D.; Hyeon, T., Colloidal synthesis and thermoelectric properties of La-doped SrTiO₃ nanoparticles. *J. Mater. Chem. A* **2014**, *2* (12).
39. Dang, F.; Mimura, K.-i.; Kato, K.; Imai, H.; Wada, S.; Haneda, H.; Kuwabara, M., Growth of monodispersed SrTiO₃ nanocubes by thermohydrolysis method. *Cryst. Eng. Comm.* **2011**, *13* (11).
40. Fujinami, K.; Katagiri, K.; Kamiya, J.; Hamanaka, T.; Koumoto, K., Sub-10 nm strontium titanate nanocubes highly dispersed in non-polar organic solvents. *Nanoscale* **2010**, *2* (10), 2080-3.
41. Wan, T.; Qu, B.; Du, H.; Lin, X.; Guan, P.; Lin, Q.; Chen, N.; Teck Tan, T.; Hang, T.; Chu, D., Tunable resistance switching in solution processed chromium-doped strontium titanate nanoparticles films. *J. Colloid Interface Sci.* **2017**, *494*, 178-184.
42. Lin, Y.; Wen, J.; Hu, L.; McCarthy, J. A.; Wang, S.; Poeppelmeier, K. R.; Marks, L. D., Electron-induced Ti-rich surface segregation on SrTiO₃ nanoparticles. *Micron*. **2015**, *68*, 152-7.

43. Lehuta, K. A.; Kittilstved, K. R., Speciation of Cr(III) in intermediate phases during the sol-gel processing of Cr-doped SrTiO₃ powders. *J. Mater. Chem. A* **2014**, *2* (17), 6138-6145.
44. Townsend, T. K.; Browning, N. D.; Osterloh, F. E., Nanoscale strontium titanate photocatalysts for overall water splitting. *ACS Nano* **2012**, *6* (8), 7420-6.
45. Jalan, B.; Engel-Herbert, R.; Mates, T. E.; Stemmer, S., Effects of hydrogen anneals on oxygen deficient SrTiO_{3-x} single crystals. *Appl. Phys. Lett.* **2008**, *93* (5).
46. Mochizuki, S.; Minami, S.; Fujishiro, F., The reversible UV-laser-light-induced spectral change and origin of the 2.4eV luminescence band in SrTiO₃. *J. Lumin.* **2005**, *112* (1-4), 267-270.
47. Rubano, A.; Paparo, D.; Granozio, F. M.; Scotti di Uccio, U.; Marrucci, L., Blue luminescence of SrTiO₃ under intense optical excitation. *J. Appl. Phys.* **2009**, *106* (10).
48. Alvarado, S. F.; La Mattina, F.; Bednorz, J. G., Electroluminescence in SrTiO₃:Cr single-crystal nonvolatile memory cells. *Appl. Phys. A* **2007**, *89* (1), 85-89.
49. La Mattina, F.; Bednorz, J. G.; Alvarado, S. F.; Shengelaya, A.; Müller, K. A.; Keller, H., Controlled oxygen vacancies and space correlation with Cr³⁺ in SrTiO₃. *Phys. Rev. B* **2009**, *80* (7).
50. Bykov, I.; Makarova, M.; Trepakov, V.; Dejneka, A.; Yurchenko, L.; Yurchenko, L.; Jäger, A.; Jastrabik, L., Intrinsic and impurity defects in chromium-doped SrTiO₃ nanopowders: EPR and NMR study. *Phys. Status Solidi B* **2013**, *250* (4), 821-824.
51. da Silva, L. F.; Avansi, W.; Andres, J.; Ribeiro, C.; Moreira, M. L.; Longo, E.; Mastelaro, V. R., Long-range and short-range structures of cube-like shape SrTiO₃ powders: microwave-assisted hydrothermal synthesis and photocatalytic activity. *Phys. Chem. Chem. Phys.* **2013**, *15* (29), 12386-93.
52. Roduner, E., Size matters: why nanomaterials are different. *Chem. Soc. Rev.* **2006**, *35* (7), 583-92.
53. Erwin, S. C.; Zu, L.; Haftel, M. I.; Efros, A. L.; Kennedy, T. A.; Norris, D. J., Doping semiconductor nanocrystals. *Nature* **2005**, *436* (7047), 91-4.
54. Müller, K. A.; Berlinger, W.; Rubins, R. S., Observation of Two Charged States of a Nickel-Oxygen Vacancy Pair in SrTiO₃ by Paramagnetic Resonance. *Phys. Rev.* **1969**, *186* (2), 361-371.

55. Li, H.; Yin, S.; Wang, Y.; Sekino, T.; Lee, S. W.; Sato, T., Roles of Cr³⁺ doping and oxygen vacancies in SrTiO₃ photocatalysts with high visible light activity for NO removal. *J. Catal.* **2013**, *297*, 65-69.
56. Szot, K.; Speier, W.; Carius, R.; Zastrow, U.; Beyer, W., Localized metallic conductivity and self-healing during thermal reduction of SrTiO₃. *Phys. Rev. Lett.* **2002**, *88* (7), 075508.
57. Moos, R.; Bischoff, T.; Menesklou, W.; Hardtl, K. H., Solubility of lanthanum in strontium titanate in oxygen-rich atmospheres. *J. Mater. Sci.* **1997**, *32* (16), 4247-4252.
58. Kolodiaznyi, T.; Petric, A., The Applicability of Sr-deficient n-type SrTiO₃ for SOFC Anodes. *J. Electroceram.* **2005**, *15* (1), 5-11.
59. Balachandran, U., Electrical Conductivity in Lanthanum-Doped Strontium Titanate. *J. Electrochem. Soc.* **1982**, *129* (5).
60. Ertekin, E.; Srinivasan, V.; Ravichandran, J.; Rossen, P. B.; Siemons, W.; Majumdar, A.; Ramesh, R.; Grossman, J. C., Interplay between intrinsic defects, doping, and free carrier concentration in SrTiO₃ thin films. *Phys. Rev. B* **2012**, *85* (19).
61. Binnig, G.; Baratoff, A.; Hoenig, H. E.; Bednorz, J. G., Two-Band Superconductivity in Nb-Doped SrTiO₃. *Phys. Rev. Lett.* **1980**, *45* (16), 1352-1355.
62. Kozuka, Y.; Kim, M.; Ohta, H.; Hikita, Y.; Bell, C.; Hwang, H. Y., Enhancing the electron mobility via delta-doping in SrTiO₃. *Appl. Phys. Lett.* **2010**, *97* (22).
63. Schooley, J. F.; Hosler, W. R.; Cohen, M. L., Superconductivity in Semiconducting SrTiO₃. *Phys. Rev. Lett.* **1964**, *12* (17), 474-475.
64. Huang, Y.; Lü, H.; Guo, H.; Liu, L.; He, M.; Chen, Z.; Zhou, Y.; Zhao, K.; Jin, K.; Yang, G., Structure and electrical characteristics of Nb-doped SrTiO₃ substrates. *Chin. Sci. Bull.* **2006**, *51* (16), 2035-2037.
65. Yuan, G. L.; Liu, J. M.; Baba-Kishi, K.; Chan, H. L. W.; Choy, C. L.; Liu, Z. G., Possible mechanism for tunneling magnetoresistance in La_{0.9}Ba_{0.1}MnO₃/Nb-doped SrTiO₃ p-n junctions. *Solid State Commun.* **2004**, *131* (6), 383-387.
66. Kato, H.; Kudo, A., Visible-Light-Response and Photocatalytic Activities of TiO₂ and SrTiO₃ Photocatalysts Codoped with Antimony and Chromium. *J. Phys. Chem. B* **2002**, *106* (19), 5029-5034.

67. Tonda, S.; Kumar, S.; Anjaneyulu, O.; Shanker, V., Synthesis of Cr and La-codoped SrTiO₃ nanoparticles for enhanced photocatalytic performance under sunlight irradiation. *Phys. Chem. Chem. Phys.* **2014**, *16* (43), 23819-28.
68. Yu, H.; Ouyang, S.; Yan, S.; Li, Z.; Yu, T.; Zou, Z., Sol-gel hydrothermal synthesis of visible-light-driven Cr-doped SrTiO₃ for efficient hydrogen production. *J. Mater. Chem.* **2011**, *21* (30).
69. Bryknar, Z.; Trepakov, V.; Potůček, Z.; Jastrabík, L., Luminescence spectra of SrTiO₃:Mn⁴⁺. *J. Lumin.* **2000**, *87-89*, 605-607.
70. Potůček, Z.; Trepakov, V.; Deyneka, A.; Bryknar, Z.; Galinetto, P.; Rossella, F., Luminescence and Absorption Spectroscopy of Weakly Mn-Doped SrTiO₃ Crystals. *Ferroelectrics* **2008**, *367* (1), 102-110.
71. Tkach, A.; Vilarinho, P. M.; Kholkin, A. L., Dependence of dielectric properties of manganese-doped strontium titanate ceramics on sintering atmosphere. *Acta Mater.* **2006**, *54* (20), 5385-5391.
72. Choudhury, D.; Pal, B.; Sharma, A.; Bhat, S. V.; Sarma, D. D., Magnetization in electron- and Mn-doped SrTiO₃. *Sci. Rep.* **2013**, *3*, 1433.
73. Azzoni, C. B.; Mozzati, M. C.; Paleari, A.; Massarotti, V.; Bini, M.; Capsoni, D., Magnetic evidence of different environments of manganese ions in Mn-substituted strontium titanate. *Solid State Commun.* **2000**, *114* (12), 617-622.
74. Badalyan, A. G.; Syrnikov, P. P.; Azzoni, C. B.; Galinetto, P.; Mozzati, M. C.; Rosa, J.; Trepakov, V. A.; Jastrabik, L., Manganese oxide nanoparticles in SrTiO₃:Mn. *J. Appl. Phys.* **2008**, *104* (3).
75. Valant, M.; Kolodiazhnyi, T.; Arčon, I.; Aguesse, F.; Axelsson, A.-K.; Alford, N. M., The Origin of Magnetism in Mn-Doped SrTiO₃. *Adv. Funct. Mater.* **2012**, *22* (10), 2114-2122.

CHAPTER 2

TUNABLE ELECTRONIC STRUCTURE AND SURFACE DEFECTS IN CHROMIUM-DOPED STRONTIUM TITANATE NANOCRYSTALS

This chapter has been adapted from the published work:

Harrigan, W. L.; Michaud, S. E.; Lehuta, K. A.; Kittilstved, K. R., Tunable Electronic Structure and Surface Defects in Chromium-Doped Colloidal SrTiO_{3-δ} Nanocrystals. *Chem. Mater.* **2016**, *28*, 430-433.

2.1 Introduction

SrTiO₃ is the prototypical oxide with electronic properties that can be modulated by strain engineering to produce superconductivity at heterostructured interfaces,¹ ferroelectricity,² high-*k* gate dielectrics,³ and giant spin splittings.⁴ Additional control over the electronic properties of SrTiO₃ has been demonstrated by paramagnetic transition metal ions such as trivalent chromium. As an example, it has been demonstrated that the resistive memory effect in Cr³⁺-doped SrTiO₃ can be switched reversibly by either electric fields or photons for solid-state memory applications.⁵⁻⁶

SrTiO₃ has also shown promise in the photoelectrochemical splitting of water.⁷⁻⁹ However, the transparency¹⁰ of SrTiO₃ in the visible region makes it an overall inefficient solar photocatalyst. Design strategies to enhance the visible light activity of oxide perovskites has been pursued. One promising strategy is the introduction of substitutional transition metal ions into wide-gap semiconductors. The goal of such a strategy is to create new sub-bandgap impurity bands that generate either conduction band electrons and/or valence band holes by visible photons. Kudo and co-workers have utilized this strategy and have demonstrated that Cr³⁺ and Rh³⁺-doped SrTiO₃ are promising visible-light

photocatalysts for H₂ evolution.¹¹⁻¹⁴ Another recent example¹⁵ of this strategy is the photoreduction of CO₂ with Co-doped SrTiO₃.

Colloidal syntheses of oxide-based perovskite NCs for photocatalysis and other applications have focused primarily on undoped materials due to the lack of synthetic methods for preparing both colloidal *and* doped NCs.⁷ Recent efforts to address this void include free-standing colloidal Ba(Ti_{1-x}Cr_x)O₃ NCs¹⁶ and sintered (Sr_{1-y}La_y)TiO₃ NCs prepared by colloidal methods.¹⁷ Herein, we report the successful preparation and spectroscopic characterization of ~10 nm colloidal Sr(Ti_{1-x}Cr_x)O_{3-δ} NCs by two aqueous hydrothermal methods that differ only by the presence of N₂H₄. The incorporation of Cr³⁺ dopants in the B-site of SrTiO_{3-δ} NCs is demonstrated with both synthetic methods. However, EPR and PL spectroscopies reveal stable, but different, oxygen-related defects in Sr(Ti_{1-x}Cr_x)O_{3-δ} (x=0-0.1%) NCs that are dependent on the synthetic method used. The successful synthesis of Sr(Ti_{1-x}Cr_x)O_{3-δ} NCs opens the door to integrating these multifunctional and potentially multiferroic nanomaterials into flexible electronic devices using established solution-based processing techniques.

Both pure and Cr-doped colloidal SrTiO₃ NCs were prepared by two similar hydrothermal methods.¹⁷⁻¹⁹ The only difference between the two methods is the presence or absence of N₂H₄·H₂O, which we refer to as methods A and B, respectively. Both methods produce oleic acid-capped SrTiO_{3-δ} NCs that are readily dispersed in non-polar organic solvents such as hexanes. The NCs possess primarily pseudo-cubic morphologies with average edge dimensions of ~10 nm ± 2 nm and aspect ratios of ~0.8 ± 0.1 (Figure 2.6).

2.2 Experimental Methods

2.2.1 Materials. Oleic acid (90%, Fisher Chemical), titanium(IV) bis(ammonium lactate)dihydroxide (TiALH, 50% wt in water¹, Alfa Aesar), Sr(OH)₂·8H₂O (99%, Alfa Aesar), Cr(NO₃)₃·9H₂O (Crystalline Certified, Fisher Chemical), tetramethylammonium hydroxide(10 M NMe₄OH, Acros Organics), hydrazine hydrate (N₂H₄·H₂O, 99%, Acros Organics), ethanol (200 proof, PHARMCO-AAPER) and hexanes (optima, Fisher Chemical) were used as received.

2.2.2 Synthesis of colloidal SrTiO_{3-δ} and Cr³⁺-doped SrTiO_{3-δ} nanocrystals. Colloidal SrTiO₃ NCs were prepared by a modified hydrothermal method.¹⁷⁻¹⁹ In a typical synthesis, 1.25 mmol of titanium(IV) bis(ammonium lactate)dihydroxide and Sr(OH)₂·8H₂O were dissolved in 30 mL of distilled H₂O. The pH was adjusted to 12.1 with NMe₄OH (10 M). The solution was transferred to a 45-mL Teflon-lined autoclave and N₂H₄·H₂O (5 mmol) and oleic acid (2.5 mmol) were added.¹⁹ The autoclaves were sealed and heated to 200 °C for 24 h. The resulting oleic acid functionalized NCs were washed with ethanol and suspended in hexanes. The synthetic procedure described above will be referred to as method A. Colloidal SrTiO₃ NCs were also prepared by removing only the N₂H₄·H₂O from the reaction mixture and we denote as method B and is similar to the method used to prepare (Sr_{1-y}La_y)TiO₃ colloidal NCs.¹⁸ Both SrTiO₃-A and -B NCs prepared here are primarily nanocubes with average edge dimensions of ~10 nm ± 4 nm.

¹The batch of TiALH received from Alfa Aesar contains common impurities of TiO₂ at ~14% and pH of the solution ~8.4-8.5. The presence of insoluble TiO₂ indicates that slow hydrolysis is taking place in the TiALH bottle and definitely overestimates [Ti] in the calculation of $x_{\text{nom}} = [\text{Cr}] / ([\text{Cr}] + [\text{Ti}])$.

Colloidal Cr₂O₃ was prepared by adding 0.625 mmol of Cr(acac)₃ into 13.75 mL of distilled water. The pH was adjusted to 12.7 using NMe₄OH (10 M). The solution was transferred into a 45 mL Teflon-lined autoclave. Hydrazine (2.5 mmol) and oleic acid (1.25 mmol) are then added. The autoclave is then sealed and placed in a 200 °C for 24 h. The products were washed with ethanol and suspended in hexanes. The product was amorphous and the EPR spectrum at room temperature is shown in figure 2.11.

2.2.3 Physical Methods. Room-temperature electronic absorption and emission/excitation spectra were collected on colloidal suspensions in hexanes with a Cary 50 Bio and Cary Eclipse, respectively. Low-temperature emission spectra were collected on air-dried powders using a Cary 670 Fourier Transform spectrophotometer equipped with a PMT detector and quartz beamsplitter with excitation from the 488 nm line of an Ar-ion laser operating up to a maximum output power of 9 W (JDS Uniphase, 2214). Alignment of the powdered sample was done using ruby in which both were fixed to a copper plate using conductive silver paint (Leitsilber 200, Ted Pella) that was placed in a closed-cycle helium optical cryostat (Advanced Research Systems HC-2). Electron paramagnetic resonance (EPR) spectroscopy were collected on powdered samples with continuous wave at X-band frequency (~9.6 GHz, Bruker Elexsys-500). X-ray powder diffraction patterns were collected using Cu-K α radiation (PAN-alytical X'Pert Material Research Diffractometer). Transmission electron microscopy images were collected on samples deposited onto a carbon film supported on 400 mesh copper grids at the UMass Amherst Electron Microscopy Center (JEM 2200FS-JEOL for high-resolution images and JEOL JEM-2000FX for low-resolution images). Analysis of TEM was performed using ImageJ software.³⁷

2.3 Results and Discussion

Figure 2.1 shows the room temperature absorption spectra of concentrated and dilute colloidal suspensions of $\text{SrTiO}_{3-\delta}$ NCs prepared by methods A and B. The electronic absorption spectra of a concentrated suspension of $\text{SrTiO}_{3-\delta}$ -A shown in Figure 2.1a displays only the band gap transition above 3.2 eV. However, the concentrated suspension of $\text{SrTiO}_{3-\delta}$ -B exhibits a broad absorption feature that extends throughout the visible. These absorption features are reflected in the colors of the concentrated $\text{SrTiO}_{3-\delta}$ suspensions with method A producing transparent suspensions and method B resulting in reddish-brown suspensions as shown in the color photos of figure 2.2. Despite the unexpected difference in sample colors, powder X-ray diffraction and TEM studies confirm that *both* products are nanocrystalline $\text{SrTiO}_{3-\delta}$ and primarily cubic in shape (figure 2.7). We tentatively assign this coloration in the $\text{SrTiO}_{3-\delta}$ -B NCs to a significant oxygen deficiency in the $\text{SrTiO}_{3-\delta}$ NCs. This assignment is supported from prior work that $\text{SrTiO}_{3-\delta}$ exhibits a sub-bandgap absorption centered at 2.9 eV that is due to the presence of oxygen vacancies (V_{O}).²⁰ We can also rule out the presence of free carriers and localized Ti^{3+} (Ti'_{Ti}) defects as the origin of the brown color of the $\text{SrTiO}_{3-\delta}$ -B NCs, since *both* defects would give rise to increased absorption at longer wavelengths.²¹

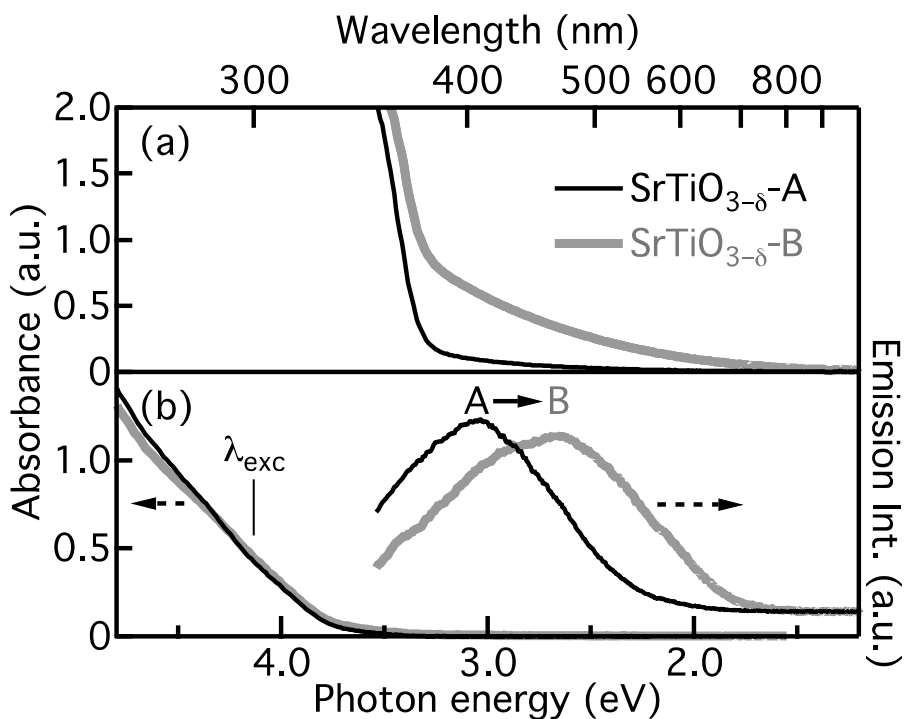


Figure 2.1 Room temperature electronic absorption spectra of (a) concentrated and (b) dilute suspensions of SrTiO_{3-δ}-A (thin lines) and SrTiO_{3-δ}-B (thick lines) NCs in hexanes. (b) Uncorrected emission spectra (dashed) excited at 300 nm.

In dilute solutions, the absorption spectra of SrTiO_{3-δ} prepared by both methods appear similar as shown in Figure 2.1b. However, the photoluminescence (PL) spectra of the SrTiO_{3-δ} suspensions shown in Figure 2.1b display clear differences. The SrTiO_{3-δ}-A NCs has a broad PL centered at ~3.06 eV while the broad PL of the SrTiO_{3-δ}-B NCs is centered at ~2.75 eV. The visible PL in SrTiO_{3-δ} has been previously described within the model of a self-trapped exciton (STE) associated with recombination at localized Ti³⁺-oxygen vacancy complexes.²²⁻²³ The energy difference of the visible PL between the two SrTiO_{3-δ} NCs suggests a significant variation in the nature of the NC surface. This assignment is supported by the appearance of different EPR signals related to SrTiO_{3-δ} NC surface defects (*vide infra*).

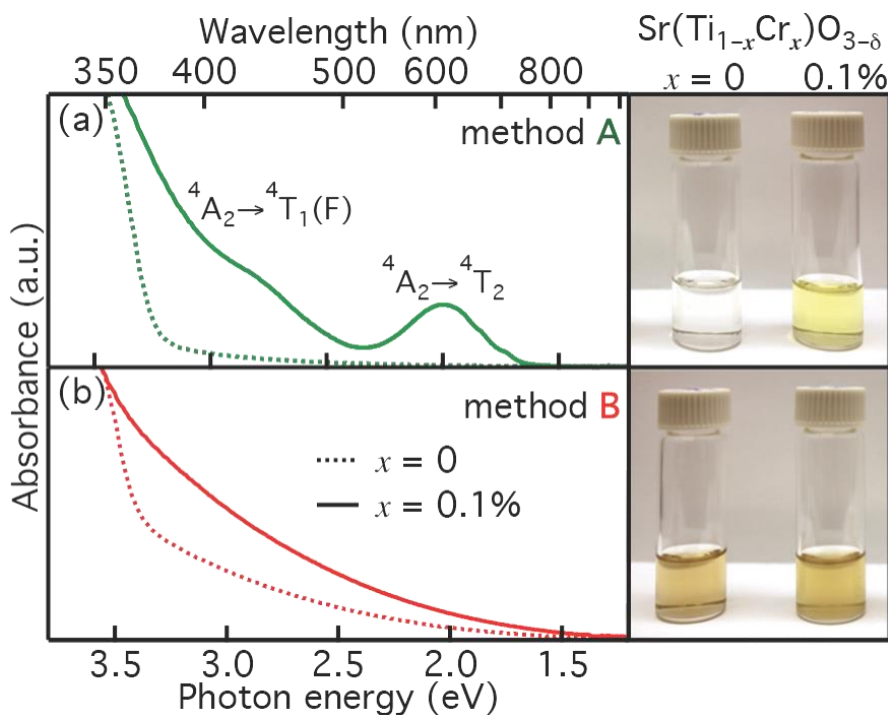


Figure 2.2. Room-temperature electronic absorption spectra of concentrated $\text{Sr}(\text{Ti}_{1-x}\text{Cr}_x)\text{O}_{3-\delta}$ suspensions prepared by (a) method A and (b) method B. The nominal Cr content is $x = 0$ (dashed) and $x = 0.1\%$ (solid). Color photos of $\text{SrTiO}_{3-\delta}$ and $\text{Sr}(\text{Ti}_{1-x}\text{Cr}_x)\text{O}_{3-\delta}$ colloidal suspensions are shown in the right panels.

Attempts to introduce Cr^{3+} into the $\text{SrTiO}_{3-\delta}$ NCs was achieved by adding $\text{Cr}(\text{NO}_3)_3 \cdot 9\text{H}_2\text{O}$ after adjusting the pH. Figure 2.2 shows the electronic absorption spectra and color photos of concentrated suspensions of $\text{Sr}(\text{Ti}_{1-x}\text{Cr}_x)\text{O}_{3-\delta}$ NCs prepared by methods A and B with $x = 0$ and 0.1% (nominal). The $\text{Sr}(\text{Ti}_{1-x}\text{Cr}_x)\text{O}_{3-\delta}$ -A NCs shown in figure 2.2a at this nominal Cr^{3+} content are yellow in color and display weak absorption features at ~ 2.0 eV and 2.8 eV as shown in figure 2.2a. These transitions are readily assigned as the ${}^4\text{A}_2 \rightarrow {}^4\text{T}_2$ and ${}^4\text{A}_2 \rightarrow {}^4\text{T}_1(\text{F})$ transitions of Cr^{3+} in an octahedral ligand field and agree well with previously reported energies for Cr^{3+} -doped BaTiO_3 .²⁴ In contrast, the $\text{Sr}(\text{Ti}_{1-x}\text{Cr}_x)\text{O}_{3-\delta}$ -B NCs with the same nominal Cr^{3+} content displays broad absorption similar to the $\text{SrTiO}_{3-\delta}$ -B NCs and is the identical reddish-brown color (see figure 2.2b). To resolve the Cr speciation we measured the variable-temperature PL and room

temperature EPR spectra to confirm the presence of Cr^{3+} in $\text{SrTiO}_{3-\delta}$ or some other oxide phase.²⁵

The low-temperature PL of $\text{Sr}(\text{Ti}_{1-x}\text{Cr}_x)\text{O}_{3-\delta}$ NCs with $x_{\text{nom}} = 0.1\%$ is shown in figure 2.3. $\text{Sr}(\text{Ti}_{1-x}\text{Cr}_x)\text{O}_{3-\delta}$ NCs prepared by both synthetic approaches display STE-related features near 2.0 eV and a structured PL transition at ~ 1.57 eV that increases in intensity below ~ 250 K. The STE-related emission is red-shifted from the pure $\text{SrTiO}_{3-\delta}$ NCs shown in Figure 2.1 and caused by the change to laser excitation at 488 nm instead of 300 nm from a Xe lamp. The 1.57 eV PL originates in the spin-forbidden ${}^2\text{E} \rightarrow {}^4\text{A}_2$ transition of Cr^{3+} and is similar to that reported for $\text{Sr}(\text{Ti}_{1-x}\text{Cr}_x)\text{O}_{3-\delta}$ single crystals and powders.²⁵⁻²⁸ The energy of the ${}^2\text{E} \rightarrow {}^4\text{A}_2$ transition blue-shifts with increasing temperature (figure 2.8) in agreement with reported PL behavior of $\text{Sr}(\text{Ti}_{1-x}\text{Cr}_x)\text{O}_{3-\delta}$ single crystals. The origin of this energy shift of the Cr^{3+} PL with temperature has been correlated to the temperature-dependence of the SrTiO_3 dielectric constant.^{25-26,28} Importantly, the energy of the ${}^2\text{E}$ state in SrTiO_3 occurs at much lower energies than observed in the possible Cr_2O_3 secondary phase, which is at 1.70 eV.²⁹

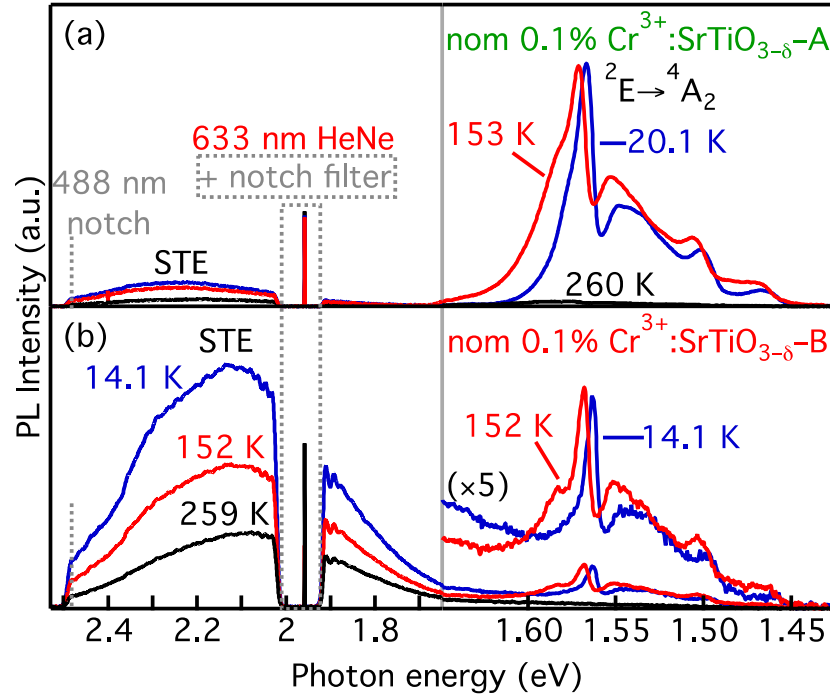


Figure 2.3. Variable-temperature emission spectra of $\text{Sr}(\text{Ti}_{1-x}\text{Cr}_x)\text{O}_{3-\delta}$ ($x_{\text{nom}} = 0.1\%$) NCs prepared by (a) method **A** and (b) method **B**. Note that the energy scale changes at 1.65 eV in order to show the Cr^{3+} PL on an expanded energy scale. The intensity scale, however, is not scaled in the different panels except for the 14.1 K and 152 K spectra in (b) that are also shown scaled by 5. Samples were excited by the 488 nm line of an Ar-ion laser.

While the signal-to-noise of the emission spectrum is noticeably lower for $\text{Sr}(\text{Ti}_{1-x}\text{Cr}_x)\text{O}_{3-\delta}\text{-B}$ NCs, the linewidth of the electronic origin is much narrower (fwhm = 7 meV vs 10 meV, figure 2.8). Another difference is the appearance of the tail from the STE PL at higher energies in the spectra of the $\text{Sr}(\text{Ti}_{1-x}\text{Cr}_x)\text{O}_{3-\delta}\text{-B}$ NCs. Both of these results suggest that the actual x is lower for $\text{Sr}(\text{Ti}_{1-x}\text{Cr}_x)\text{O}_{3-\delta}$ prepared by method B than method A. In other words, most $\text{Sr}(\text{Ti}_{1-x}\text{Cr}_x)\text{O}_{3-\delta}\text{-A}$ NCs contain at least one Cr^{3+} ion, which efficiently quenches the higher energy emission via energy transfer to lower-energy Cr^{3+} d-states and charge-transfer transitions.²⁴ The $\text{Sr}(\text{Ti}_{1-x}\text{Cr}_x)\text{O}_{3-\delta}\text{-B}$ NCs, however, likely have on average less than one Cr^{3+} ion per NC and the STE PL is originating in the sub-population of $\text{SrTiO}_3\text{-B}$ NCs within the $\text{Sr}(\text{Ti}_{1-x}\text{Cr}_x)\text{O}_{3-\delta}\text{-B}$ ensemble. Inductively coupled

plasma optical emission spectrometry (ICP-OES) confirms this scenario with actual x values of 0.15% for $\text{Sr}(\text{Ti}_{1-x}\text{Cr}_x)\text{O}_{3-\delta}\text{-A}$ and 0.09% for $\text{Sr}(\text{Ti}_{1-x}\text{Cr}_x)\text{O}_{3-\delta}\text{-B}$ when $x_{\text{nom}} = 0.1\%$. Repeated ICP-OES measurements on different batches of $\text{Sr}(\text{Ti}_{1-x}\text{Cr}_x)\text{O}_{3-\delta}\text{-A}$ and -B NCs always result in experimental x values that are greater than the nominal x in $\text{Sr}(\text{Ti}_{1-x}\text{Cr}_x)\text{O}_{3-\delta}\text{-A}$ than $\text{Sr}(\text{Ti}_{1-x}\text{Cr}_x)\text{O}_{3-\delta}\text{-B}$. This unusual result suggests that either N_2H_4 is preferentially binding to Sr^{2+} or Ti^{4+} in solution or there is a large error in the reported Ti content in the precursor due to insoluble TiO_2 impurities (see section 2.2.1). Experiments to reveal the nature of the N_2H_4 interaction with the Sr^{2+} and Ti^{4+} precursors in solution are currently underway.

The room-temperature X-band EPR spectra of doped ($x_{\text{nom}}=0.01\%$) and undoped NCs prepared by both methods is shown in figure 2.4. In addition to being a sensitive probe of the local environment surrounding Cr^{3+} ions, EPR spectroscopy has also been utilized to identify defect-related species and shallow carriers in SrTiO_3 bulk powders and related oxide NCs.³⁰⁻³¹ The EPR spectra of both $\text{Sr}(\text{Ti}_{1-x}\text{Cr}_x)\text{O}_{3-\delta}\text{-A}$ and -B NCs display identical features at $g=1.978$ with weak hyperfine splittings from the 9.5% abundant ^{53}Cr $I = 3/2$ nuclei ($|A| = 16.2 \times 10^{-4} \text{ cm}^{-1}$) that agree³² with bulk $\text{Sr}(\text{Ti}_{1-x}\text{Cr}_x)\text{O}_{3-\delta}$.

Bulk $\text{Sr}(\text{Ti}_{1-x}\text{Cr}_x)\text{O}_{3-\delta}$ powders prepared up to $x=2\%$ by a sol-gel technique are reddish in color and also do not display well-resolved absorption bands with the exception of an oxygen vacancy-related band centered at 2.9 eV, which is also observed in nominal $\text{SrTiO}_{3-\delta}$ annealed under reduced pressures.^{20,25} However, the color of $\text{Ba}(\text{Ti}_{1-x}\text{Cr}_x)\text{O}_3$ single crystals has been reported to change from red (with no resolved absorption bands in the visible) to green (with resolved absorption bands similar that shown in figure 2.2a) with increasing x from 0.02% to 0.24%, respectively.²⁴ Furthermore, the low-temperature

emission spectra in both the “red” and “green” samples of $\text{Ba}(\text{Ti}_{1-x}\text{Cr}_x)\text{O}_3$ displayed the same ${}^2\text{E} \rightarrow {}^4\text{A}_2$ PL, which is also observed in both $\text{Sr}(\text{Ti}_{1-x}\text{Cr}_x)\text{O}_{3-\delta}$ -A and -B NCs presented here. Therefore, despite the difference in color of the two sets of $\text{Sr}(\text{Ti}_{1-x}\text{Cr}_x)\text{O}_{3-\delta}$ NCs, both possess Cr^{3+} ions that are substitutional at the B-site of the $\text{SrTiO}_{3-\delta}$ lattice based on the variable-temperature PL and room-temperature EPR spectra.

The EPR spectra shown in figure 2.4 also display two defects: one at ~ 342 mT ($g=2.010$) that is observed in the Cr^{3+} -doped $\text{SrTiO}_{3-\delta}$ -A and -B NCs, and the other at ~ 343 mT ($g=2.004$) that is observed only in the undoped and Cr^{3+} -doped $\text{SrTiO}_{3-\delta}$ -B NCs. Bykov and co-workers have also detected both of these defects in 5 nm $\text{Sr}(\text{Ti}_{1-x}\text{Cr}_x)\text{O}_{3-\delta}$ nanopowders prepared by a different non-colloidal solvothermal method.³³ They assigned both of these signals to oxygen-related defects: O^- ($g \sim 2.010$) and a surface-adsorbed superoxide anion (O_2^- at $g = 2.004$), respectively.³⁴⁻³⁵ The O^- defect, also known as trapped hole centers in the TiO_2 literature,³⁵ is present in the EPR spectra of both $\text{Sr}(\text{Ti}_{1-x}\text{Cr}_x)\text{O}_{3-\delta}$ NCs. The EPR signal of Cr^{3+} appears rigorously cubic and is thus consistent with previous studies where charge compensating defects are not within the first coordination sphere of the Cr^{3+} ion in $\text{SrTiO}_{3-\delta}$.³⁶

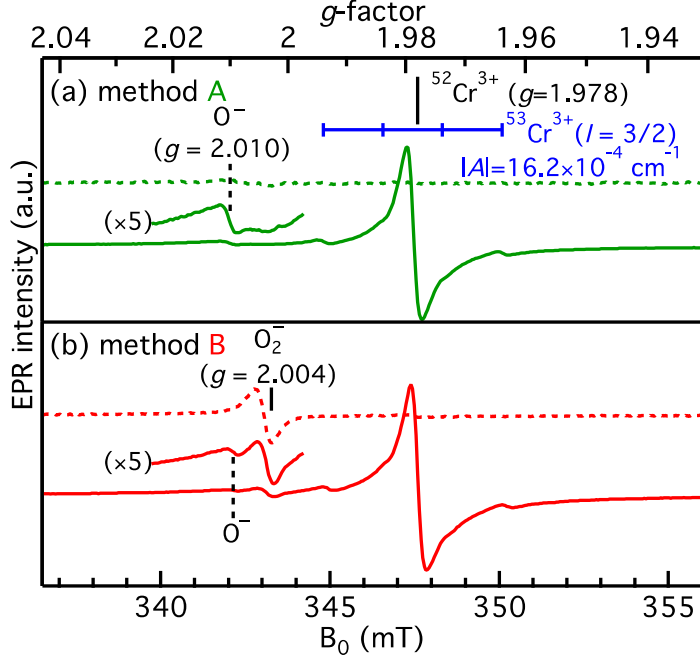
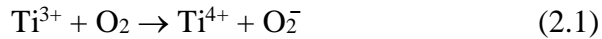


Figure 2.4. Room-temperature X-band EPR spectra of (a) $\text{Sr}(\text{Ti}_{1-x}\text{Cr}_x)\text{O}_{3-\delta}\text{-A}$ and (b) $\text{Sr}(\text{Ti}_{1-x}\text{Cr}_x)\text{O}_{3-\delta}\text{-B}$ with $x = 0$ (dashed line) and 0.01% (solid line).

The electronic structures of the $\text{Sr}(\text{Ti}_{1-x}\text{Cr}_x)\text{O}_{3-\delta}$ NCs shown above suggest that both higher Cr^{3+} substitution yields and suppression of O_2^- anions in undoped NCs occur when N_2H_4 is present during the synthesis. The role of N_2H_4 in the formation mechanism of the O_2^- defect at the surface of undoped $\text{SrTiO}_{3-\delta}$ NCs and apparent effect on the incorporation of Cr^{3+} dopants is under current investigation. We propose the following tentative mechanism based on an existing model of O_2^- formation in TiO_2 ,³⁴⁻³⁵ which proceeds via electron transfer from Ti^{3+} to adsorbed O_2 as given by eq 2.1



We showed above that N_2H_4 , a reducing agent, hinders formation of O_2^- anions. Therefore, we propose that instead of reducing surface Ti^{4+} sites N_2H_4 is reducing surface V_{O} defects that ultimately produce surface V_{O} defects. The double-donor V_{O} defect is EPR silent. Therefore, during $\text{SrTiO}_{3-\delta}$ NC growth without N_2H_4 there are surface V_{O} or Ti^{3+}

defects that can transfer an electron to surface-adsorbed O₂. Experiments to clarify the role of N₂H₄ in the formation of O₂⁻ anion and promoting increased Cr³⁺ yields are currently underway.

2.4 Conclusions

We have presented two hydrothermal syntheses of substitutionally-doped Cr³⁺ in colloidal SrTiO_{3-δ} NCs with different oxygen-related defect structures. We find that N₂H₄ addition increases the overall efficiency of Cr³⁺ incorporation into the SrTiO_{3-δ} NC and also plays a critical role in controlling the nature of the surface defects. This study provides a simple synthetic path to preparing magnetically-doped SrTiO_{3-δ} NCs with tunable surface defects and enables integration of these technologically-relevant nanomaterials into new device architectures by means of existing solution-based processing techniques.

2.5 Supplementary Information

2.5.1 Charge Compensation in Sr(Ti_{1-x}Cr_x)O_{3-δ}. The concentration of Cr doped into the system (x) is the sum of Cr³⁺, Cr⁴⁺, and Cr⁶⁺. The lack of Cr⁵⁺ doped into SrTiO₃ is confirmed by the absence of a peak at $g=1.95$ in the EPR spectra.³⁸ The presence of Cr³⁺ substitutionally doped into the Ti⁴⁺ site requires charge compensation, either through the presence of Cr⁶⁺ or through a deficiency in the oxygen content ($\delta>0$). The variables x and δ include all possible oxidation states of substitutional Cr and V_O defects, and are represented by eqs 2.2 and 2.3 in Kröger-Vink notation:

$$x = [\text{Cr}'_{\text{Ti}}] + [\text{Cr}^{\times}_{\text{Ti}}] + [\text{Cr}^{\bullet\bullet}_{\text{Ti}}] \quad (2.2)$$

$$\delta = [V^{\bullet}_O] + [V^{\bullet\bullet}_O] \quad (2.3)$$

The Cr^{3+} (Cr'_{Ti}) concentration can thus be determined using eqs 2.2 and 2.3 with eq 2.4. Equation 2.4 takes into account the lack of spectroscopic evidence of Cr^{5+} or Ti^{3+} in the samples, but may slightly vary depending on trace amounts of either.

$$2[\text{Cr}'_{\text{Ti}}] = [\text{Cr}''_{\text{Ti}}] + 2[\text{V}_\text{O}^\bullet] + [\text{V}_\text{O}^{\bullet\bullet}] \quad (2.4)$$

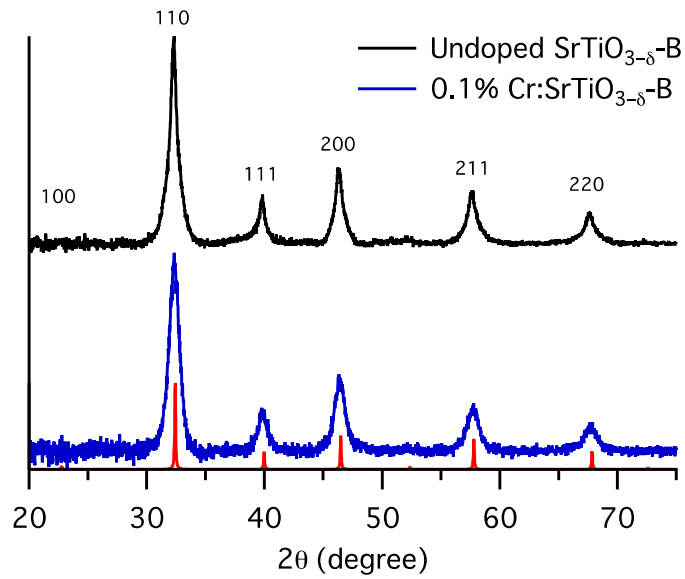


Figure 2.5. Powder X-ray diffraction patterns of $\text{SrTiO}_{3-\delta}\text{-B}$ (top) and nominally 0.1% $\text{Sr}(\text{Ti}_{1-x}\text{Cr}_x)\text{O}_{3-\delta}\text{-B}$ (bottom). The grain sizes estimated from the Scherrer equation are 15 nm for $\text{SrTiO}_{3-\delta}\text{-B}$ and 9 nm for nominally 0.1% $\text{Sr}(\text{Ti}_{1-x}\text{Cr}_x)\text{O}_{3-\delta}\text{-B}$. Red lines indicate the powder pattern of bulk SrTiO_3 .

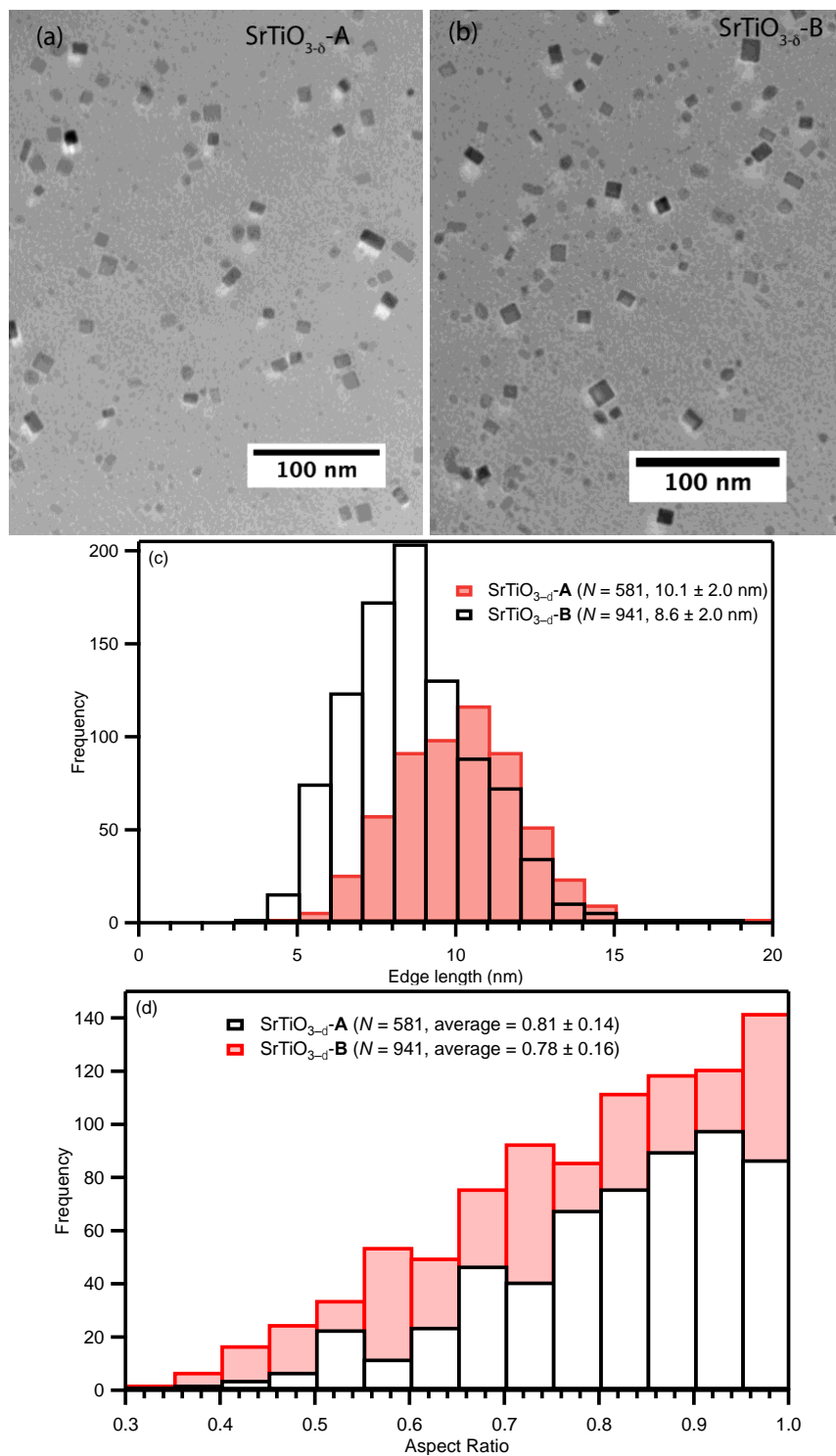


Figure 2.6. Representative TEM images of (a) SrTiO_{3-δ}-A and (b) SrTiO_{3-δ}-B NCs. (c) Particle size distribution and (d) aspect ratios obtained from analysis of TEM data for SrTiO_{3-δ}-A and SrTiO_{3-δ}-B.

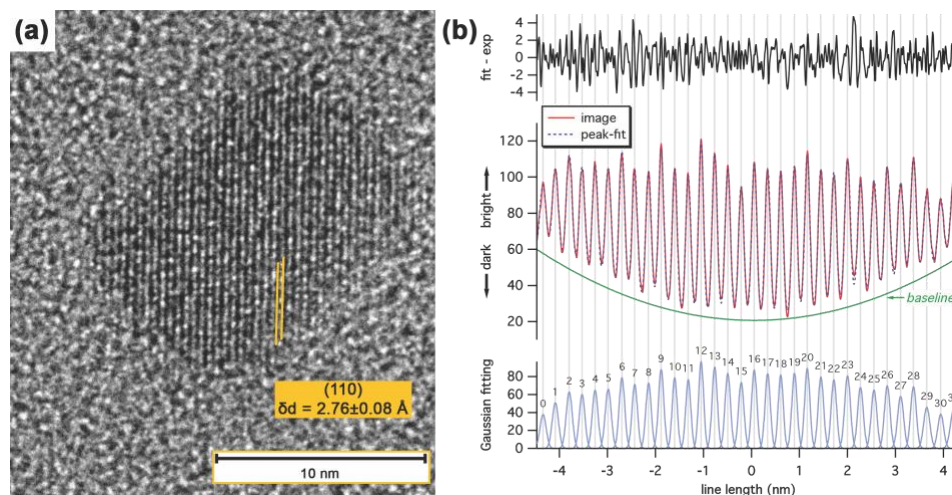


Figure 2.7. (a) Representative high-resolution TEM image and (b) rectangular color profile of the $\text{Sr}(\text{Ti}_{1-x}\text{Cr}_x)\text{O}_{3-\delta}\text{-B}$ NC shown in (a). The analysis was performed by first rotating the image so that the lattice fringes are vertical and then using the “plot profile” analysis function in ImageJ software on a rectangle encompassing the entire nanocrystal. The average lattice spacing is $2.76 \pm 0.08 \text{ \AA}$ and agrees well with the 2.76 \AA d-spacing of the (110) plane of SrTiO_3 .

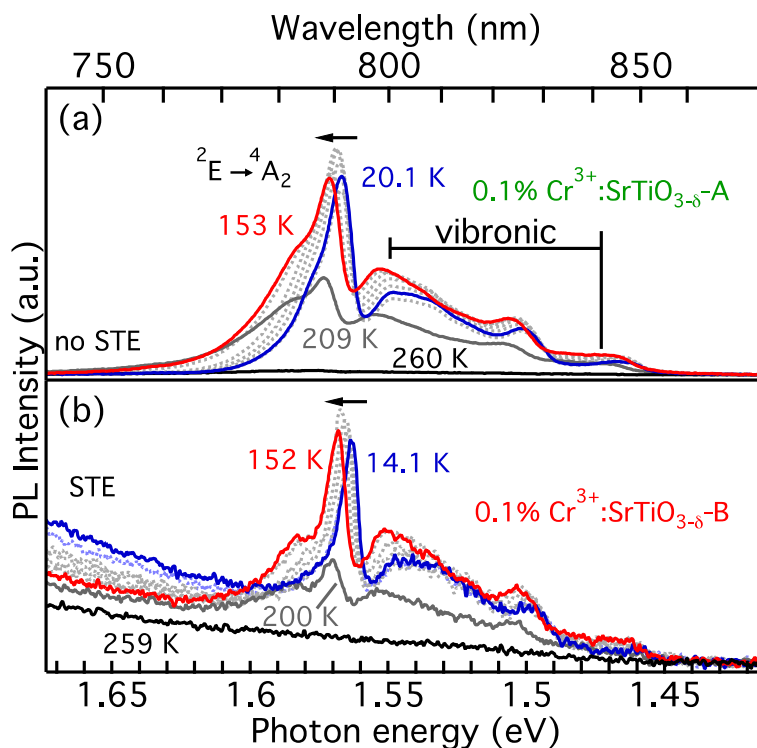


Figure 2.8. Variable-temperature photoluminescence spectrum of (a) $\text{Sr}(\text{Ti}_{1-x}\text{Cr}_x)\text{O}_{3-\delta}\text{-A}$ and (b) $\text{Sr}(\text{Ti}_{1-x}\text{Cr}_x)\text{O}_{3-\delta}\text{-B}$ NC powders. The spectra were collected with 488-nm laser excitation and the emitted light was detected using a Fourier transform (FT) spectrometer with 488 nm and 633 nm notch filters. The 633 nm notch filter is to remove laser emission from the HeNe alignment laser of the FT spectrometer.

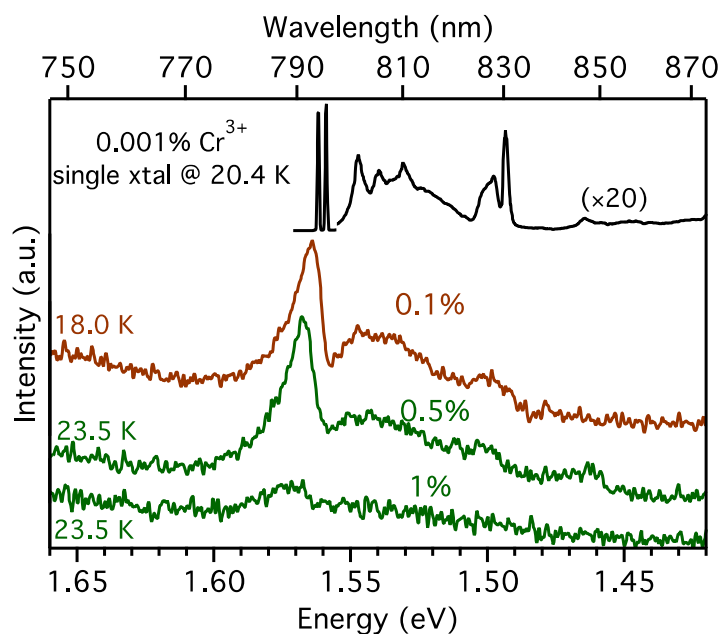


Figure 2.9. Low-temperature ${}^2E \rightarrow {}^4A_2$ emission $\text{Sr}(\text{Ti}_{1-x}\text{Cr}_x)\text{O}_{3-\delta}\text{-B}$ nanocrystal powders as a function of nominal Cr content, x . Excitation was the 488 nm line from an Ar^+ ion laser (JDS Uniphase). The literature emission from a 0.001% Cr^{3+} -doped SrTiO_3 single crystal at 20.4 K is included for comparison.²⁷

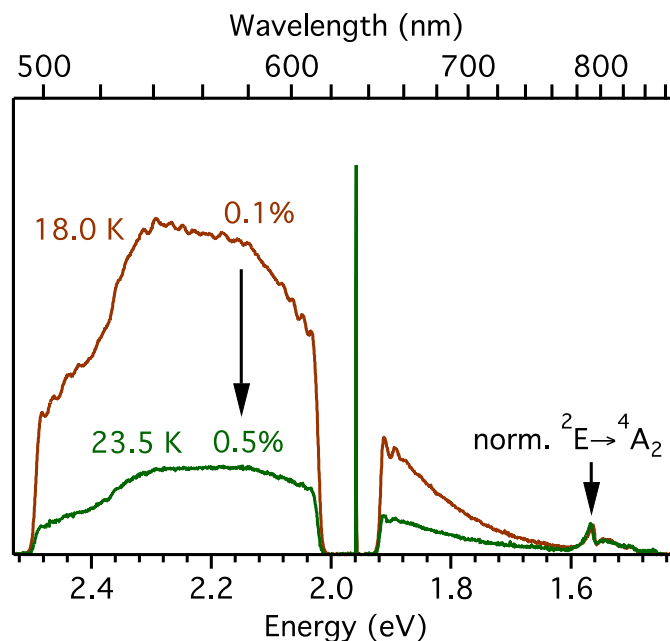


Figure 2.10. Comparison of the relative PL intensities of the visible STE emission for $\text{Sr}(\text{Ti}_{1-x}\text{Cr}_x)\text{O}_{3-\delta}\text{-B}$ NCs with nominal values of $x = 0.1\%$ and 0.5% . The intensities of the ${}^2E \rightarrow {}^4A_2$ transition for the two spectra are normalized. The broad STE-related emission from the undoped $\text{SrTiO}_{3-\delta}\text{-B}$ NC population in the ensemble is significantly reduced with the increase in nominal Cr^{3+} concentration. Excitation was the 488 nm line from an Ar^+ ion laser (JDS Uniphase). Sample temperatures are given in figure.

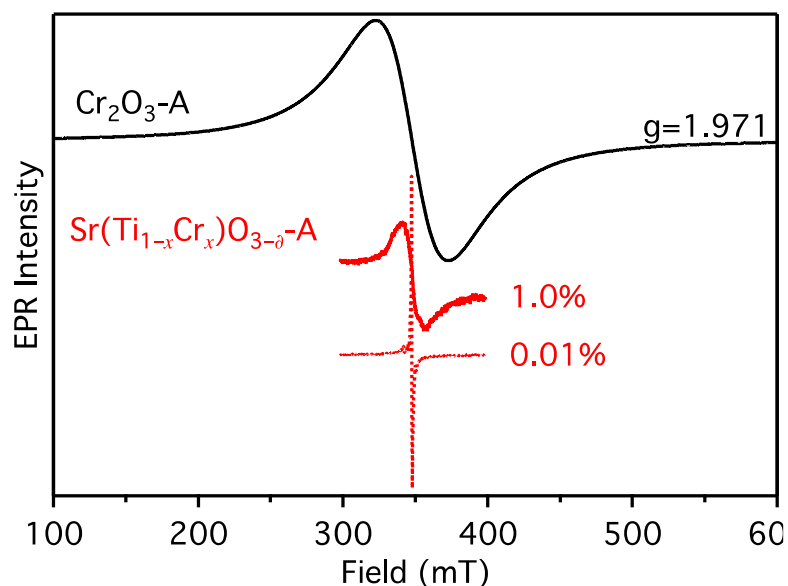


Figure 2.11. Room-temperature EPR spectra of “Cr₂O₃” and Sr(Ti_{1-x}Cr_x)O_{3-δ}-A nanocrystals where nominal $x = 0.01\%$ (dotted line) and 1% (solid line). The linewidth is much broader in “Cr₂O₃” from the antiferromagnetically-coupled Cr³⁺ ions.

Table 2.1 Comparison of measured Cr content (x) for Sr(Ti_{1-x}Cr_x)O_{3-δ} NCs prepared by methods A and B as a function of varying nominal x .

x_{nom}	ICP-OES method	
	A	B
0.1%	0.15%	0.09%
0.5%	0.99%	0.72%
1.0%	1.5%	1.8%

2.6 References

1. Ohtomo, A.; Hwang, H. Y. A High-Mobility Electron Gas at the LaAlO₃/SrTiO₃ Heterointerface. *Nature* **2004**, *427*, 423-426.
2. Guo, Y. Y.; Liu, H. M.; Yu, D. P.; Liu, J. M. Ferroelectricity and Superparamagnetism in Sr/Ti Nonstoichiometric SrTiO₃. *Phys. Rev. B* **2012**, *85*, 104108.
3. Warusawithana, M. P.; Cen, C.; Sleasman, C. R.; Woicik, J. C.; Li, Y.; Kourkoutis, L. F.; Klug, J. A.; Li, H.; Ryan, P.; Wang, L. P.; Bedzyk, M.; Muller, D. A.; Chen, L. Q.; Levy, J.; Schlom, D. G. A Ferroelectric Oxide Made Directly on Silicon. *Science* **2009**, *324*, 367-370.

4. Santander-Syro, A. F.; Fortuna, F.; Bareille, C.; Rodel, T. C.; Landolt, G.; Plumb, N. C.; Dil, J. H.; Radovic, M. Giant Spin Splitting of the Two-dimensional Electron Gas at the Surface of SrTiO₃. *Nat. Mater.* **2014**, *13*, 1085-1090.
5. Janousch, M.; Meijer, G. I.; Staub, U.; Delley, B.; Karg, S. F.; Andreasson, B. P. Role of Oxygen Vacancies in Cr-Doped SrTiO₃ for Resistance-Change Memory. *Adv. Mater.* **2007**, *19*, 2232-2235.
6. Meijer, G. I.; Staub, U.; Janousch, M.; Johnson, S. L.; Delley, B.; Neisius, T. Valence States of Cr and the Insulator-to-Metal Transition in Cr-doped SrTiO₃. *Phys. Rev. B* **2005**, *72*, 155102.
7. Townsend, T. K.; Browning, N. D.; Osterloh, F. E. Nanoscale Strontium Titanate Photocatalysts for Overall Water Splitting. *ACS Nano* **2012**, *6*, 7420-7426.
8. Wrighton, M. S.; Ellis, A. B.; Wolczanski, P. T.; Morse, D. L.; Abrahamson, H. B.; Ginley, D. S. Strontium Titanate Photoelectrodes. Efficient Photoassisted Electrolysis of Water at Zero Applied Potential. *J. Am. Chem. Soc.* **1976**, *98*, 2774-2779.
9. Mavroides, J. G.; Kafalas, J. A.; Kolesar, D. F. Photoelectrolysis of Water in Cells with SrTiO₃ Anodes. *Appl. Phys. Lett.* **1976**, *28*, 241-243.
10. van Benthem, K.; Elsässer, C.; French, R. H. Bulk Electronic Structure of SrTiO₃: Experiment and Theory. *J. Appl. Phys.* **2001**, *90*, 6156-6164.
11. Sasaki, Y.; Nemoto, H.; Saito, K.; Kudo, A. Solar Water Splitting Using Powdered Photocatalysts Driven by Z-Schematic Interparticle Electron Transfer without an Electron Mediator. *J. Phys. Chem. C* **2009**, *113*, 17536-17542.
12. Kato, H.; Kudo, A. Visible-Light-Response and Photocatalytic Activities of TiO₂ and SrTiO₃ Photocatalysts Codoped with Antimony and Chromium. *J. Phys. Chem. B* **2002**, *106*, 5029-5034.
13. Iwase, A.; Ng, Y. H.; Ishiguro, Y.; Kudo, A.; Amal, R. Reduced Graphene Oxide as a Solid-State Electron Mediator in Z-Scheme Photocatalytic Water Splitting under Visible Light. *J. Am. Chem. Soc.* **2011**, *133*, 11054-11057.
14. Wang, D.; Ye, J.; Kako, T.; Kimura, T. Photophysical and Photocatalytic Properties of SrTiO₃ Doped with Cr Cations on Different Sites. *J. Phys. Chem. B* **2006**, *110*, 15824-15830.
15. Kou, J.; Gao, J.; Li, Z.; Yu, H.; Zhou, Y.; Zou, Z. Construction of Visible-Light-Responsive SrTiO₃ with Enhanced CO₂ Adsorption Ability: Highly Efficient Photocatalysts for Artificial Photosynthesis. *Catal. Lett.* **2014**, *145*, 640-646.

16. Ju, L.; Sabergharesou, T.; Stampleskoskie, K. G.; Hegde, M.; Wang, T.; Combe, N. A.; Wu, H.; Radovanovic, P. V. Interplay between Size, Composition, and Phase Transition of Nanocrystalline Cr³⁺-doped BaTiO₃ as a Path to Multiferroism in Perovskite-Type Oxides. *J. Am. Chem. Soc.* **2011**, *134*, 1136-1146.
17. Park, K.; Son, J. S.; Woo, S. I.; Shin, K.; Oh, M.-W.; Park, S.-D.; Hyeon, T. Colloidal Synthesis and Thermoelectric Properties of La-doped SrTiO₃ Nanoparticles. *J. Mater. Chem. A* **2014**, *2*, 4217-4224.
18. Dang, F.; Mimura, K.-i.; Kato, K.; Imai, H.; Wada, S.; Haneda, H.; Kuwabara, M. Growth of Monodispersed SrTiO₃ Nanocubes by Thermohydrolysis Method. *Cryst. Eng. Comm.* **2011**, *13*, 3878-3883.
19. Fujinami, K.; Katagiri, K.; Kamiya, J.; Hamanaka, T.; Koumoto, K. Sub-10 nm Strontium Titanate Nanocubes Highly Dispersed in Non-polar Organic Solvents. *Nanoscale* **2010**, *2*, 2080-2083.
20. Rice, W. D.; Ambwani, P.; Bombeck, M.; Thompson, J. D.; Haugstad, G.; Leighton, C.; Crooker, S. A. Persistent Optically Induced Magnetism in Oxygen-Deficient Strontium Titanate. *Nat. Mater.* **2014**, *13*, 481-487.
21. Tan, H.; Zhao, Z.; Zhu, W. B.; Coker, E. N.; Li, B.; Zheng, M.; Yu, W.; Fan, H.; Sun, Z. Oxygen Vacancy Enhanced Photocatalytic Activity of Perovskite SrTiO₃. *ACS Appl. Mater. Interfaces* **2014**, *6*, 19184-19190.
22. Zhang, W. F.; Yin, Z.; Zhang, M. S.; Du, Z. L.; Chen, W. C. Roles of Defects and Grain Sizes in Photoluminescence of Nanocrystalline SrTiO₃. *J. Phys.: Condens. Matter* **1999**, *11*, 5655-5660.
23. Leonelli, R.; Brebner, J. L. Time-resolved Spectroscopy of the Visible Emission Band in Strontium Titanate. *Phys. Rev. B* **1986**, *33*, 8649-8656.
24. Eden, S.; Kapphan, S.; Hesse, H.; Trepakov, V.; Vikhnin, V.; Gregora, I.; Jastrabik, L.; Seglins, J. Observations of the Absorption, Infra-red Emission, and Excitation Spectra of Cr in BaTiO₃. *J. Phys.: Condens. Matter* **1998**, *10*, 10775-10786.
25. Lehuta, K. A.; Kittilstved, K. R. Speciation of Cr(III) in Intermediate Phases During the Sol-Gel Processing of Cr-doped SrTiO₃ Powders. *J. Mater. Chem. A* **2014**, *2*, 6138-6145.
26. Stokowski, S.; Schawlow, A. Dielectric-Related Optical Line Shifts in SrTiO₃:Cr³⁺. *Phys. Rev.* **1969**, *178*, 464-470.
27. Stokowski, S.; Schawlow, A. Spectroscopic Studies of SrTiO₃ Using Impurity-Ion Probes. *Phys. Rev.* **1969**, *178*, 457-464.

28. Trepakov, V. A.; Potucek, Z.; Makarova, M. V.; Dejneka, A.; Sazama, P.; Jastrabik, L.; Bryknar, Z. SrTiO₃:Cr Nanocrystalline Powders: Size Effects and Optical Properties. *J. Phys. Condens. Matter* **2009**, *21*, 375303.
29. McClure, D. S. Comparison of the Crystal Fields and Optical Spectra of Cr₂O₃ and Ruby. *J. Chem. Phys.* **1963**, *38*, 2289-2294.
30. Liu, W. K.; Whitaker, K. M.; Kittilstved, K. R.; Gamelin, D. R. Stable Photogenerated Carriers in Magnetic Semiconductor Nanocrystals. *J. Am. Chem. Soc.* **2006**, *128*, 3910-3911.
31. Naccache, C.; Meriaudeau, P.; Che, M.; Tench, A. J. Identification of Oxygen Species Adsorbed on Reduced Titanium Dioxide. *Trans. Faraday Soc.* **1971**, *67*, 506-512.
32. Müller, K. A. In *Proceedings of the First International Conference I, Paramagnetic Resonance*; Low, W., Ed.; Academic Press: New York, 1963; pp 17-43.
33. Bykov, I.; Makarova, M.; Trepakov, V.; Dejneka, A.; Yurchenko, L.; Yurchenko, L.; Jäger, A.; Jastrabik, L. Intrinsic and Impurity Defects in Chromium-doped SrTiO₃ Nanopowders: EPR and NMR Study. *Phys. Status Solidi B* **2013**, *250*, 821-824.
34. Lunsford, J. H. ESR of Adsorbed Oxygen Species. *Catal. Rev.* **1974**, *8*, 135-157.
35. Soria, J.; Sanz, J.; Sobrados, I.; Coronado, J. M.; Fresno, F.; Hernández-Alonso, M. D. Magnetic Resonance Study of the Defects Influence on the Surface Characteristics of Nanosize Anatase. *Catal. Today* **2007**, *129*, 240-246.
36. La Mattina, F.; Bednorz, J. G.; Alvarado, S. F.; Shengelaya, A.; Müller, K. A.; Keller, H. Controlled Oxygen Vacancies and Space Correlation with Cr³⁺ in SrTiO₃. *Phys. Rev. B* **2009**, *80*, 075122.
37. Rasband, W. S., ImageJ, U. S. National Institutes of Health, Bethesda, Maryland, USA, <http://imagej.nih.gov/ij/>, 1997-2015.
38. Badalyan, A. G.; Azamat, D.; Babunts, R. A.; Neverova, E. V.; Dejneka, A.; Trepakov, V. A.; Jastrabik, L. EPR study of charge compensation of chromium centers in the strontium titanate crystal. *Phys. Solid State* **2013**, *55*, 1454-1458.

CHAPTER 3

REVERSIBLE CONTROL OVER THE MANGANESE OXIDATION STATE IN COLLOIDAL STRONTIUM TITANATE NANOCRYSTALS

3.1 Introduction

Mn-doped strontium titanate is a promising material due to its various applications in ferroelectrics,¹⁻² photocatalytic water splitting,³⁻⁶ magnetism,⁷⁻⁹ and capacitance.¹⁰ Mn has been reported to exist in a multitude of oxidation states, Mn^{2+} , Mn^{3+} , and Mn^{4+} when incorporated into SrTiO_3 . It is well known that Mn^{4+} exclusively substitutes for Ti^{4+} with no local charge compensation. However, Mn^{2+} has been reported to substitute for both Sr^{2+} and Ti^{4+} with and without local charge compensation.^{7-9, 11} There is a lot of inconsistency regarding the doping position of Mn^{2+} .

Mn^{4+} : SrTiO_3 has been reported to have applications as a visible light catalyst for water splitting. Mn^{4+} is isovalent with Ti^{4+} and isoelectronic with Cr^{3+} , a known visible light photocatalyst.¹²⁻¹³ The inherent problem with using Cr^{3+} is the formation of undesirable defects such as Cr^{6+} to maintain charge neutrality. Cr^{6+} is known to act as recombination centers and must be removed by co-doping, chemical reductions or other post-synthetic modifications.¹⁴⁻¹⁷ Since Mn^{4+} is isovalent with Ti^{4+} , there should be no need for charge compensation mechanisms such as oxygen vacancies or higher Mn valence states and therefore no post-synthetic modifications should be needed. Due to this difference, Mn can serve as a potential replacement for Cr for these visible light photocatalysts. Due to their high dielectric and insulating properties, SrTiO_3 and BaTiO_3 also have applications in electronics as high dielectric materials.¹⁸⁻²⁰ Mn^{4+} : BaTiO_3 has

been reported to increase the insulating properties by serving as trap centers to localize electrons.²¹ Conversely, Mn^{2+} or $\text{Mn}^{2+-\text{v}_\text{O}}$ at the Ti site with high oxygen vacancy concentrations has been reported to induce a conversion from insulating to a metallic state.²² Control over both dopant location and oxidation are both extremely important factors for imparting property-based functionality into SrTiO_3 .

We previously reported the synthesis and characterization of $\text{Cr}^{3+}:\text{SrTiO}_3$ using two hydrothermal methods, one with hydrazine and the other without noted method A and B respectively. In that study, we confirmed through EPR and low-temperature photoluminescence (PL) that both methods yielded substitutionally doped Cr^{3+} at the Ti^{4+} site. We also observed different surface related defects depending on whether hydrazine or a dopant was used or not. Herein we report the oxidation state of substitutional Mn exclusively at the Ti site in colloidal SrTiO_3 nanocrystals. We used a myriad of physical characterization techniques to confirm the formation of phase pure highly crystalline SrTiO_3 including high-resolution transmission electron microscopy (HRTEM) and powder X-ray diffraction (XRD). Dopant-specific spectroscopies such as EPR were employed to identify the Mn oxidation state. We used photoirradiation to probe the changes in Mn valency when doped into colloidal SrTiO_3 NCs.

3.2 Experimental Methods

3.2.1 Materials. $\text{Sr}(\text{OH})_2 \cdot 8\text{H}_2\text{O}$ (99%, Alfa Aesar), titanium(IV) bis(ammonium lactate)dihydroxide (TiALH, 50% wt in water, Alfa Aesar), $\text{Mn}(\text{NO}_3)_2 \cdot 4\text{H}_2\text{O}$ (analytical grade, Acros Organics), tetramethylammonium hydroxide (10 M NMe_4OH , Acros Organics), hydrazine hydrate ($\text{N}_2\text{H}_4 \cdot \text{H}_2\text{O}$, 99%, Acros Organics), oleic acid (90%, Fisher

Chemical), ethanol (200 proof, PHARMCO-AAPER) and hexanes (optima, Fisher Chemical) were used as received.

3.2.2 Synthesis of colloidal Mn: SrTiO₃ nanocrystals. Colloidal SrTiO₃ NCs were prepared using a previously reported modified hydrothermal method using manganese as the dopant.²³⁻²⁴ Method A is characterized by the use of hydrazine and method B is without hydrazine. The colloidal samples were utilized without further modifications. Powder samples were obtained by precipitating the colloids out using ethanol and then allowing them to air dry.

3.2.3 Physical Methods. Room-temperature electronic absorption spectra were collected on colloidal suspensions in hexanes with a Cary 50 Bio spectrometer. Electron paramagnetic resonance (EPR) spectroscopy were collected on colloidal suspensions in hexanes and powdered samples with continuous wave at X-band frequency (~9.6 GHz, Bruker Elexsys-500). X-ray powder diffraction patterns were collected using Cu-K α radiation (PAN-alytical X'Pert Material Research Diffractometer). Transmission electron microscopy images were collected on samples deposited onto a carbon film supported on 400 mesh copper grids at the UMass Amherst Electron Microscopy Center (HR-TEM, JEM 2200FS-JEOL, 200 kV). Photodoping experiments were performed by irradiating the sample (in a cuvette or EPR tube) with a 75-W or 1000-W Xe arc lamp in the presence or absence of a hole quencher.

3.3 Results and Discussion

3.3.1 Structural characterization

Powder X-ray diffraction (XRD) was used to confirm both the crystallinity and phase purity of the synthesized NCs. XRD of as-prepared 0.1% Mn: SrTiO₃ NCs shows phase pure strontium titanate with ~8 nm highly crystalline particles evident from comparisons to simulated diffraction patterns of SrTiO₃ shown in figure 3.1. Particle sizes were calculated from the average of the FWHM of each peak and averaged using the Scherrer equation. There were no detectable impurity phases present in the diffraction pattern. HRTEM was utilized to corroborate the crystallinity and calculated particle sizes from PXRD yielding sizes of ~7 nm. A rectangular color profile analysis was utilized in ImageJ software to yield interplanar spacings of 2.20 ± 0.02 Å matching well to the calculated d-spacing of the (111) plane in SrTiO₃ of 2.25 Å. A Fast Fourier transform analysis indicates single crystalline morphology, highlighting three distinct planes, the (111), (211) and (222) planes from the calculated d-spacings of 2.2 Å, 1.6 Å, and 1.1 Å respectively. From the structural analysis, changing the dopant from chromium to manganese does not alter the structure, morphology, or crystallinity of the SrTiO₃ colloidal NCs.

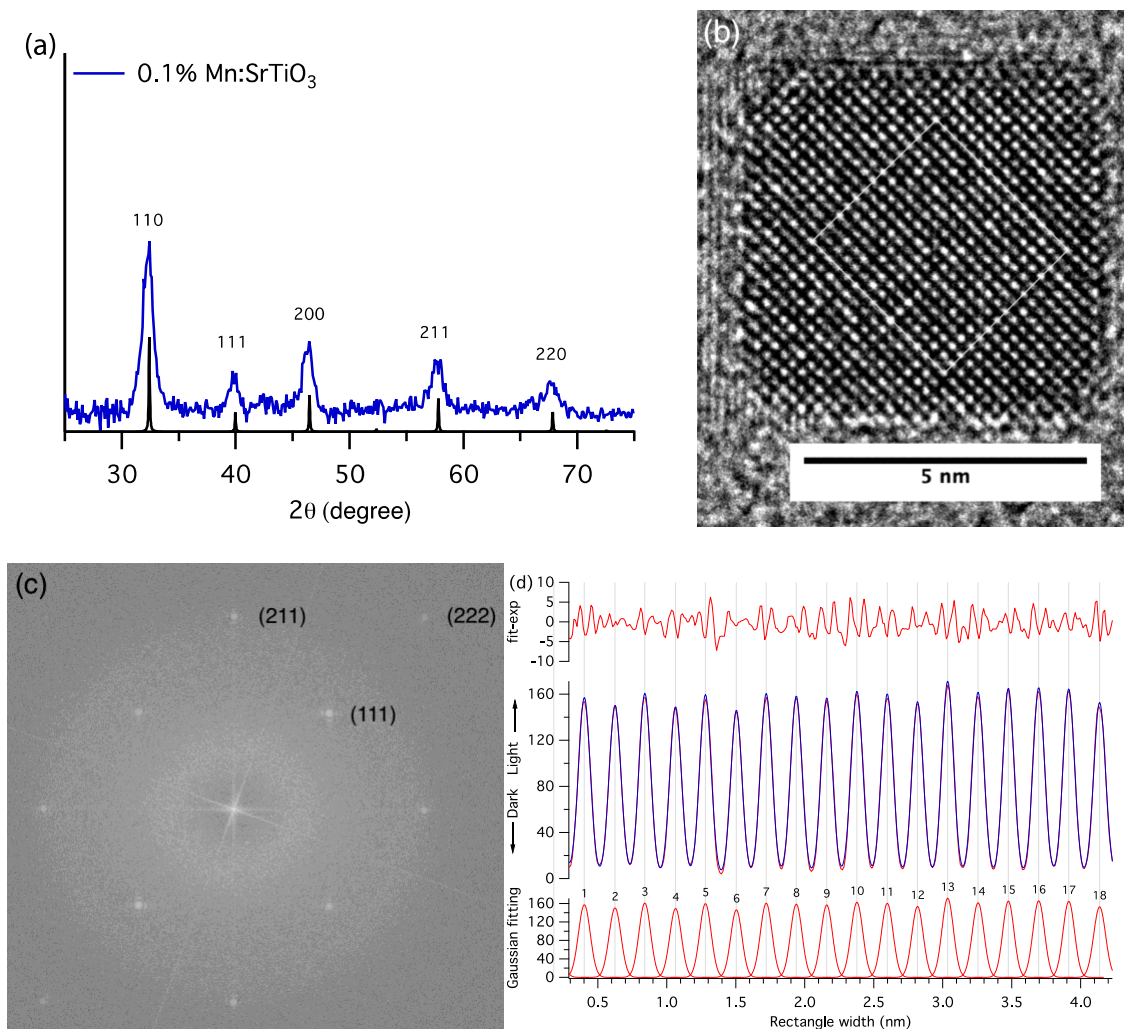


Figure 3.1a: Powder X-ray diffraction pattern of as prepared-0.1% Mn-SrTiO₃. Particle sizes calculated from the Scherrer equation yield ~ 8 nm particles. (b) The HRTEM indicates ~ 7 nm cubic nanocrystals. (c) Fast Fourier transform (FFT) displaying the (111), (211) and (222) planes with measured d-spacings of 2.2 Å, 1.6 Å, and 1.1 Å respectively. (d) The rectangular color plot profile analysis performed in ImageJ is shown in (b). The calculated interplanar spacings 2.20 ± 0.02 Å agrees well with 2.25 Å, the d-spacing of the (111) plane.

3.3.2 Electronic structure characterizations

The electronic absorption spectra for concentrated method A and B Mn: SrTiO₃, shown in figure 3.2, displays only the bandgap absorption above ~ 385 nm. The broad absorption tailing into the visible region for method B is attributed to various oxygen-

related defects present comparable to those seen in colloidal Cr: SrTiO₃ NCs.²⁵⁻²⁶ The oxidation state of manganese was expected to exist as Mn⁴⁺, isovalent with titanium when doped into SrTiO₃. The characteristic d³, Mn⁴⁺ ⁴A₂→⁴T₂ ligand field transition reported to occur at 556 nm was not observed in these colloidal NCs.²⁷ This observation could indicate one of two possibilities, (1) manganese is not doping primarily as Mn⁴⁺ into the NCs and may exist as either Mn³⁺ or Mn²⁺, or (2) the concentration of internally doped Mn ions is not large enough to observe these ligand field transitions. To resolve the speciation of Mn, EPR was utilized to determine the oxidation state and doping environment.

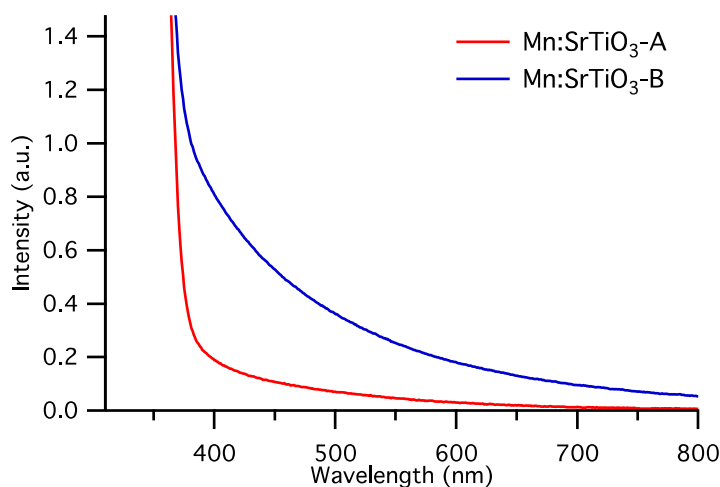


Figure 3.2: Concentrated electronic absorption spectra of 0.1% Mn:SrTiO₃ method A and B colloidal NCs. The broad absorption into the visible region in B is due to various oxygen related defects.

EPR spectroscopy was used to determine the oxidation state and local environment of manganese. As can be seen in figure 3.3, there is a stark difference between Method A₁ and A₂ and Method B₁ and B₂. Both sets of samples were synthesized under the same conditions respective of their method, the difference between the two sets of samples was the time between when the measurement was taken and how the sample was stored. Samples A₁ and B₁ were taken immediately after synthesis, while samples A₂ and B₂ were

left under ambient light conditions. In A₁ and B₁, a weak set of sextet peaks arising from the nuclear hyperfine of ⁵⁵Mn (I=5/2, 100% abundance) can be seen. The g-value for this set of sextet peaks was calculated to be 1.998 with A=71.4 x 10⁻⁴ cm⁻¹. Mn-doped into SrTiO₃ has been reported as Mn⁴⁺ or Mn²⁺ at the B-site from numerous literature reports that utilized EPR spectroscopy.^{8, 11, 22, 28-30} The calculated g and A values for A₁ and B₁ are consistent with Mn⁴⁺ substituting for Ti⁴⁺ (g=1.994 and A=69.4 x 10⁻⁴ cm⁻¹).²⁹ The peak at 3476 G is due to a small Cr impurity (marked with *). The peak corresponding to g=2.003 observed in method B has been previously reported and assigned to adsorbed superoxide (O₂⁻) on the surface.^{24, 31-32} The g-value for the larger set of sextet peaks seen in samples A₂ and B₂ was calculated to be 2.007 with a hyperfine splitting constant A= 79.3 x 10⁻⁴ cm⁻¹. Mn⁴⁺ appears to be absent from samples A₂ and B₂. Mn²⁺ can substitute either for Ti⁴⁺ or Sr²⁺ as well as form Mn²⁺-v_o complexes at the B-site.^{8, 22} B-site substitutional Mn²⁺ without local charge compensation has been reported to have g=2.0032 and A=82.8 x 10⁻⁴ cm⁻¹.¹¹ Under reducing conditions, Mn²⁺-v_o complexes with doubly ionized oxygen vacancies in the first coordination sphere have reported g-values of 2.003 with A=76.1 x 10⁻⁴ cm⁻¹.¹¹ However, A-site substitution is expected to have larger A values (>90 x 10⁻⁴ cm⁻¹) for a dodecahedrally coordinated environment.^{29, 33} Mn³⁺ substituting for Ti⁴⁺ is another possibility but is not observable in X-band frequencies due to being S=2, exhibiting a large zero-field splitting and thus is EPR silent. It is clear from the calculated g and A values for A₂ and B₂ that Mn is not substituting for Sr²⁺, but for Ti⁴⁺. However, the calculated hyperfine constant is very close to both assignments of substitutional Mn²⁺ with and without local charge compensation.

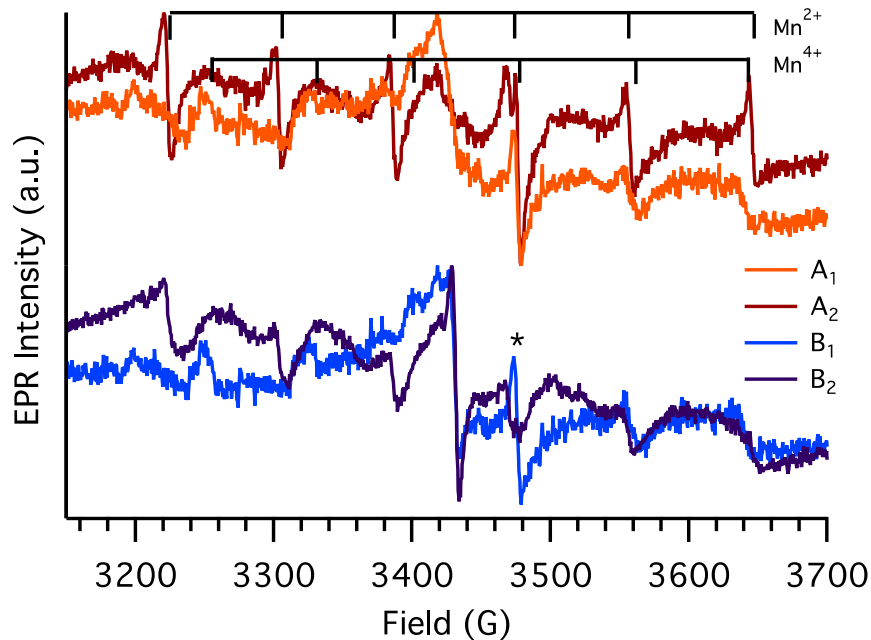


Figure 3.3: Room temperature EPR of two sets of synthesized method A and B, Mn: SrTiO₃ samples. A₁ and B₁ were measured immediately after being synthesized. A₂ and B₂ were measured a week after being synthesized and stored in ambient light.

3.3.3 Probing the valance state with photochemical reductions

To investigate the impact light has on Mn: SrTiO₃ NCs, we utilized controlled light irradiation to probe the nature of this observed difference in the EPR spectra. The colloidal suspensions were irradiated with a 75 W lamp for several hours and then measured. As seen in figure 3.4, the weak sextet peaks of Mn⁴⁺ disappear for both samples A₁ and B₁, and a new set of sextet peaks appear with $g=2.007$ and A value of $79.3 \times 10^{-4} \text{ cm}^{-1}$. The g and A value of this new set of peaks align with the g and A values calculated in samples A₂ and B₂. Concurrently with the disappearance of Mn⁴⁺, a new signal at 3420 G ($g=2.009$) appears in all photo-irradiated samples. This feature has been reported to arise from trapped holes.³² For samples A₂ and B₂, the peak intensities just increase with photo-irradiation. The increase in the intensity of the Mn²⁺ signal in A₂ and B₂ indicates the possibility of

Mn^{3+} since Mn^{4+} was not originally observed in the as-prepared samples. Through the introduction of light, we observe a reduction of the Mn valance state from Mn^{4+} to Mn^{2+} in A_1 and B_1 and an increase in intensity for A_2 and B_2 . Further investigation into the speciation of Mn in these colloidal NCs are currently underway.

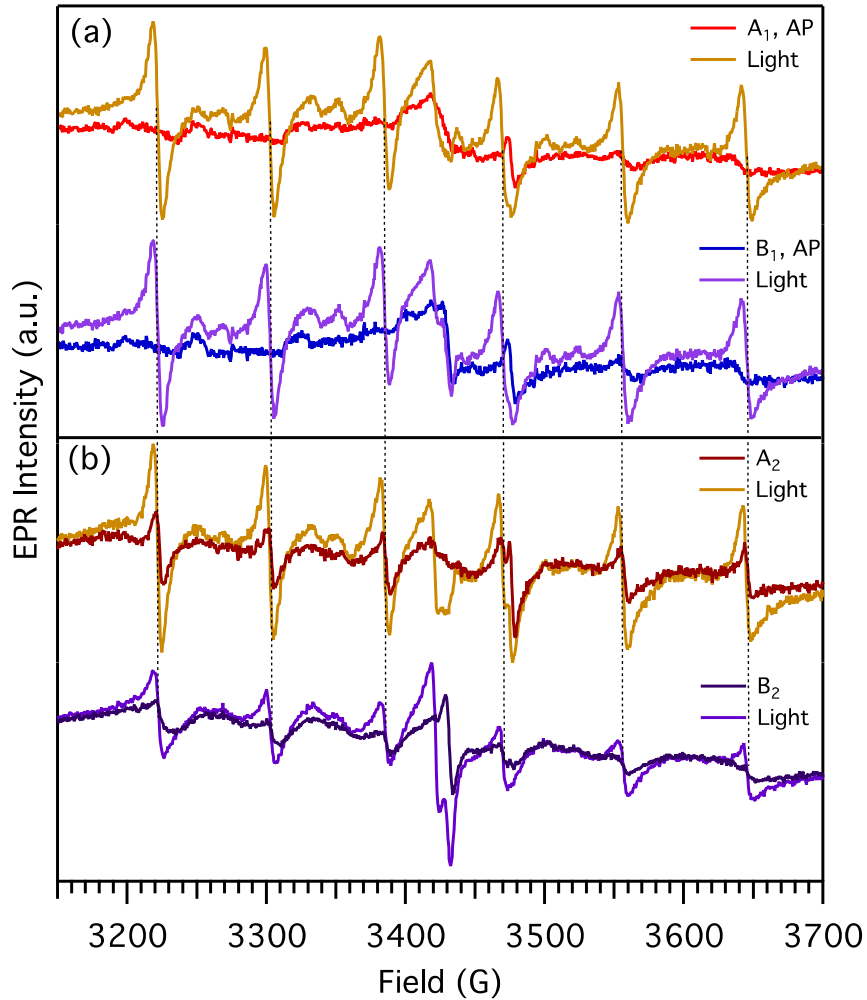


Figure 3.4: Room temperature EPR of colloidal as prepared and after photoirradiation, (a) A_1 and B_1 (b) A_2 and B_2 . Each sample was irradiated with a 75 W lamp for 3 hours and then measured immediately.

When $\text{Mn}:\text{SrTiO}_3$ is left in the dark for a period of time, the photo-induced changes are oxidized back to Mn^{4+} as seen in figure 3.5. This shows the oxidative and reductive changes are reversible under light and dark conditions. The increase in Mn^{4+} intensity under

dark conditions compared to the as-prepared samples indicates the possible presence of EPR silent species. Experiments are currently underway to investigate the exact nature of this observed reversibility of the light-induced reduction/oxidation.

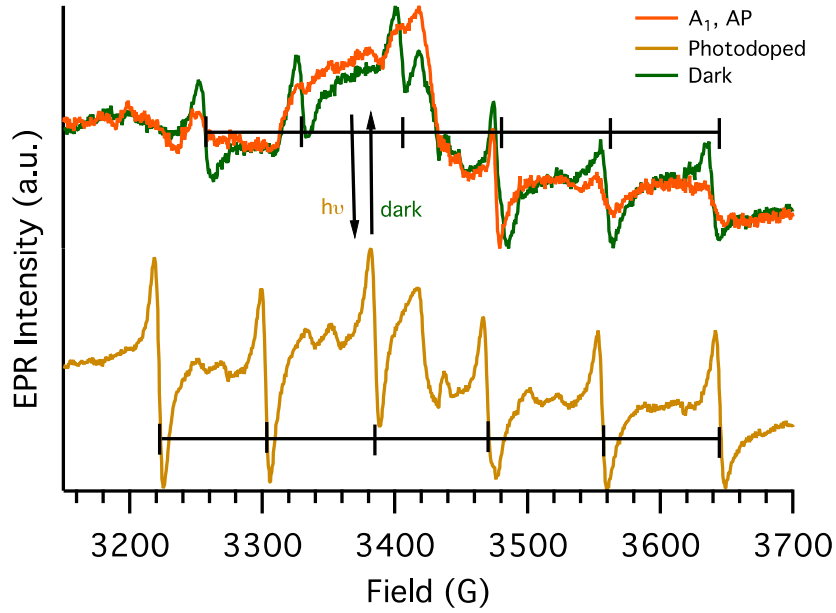


Figure 3.5: Photo-reversibility of Mn:SrTiO₃-A₁ in both light and dark conditions. The sample was left in the dark for 7 days and then measured.

Low-temperature EPR was used to identify which Mn²⁺ species was present in A₂ and B₂ (figure 3.4). The EPR peak intensity increased when the sample was cooled down to 120 K, indicating that the large sextet in A₂ and B₂ are not from Mn²⁺ without local charge compensation. The EPR signal intensity would have gradually disappeared when cooled down to 120 K if Mn²⁺ was present due to antiferromagnetic interactions. A similar temperature dependent trend was reported for MnO and in Mn: SrTiO₃ powders.^{28, 30} It is likely that Mn²⁺-v_o complexes with doubly ionized oxygen vacancies in the first coordination sphere are present in A₂ and B₂ and when photo-irradiated (vide infra).

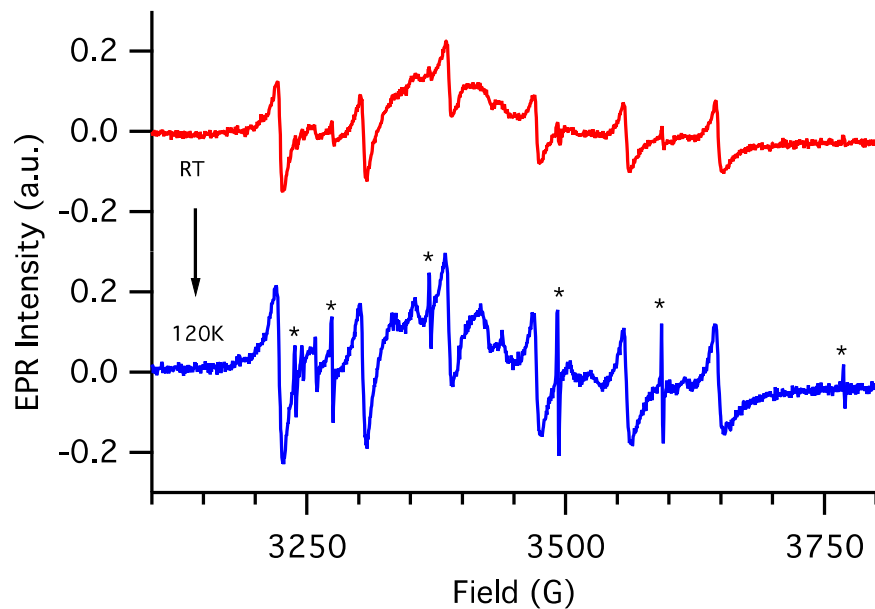


Figure 3.6: Room temperature EPR spectra of colloidal $\text{Mn}^{2+}:\text{SrTiO}_3\text{-A}_1$ (top). EPR spectra of colloidal $\text{Mn}^{2+}:\text{SrTiO}_3\text{-A}_1$ at 120 K (bottom). Impurities from the cryostat at low temperatures are marked with an asterisk.

Mn -doped SrTiO_3 bulk powders were used to corroborate the EPR assignments for the colloidal Mn -doped SrTiO_3 NCs. Previous work done in our lab on bulk SrTiO_3 showed the emergence of multivalent Mn in reduced SrTiO_3 as seen in figure 3.7. Reductions on SrTiO_3 bulk powders were done using NaBH_4 and annealed at $300\text{ }^\circ\text{C}$. Three separate sets of sextet signals can be seen in Mn -doped SrTiO_3 bulk powders. The largest set of sextet peaks were attributed to Ti^{4+} substituted Mn^{4+} ($g=1.994$ and $A=69.4 \times 10^{-4} \text{ cm}^{-1}$). The weakest set of peaks was attributed to Ti^{4+} substituted Mn^{2+} ($g=2.004$ and $A=82.3 \times 10^{-4} \text{ cm}^{-1}$). The intermediate set of peaks was attributed to Ti^{4+} substituted $\text{Mn}^{2+}\text{-}v_0$ complexes ($g=2.003$ and $A=76 \times 10^{-4} \text{ cm}^{-1}$). $\text{Mn}^{2+}\text{-}v_0$ complexes are well reported and are known to form under highly reducing atmospheres and at high temperatures.³⁴ The $\text{Mn}^{2+}\text{-}v_0$ complexes observed in the bulk powders were formed under reducing conditions and at moderate temperatures. The large set of peaks in the photo-irradiated Mn -doped SrTiO_3

NCs align well to the $\text{Mn}^{2+}\text{-v}_0$ complexes in reduced Bulk Mn-doped SrTiO_3 . These results lead to the tentative assignment of $\text{Mn}^{2+}\text{-v}_0$ in as prepared A₂ and B₂ and in all photo-irradiated samples. Further experiments to probe this finding are currently underway.

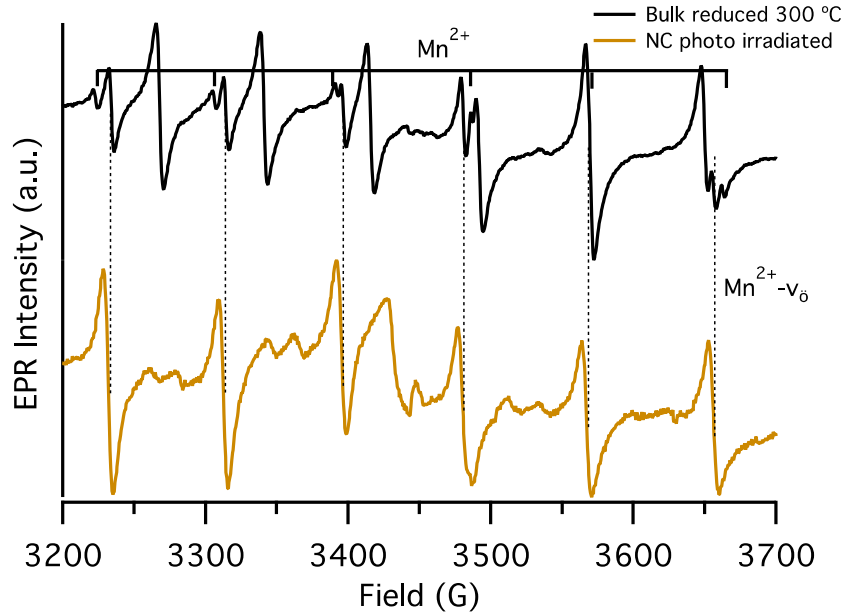


Figure 3.7: Room temperature EPR spectra of 0.1% Mn:SrTiO₃ bulk powders reduced at 300° C using NaBH₄ as a reductant (top). Photo-irradiated 0.1% Mn:SrTiO₃-A₁ NCs (bottom).

3.4 Conclusions

The tunability of manganese oxidation states in colloidal Mn-doped SrTiO₃ NCs, synthesized using a modified hydrothermal synthesis method was studied using EPR. Colloidal Mn-doped SrTiO₃ NCs and intrinsic defects were probed using photo-irradiation. We found that the oxidation state of Mn is multivalent in the as-prepared samples and was sensitive to the exposure to ambient light conditions. The EPR, when irradiated, showed a decrease in Mn⁴⁺ intensity and an increase in Mn²⁺ intensity, which we tentatively assign to Mn²⁺-v₀ complexes. This is supported through the findings in low-temperature EPR and matching signals in EPR for reduced bulk Mn-doped SrTiO₃. We observed an increase in

Mn EPR signal intensity at low temperature rather than an expected decrease for Mn^{2+} . We demonstrate the reversibility of this observed reduction/oxidation through the presence/absence of light respectively. The tentatively assigned $\text{Mn}^{2+}\text{-}v_0$ complex oxidizes back to Mn^{4+} when left in the dark. This facile method offers a way reversibly generate $\text{Mn}^{2+}\text{-}v_0$ with just light rather than having to use high temperatures or strongly reducing conditions, exhibiting tunability and control over manganese oxidation states.

3.5 References

1. Valant, M.; Kolodiazny, T.; Arçon, I.; Aguesse, F.; Axelsson, A.-K.; Alford, N. M., The Origin of Magnetism in Mn-Doped SrTiO_3 . *Adv. Funct. Mater.* **2012**, *22* (10), 2114-2122.
2. Bryknar, Z.; Trepakov, V.; Potůček, Z.; Jastrabík, L., Luminescence spectra of $\text{SrTiO}_3\text{:Mn}^{4+}$. *J. Lumin.* **2000**, *87-89*, 605-607.
3. Zhou, X.; Shi, J.; Li, C., Effect of Metal Doping on Electronic Structure and Visible Light Absorption of SrTiO_3 and NaTaO_3 (Metal = Mn, Fe, and Co). *J. Phys. Chem. C* **2011**, *115* (16), 8305-8311.
4. Yang, H.; Kan, K.; Ouyang, J.; Li, Y., Solvothermal synthesis and optical properties of Mn^{2+} -doped SrTiO_3 powders. *J. Alloys Compd.* **2009**, *485* (1-2), 351-355.
5. Konta, R.; Ishii, T.; Kato, H.; Kudo, A., Photocatalytic Activities of Noble Metal Ion Doped SrTiO_3 under Visible Light Irradiation. *J. Phys. Chem. B* **2004**, *108* (26), 8992-8995.
6. Sun, X.; Lin, J., Synergetic Effects of Thermal and Photo-Catalysis in Purification of Dye Water over $\text{SrTi}_{1-x}\text{Mn}_x\text{O}_3$ Solid Solutions. *J. Phys. Chem. C* **2009**, *113* (12), 4970-4975.
7. Tkach, A.; Vilarinho, P. M.; Kholkin, A. L., Structure–microstructure–dielectric tunability relationship in Mn-doped strontium titanate ceramics. *Acta Mater.* **2005**, *53* (19), 5061-5069.
8. Choudhury, D.; Mukherjee, S.; Mandal, P.; Sundaresan, A.; Waghmare, U. V.; Bhattacharjee, S.; Mathieu, R.; Lazor, P.; Eriksson, O.; Sanyal, B.; Nordblad, P.; Sharma, A.; Bhat, S. V.; Karis, O.; Sarma, D. D., Tuning of dielectric properties

- and magnetism of SrTiO₃ by site-specific doping of Mn. *Phys. Rev. B* **2011**, *84* (12).
9. Zorko, A.; Pregelj, M.; Luetkens, H.; Axelsson, A. K.; Valant, M., Intrinsic paramagnetism and aggregation of manganese dopants in SrTiO₃. *Phys. Rev. B* **2014**, *89* (9).
 10. Baumert, B. A.; Chang, L. H.; Matsuda, A. T.; Tsai, T. L.; Tracy, C. J.; Gregory, R. B.; Fejes, P. L.; Cave, N. G.; Chen, W.; Taylor, D. J.; Otsuki, T.; Fujii, E.; Hayashi, S.; Suu, K., Characterization of sputtered barium strontium titanate and strontium titanate-thin films. *J. Appl. Phys.* **1997**, *82* (5), 2558-2566.
 11. Laguta, V. V.; Kondakova, I. V.; Bykov, I. P.; Glinchuk, M. D.; Tkach, A.; Vilarinho, P. M.; Jastrabik, L., Electron spin resonance investigation of Mn²⁺ ions and their dynamics in Mn-doped SrTiO₃. *Phys. Rev. B* **2007**, *76* (5).
 12. Reunchan, P.; Ouyang, S.; Umezawa, N.; Xu, H.; Zhang, Y.; Ye, J., Theoretical design of highly active SrTiO₃-based photocatalysts by a codoping scheme towards solar energy utilization for hydrogen production. *J. Mater. Chem. A* **2013**, *1* (13).
 13. Reunchan, P.; Umezawa, N.; Ouyang, S.; Ye, J., Mechanism of photocatalytic activities in Cr-doped SrTiO₃ under visible-light irradiation: an insight from hybrid density-functional calculations. *Phys. Chem. Chem. Phys.* **2012**, *14* (6), 1876-80.
 14. Kato, H.; Kudo, A., Visible-Light-Response and Photocatalytic Activities of TiO₂ and SrTiO₃ Photocatalysts Codoped with Antimony and Chromium. *J. Phys. Chem. B* **2002**, *106* (19), 5029-5034.
 15. Kang, H. W.; Park, S. B., H₂ evolution under visible light irradiation from aqueous methanol solution on SrTiO₃:Cr/Ta prepared by spray pyrolysis from polymeric precursor. *Int. J. Hydrogen Energy* **2011**, *36* (16), 9496-9504.
 16. Ouyang, S.; Tong, H.; Umezawa, N.; Cao, J.; Li, P.; Bi, Y.; Zhang, Y.; Ye, J., Surface-alkalinization-induced enhancement of photocatalytic H₂ evolution over SrTiO₃-based photocatalysts. *J. Am. Chem. Soc.* **2012**, *134* (4), 1974-7.
 17. Zuo, F.; Wang, L.; Wu, T.; Zhang, Z.; Borchardt, D.; Feng, P., Self-doped Ti³⁺ enhanced photocatalyst for hydrogen production under visible light. *J. Am. Chem. Soc.* **2010**, *132* (34), 11856-7.
 18. Balaya, P.; Ahrens, M.; Kienle, L.; Maier, J.; Rahmati, B.; Lee, S. B.; Sigle, W.; Pashkin, A.; Kuntscher, C.; Dressel, M., Synthesis and Characterization of Nanocrystalline SrTiO₃. *J. Am. Ceram. Soc.* **2006**, *0* (0), 2804-2811
 19. Meyer, R.; Zurhelle, A. F.; De Souza, R. A.; Waser, R.; Gunkel, F., Dynamics of the metal-insulator transition of donor-doped SrTiO₃. *Phys. Rev. B* **2016**, *94* (11).

20. Böttcher, R.; Klimm, C.; Michel, D.; Semmelhack, H. C.; Völkel, G.; Gläsel, H. J.; Hartmann, E., Size effect in Mn²⁺-doped BaTiO₃ nanopowders observed by electron paramagnetic resonance. *Phys. Rev. B* **2000**, *62* (3), 2085-2095.
21. Wang, X.; Gu, M.; Yang, B.; Zhu, S.; Cao, W., Hall effect and dielectric properties of Mn-doped barium titanate. *Microelectron. Eng.* **2003**, *66* (1-4), 855-859.
22. Choudhury, D.; Pal, B.; Sharma, A.; Bhat, S. V.; Sarma, D. D., Magnetization in electron- and Mn-doped SrTiO₃. *Sci. Rep.* **2013**, *3*, 1433.
23. Fujinami, K.; Katagiri, K.; Kamiya, J.; Hamanaka, T.; Koumoto, K., Sub-10 nm strontium titanate nanocubes highly dispersed in non-polar organic solvents. *Nanoscale* **2010**, *2* (10), 2080-3.
24. Harrigan, W. L.; Michaud, S. E.; Lehuta, K. A.; Kittilstved, K. R., Tunable Electronic Structure and Surface Defects in Chromium-Doped Colloidal SrTiO_{3-δ} Nanocrystals. *Chem. Mater.* **2016**, *28* (2), 430-433.
25. Rice, W. D.; Ambwani, P.; Bombeck, M.; Thompson, J. D.; Haugstad, G.; Leighton, C.; Crooker, S. A., Persistent optically induced magnetism in oxygen-deficient strontium titanate. *Nat. Mater.* **2014**, *13* (5), 481-7.
26. Mitra, C.; Lin, C.; Robertson, J.; Demkov, A. A., Electronic structure of oxygen vacancies in SrTiO₃ and LaAlO₃. *Phys. Rev. B* **2012**, *86* (15).
27. Badalyan, A. G.; Azzoni, C. B.; Galinetto, P.; Mozzati, M. C.; Trepakov, V. A.; Savinov, M.; Deyneka, A.; Jastrabik, L.; Rosa, J., Impurity centers and host microstructure in weakly doped SrTiO₃:Mn crystals: new findings. *J. Phys. Conf. Ser.* **2007**, *93*.
28. Azzoni, C. B.; Mozzati, M. C.; Paleari, A.; Massarotti, V.; Bini, M.; Capsoni, D., Magnetic evidence of different environments of manganese ions in Mn-substituted strontium titanate. *Solid State Commun.* **2000**, *114* (12), 617-622.
29. Serway, R. A.; Berlinger, W.; Müller, K. A.; Collins, R. W., Electron paramagnetic resonance of three manganese centers in reduced SrTiO₃. *Phys. Rev. B* **1977**, *16* (11), 4761-4768.
30. Badalyan, A. G.; Syrnikov, P. P.; Azzoni, C. B.; Galinetto, P.; Mozzati, M. C.; Rosa, J.; Trepakov, V. A.; Jastrabik, L., Manganese oxide nanoparticles in SrTiO₃:Mn. *J. Appl. Phys.* **2008**, *104* (3).
31. Lunsford, J. H., ESR of Adsorbed Oxygen Species. *Catal. Rev.Sci. Eng.* **2006**, *8* (1), 135-157.

32. Soria, J.; Sanz, J.; Sobrados, I.; Coronado, J. M.; Fresno, F.; Hernández-Alonso, M. D., Magnetic resonance study of the defects influence on the surface characteristics of nanosize anatase. *Catal. Today* **2007**, *129* (1-2), 240-246.
33. Šimánek, E., Müller, K. A., Covalency and Hyperfine Structure constant A of Iron group Impurities in Crystals. *J. Phys. Chem. Solids* **1970**, *31*, 1027-1040.
34. Kutty, T. R. N. D., L. G.; Murugaraj, P. , The Change in Oxidation State of Mn Ions in Semiconducting BaTiO₃ and SrTiO₃ around the Phase Transition Temperatures. *Mater. Res. Bull.* **1986**, *21*, 1093-1102.

CHAPTER 4

REVERSABLE MODULATION OF THE Cr³⁺ SPIN DYNAMICS IN COLLOIDAL SrTiO₃ NANOCRYSTALS

This chapter has been adapted from the published work:

Harrigan, W.L. and Kittilstved, K.R.; Reversible modulation of the Cr³⁺ spin dynamics in colloidal SrTiO₃ nanocrystals. *J. Phys. Chem. C*, **2018**, 122 (46), 26652-26657

4.1 Introduction

Control over either the individual or collective behavior of spins in semiconductor nanomaterials is a grand challenge for the field of quantum information processing.¹⁻³ One class of materials that shows promise for this technology are the diluted magnetic semiconductors (DMSs) where a fraction of the diamagnetic cations of the host lattice are substituted with paramagnetic dopant ions. The exchange interaction between spatially-confined charge carriers such as excitons or conduction band electrons (e_{cb}^-) and paramagnetic centers in nanoscale DMSs has been exploited to produce new magneto-optical phenomena such as excitonic magnetic polarons.⁴ However, traditional II-VI based DMS-QDs have isovalent dopants and do not possess appreciable n- or p-type carriers. The Fermi-level must therefore be modulated through incorporation of heterovalent dopants or reduction of the DMS-QD.

Previous work on colloidal semiconductor NCs demonstrated that electrons can be reversibly added to the conduction band by appropriate chemical reductants⁵ or "photodoping" with UV photons in the presence of a sacrificial reductant under anaerobic conditions.⁶⁻⁸ The introduction of chemically-stable e_{cb}^- into colloidal QDs by aliovalent doping has received increasing attention after the demonstrations of tunable localized

surface plasmon resonances (LSPR) in Al³⁺-doped ZnO (Al³⁺:ZnO) QDs and Sn⁴⁺:In₂O₃ NCs. Recently, the ability to modulate the carrier concentration of colloidal DMS-QDs has been shown to produce interesting effects in DMS-QDs including carrier-controlled magnetism⁹ and spin dynamics,¹⁰ and supercapacitance.¹¹

We recently reported the synthesis and characterization of Cr³⁺-doped SrTiO₃ colloidal NCs.¹² Through dopant-specific spectroscopic methods (including EPR, electronic absorption and emission), we confirmed that Cr³⁺ ions substitute at the Ti⁴⁺ site in the cuboidal NCs with ~10 nm edges. Herein, we present evidence that the spin dynamics of Cr³⁺ ions in colloidal SrTiO₃ NCs are extremely perturbed after photodoping, which does not produce e_{cb}^- , but localized Ti³⁺ defects. These “self-trapped electrons” at Ti³⁺ defects are confirmed by electronic absorption and continuous-wave (CW) electron paramagnetic resonance (EPR) spectroscopy and can be completely removed upon aerobic oxidation. The drastic change of the Cr³⁺ spin dynamics is evident even at room temperature by the disappearance of the Cr³⁺ EPR signal upon photodoping. We confirm the origin of this effect by performing EPR measurements as a function of temperature and power saturation rollover experiments between 4 K and 50 K. We invoke a cross-relaxation mechanism between localized Cr³⁺ and Ti³⁺ in photodoped SrTiO₃. These results demonstrate a new type of dopant-defect interaction that is (1) enhanced by spatial confinement of charge carriers in NCs, and (2) unique to metal oxides with conduction band minima that are comprised of empty d orbitals (d⁰ metal oxides such as TiO₂ and SrTiO₃).

4.2 Results and Discussion

Figure 4.1 shows the electronic absorption spectra of SrTiO₃ and nominally 0.1% Cr:SrTiO₃ colloidal nanocrystal anaerobic suspensions in hexanes as a function of UV irradiation time using a 75 W Xe lamp. The electronic absorption spectra of the as-prepared samples are dominated by the SrTiO₃ band gap transition above 3.2 eV. The Cr:SrTiO₃ NCs display a broad, weak transition that extends throughout the visible region and has been assigned in bulk Cr:SrTiO₃ as a metal-to-ligand charge transfer (MLCT) transition involving Cr³⁺ as the metal and the conduction band (empty Ti⁴⁺ 3d orbitals) as the ligand.¹³ With increasing photodoping time, the spectra change and the physical appearance of the NCs change from transparent or light yellow to dark blue. This change in color is accompanied by a new feature in the electronic absorption spectrum centered at ~1.4 eV (~900 nm). This feature has been observed previously in reduced titanium oxides¹⁴⁻¹⁶ and photodoped colloidal TiO₂ nanoparticles.¹⁷⁻²⁰ This new transition originates from the excitation of trapped electrons at Ti³⁺ centers to the SrTiO₃ conduction band (also known as a metal-to-metal charge transfer transition, MMCT). Similar to photodoped TiO₂, the near-IR transition does not shift in energy with increasing photodoping time, but does increase in optical density.

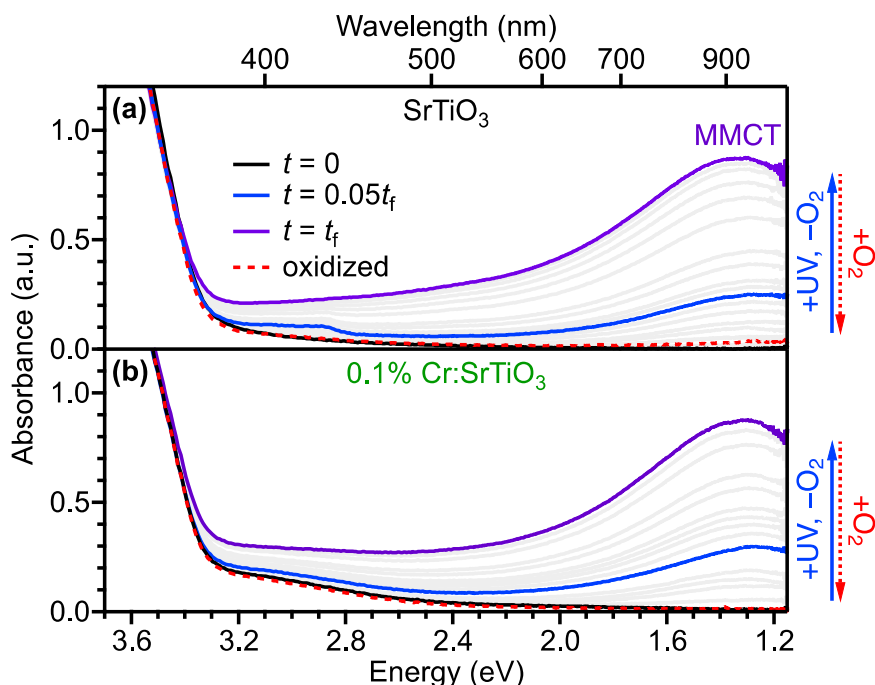


Figure 4.1. Electronic absorption spectra of air-free (a) SrTiO_3 and (b) 0.1% $\text{Cr}:\text{SrTiO}_3$ suspensions in hexane collected after different UV irradiation times. The spectra collected before irradiation (black line), and after irradiation at $0.05t_f$ (blue line) and t_f (purple line) are highlighted by colors. The spectra taken after reopening the cuvette to air is also shown (dashed red line). The t_f is arbitrarily defined as the time needed for the MMCT transition to reach an optical density equal to 0.87.

In pristine SrTiO_3 , a weak, broad feature appears at 430 nm after short photodoping times (see figure 4.1a), but disappears or becomes occluded by the intense MMCT transition that grows in at longer photodoping times. A similar visible absorption feature has been observed and assigned to transitions from the valence band to oxygen vacancies (V_O) in bulk SrTiO_3 .²¹⁻²² Notably, this feature is not observed for the $\text{Cr}:\text{SrTiO}_3$ NCs after similar photodoping times likely due to the stronger MLCT transition. We also looked in the mid-IR region, but photodoping does not appear to produce LSPRs such as those recently been reported for Nb-doped TiO_2 (see figure 4.7).²³ In addition, the band edge absorption does not shift with photodoping that further supports the self-trapping model for the electron and not as a delocalized e_{cb} , which should display a significant blue-shift

of the band edge according to the Moss-Burstein effect if electrons accumulate in the conduction band.²³ Figure 4.1 shows that photodoping ultimately creates localized Ti^{3+} defects in both NCs that are consistent with previous studies on TiO_2 nanoparticles.^{17-18,24} These electronic structure changes are also totally reversed upon reoxidizing the samples with air as shown in figure 4.1.

The Cr^{3+} -centered d-d transitions are too weak to be observed in the spectra shown in figure 4.1b. We therefore utilized EPR spectroscopy to confirm that Cr is trivalent and also monitor any changes in the Cr^{3+} signal upon introduction of Ti^{3+} defects in the Cr:SrTiO₃ NCs. EPR spectra were collected under the following conditions: (1) Cr:SrTiO₃ NCs before and after photodoping at room temperature, (2) Cr:SrTiO₃ and SrTiO₃ NCs after photodoping as a function of sample temperature and (3) microwave power at low temperatures.

The EPR spectra and color photographs of the colloidal Cr:SrTiO₃ NCs before and after photodoping at room temperature are shown in figure 4.2. As previously reported,^{12,25} Cr^{3+} in SrTiO₃ exhibits an isotropic EPR signal at $g = 1.978$ ($B_0 \sim 347$ mT in figure 4.2) which is consistent with substitutional doping of Cr^{3+} in the octahedral Ti^{4+} site of SrTiO₃. This signal corresponds to spin-allowed EPR transitions within the $^4\text{A}_2$ ground state of Cr^{3+} . The expected 4-line hyperfine pattern from $^{53}\text{Cr}^{3+}$ ions (relative abundance, rel. ab. = 9.5% with a nuclear spin of $I = 3/2$) is occluded by the inhomogeneously broadened central transition of the nuclear-spin free $^{52}\text{Cr}^{3+}$ isotopes (rel. ab. = $\sim 84\%$). After photodoping, however, the Cr^{3+} EPR signal disappears completely at room temperature and the solution appears blue due to the MMCT transition shown in figure 4.1 and in the color photograph in figure 4.2. Both the color of the sample and the Cr^{3+} EPR signal reverts quantitatively

to its original intensity upon reopening the sample to air. In addition, upon reoxidation a new feature at ~ 343 mT ($g \sim 2.009$) is clearly observed that we attribute to the reaction of Ti^{3+} with molecular O_2 to regenerate Ti^{4+} and form superoxide ions (O_2^-) at the NC surface. We recently observed this same defect-related signal in nominally undoped SrTiO_3 NCs that were prepared in the absence of hydrazine.¹²

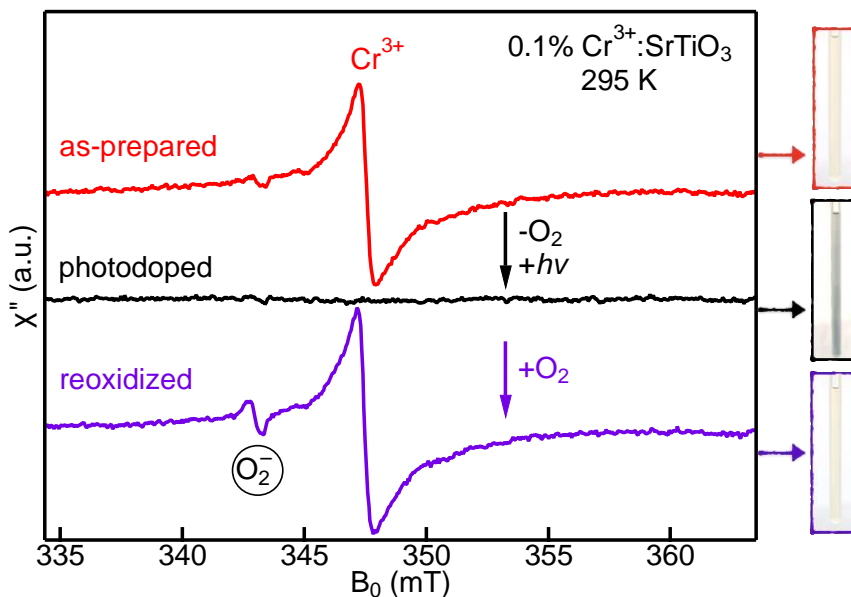


Figure 4.2. Room-temperature EPR spectra of 0.1% Cr:SrTiO₃ NCs in hexanes before (red) and after anaerobic photodoping (black), and after reoxidation (purple). Corresponding color photographs of representative Cr:SrTiO₃ samples in EPR tubes is included to the right of each EPR spectra.

The disappearance of the Cr^{3+} EPR signal in photodoped 0.1% Cr:SrTiO₃ could be explained by (1) the formation of a new EPR-silent Cr^{3+} -defect complex, (2) a change in the Cr^{3+} oxidation state, or (3) a possible interaction between Cr^{3+} and the paramagnetic Ti^{3+} defects, which typically requires low temperatures to observe by EPR due to fast spin-lattice relaxation dynamics. To evaluate which scenario was likely operative in the photodoped Cr:SrTiO₃ NCs, we measured EPR spectra at various temperatures down to 4.2 K. The EPR spectra of photodoped Cr:SrTiO₃ at various temperatures down to 77 K

and photodoped SrTiO₃ at 4.2 K are shown in figure 4.3. In the photodoped Cr:SrTiO₃ sample, we see the appearance of two broad signals that increase in intensity with decreasing temperature. The main feature is observed at ~347 mT ($g = 1.978$) and assigned to substitutional Cr³⁺ (see figure 4.2), while the second signal at ~355 mT ($g = \sim 1.95$) is asymmetric and is assigned to self-trapped electrons located at Ti³⁺ defects.²⁶ This assignment of the Ti³⁺ signal is confirmed by the 4.2 K spectrum of photodoped SrTiO₃ also shown in figure 4.3. Upon warming the photodoped Cr:SrTiO₃ to room temperature, we note the reappearance of a minor EPR signal from Cr³⁺ that we attribute to a small amount of air that was introduced through the low-pressure valve on the EPR tube during the thermal cycling.

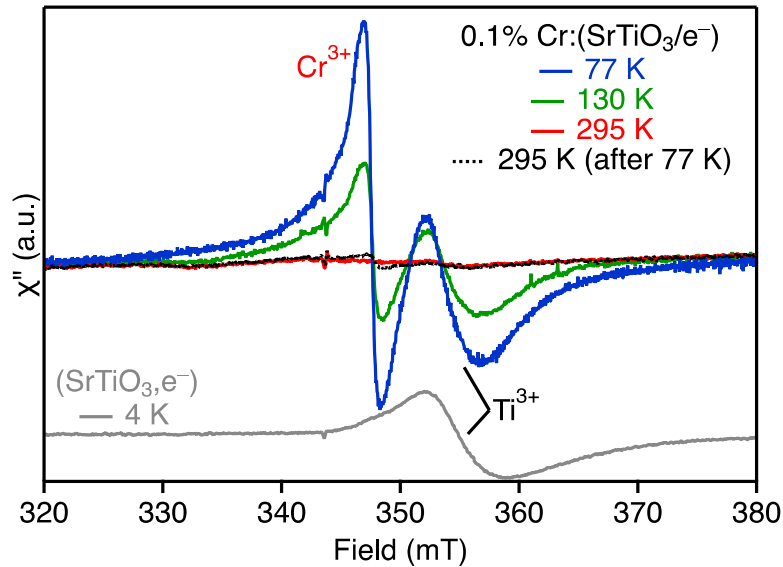


Figure 4.3. Variable-temperature EPR spectra collected on photodoped 0.1% Cr:SrTiO₃ NCs and 4.2 K spectrum of photodoped SrTiO₃ NCs. The spectra for photodoped Cr:SrTiO₃ were collected first at 295 K (red), and then decreased to 130 K (green) and 77 K (blue) followed by warming the sample again to 295 K (black dotted).

The behavior of the Cr³⁺ EPR signal in the photodoped Cr:SrTiO₃ NCs at various temperatures supports scenario 3 discussed above where the localized spins of Cr³⁺ are strongly interact with Ti³⁺ defects. We performed power saturation rollover studies with

various microwave powers on Cr:SrTiO₃ NCs before and after photodoping, and photodoped Cr:SrTiO₃ NCs to confirm the effect of Ti³⁺ on the Cr³⁺ spin dynamics. Representative CW-EPR spectra of these three samples at various microwave powers and 4.2 K are shown in figure 4.4. The EPR intensity for Cr³⁺ in the as-prepared Cr:SrTiO₃ sample and Ti³⁺ in the photodoped SrTiO₃ NCs is defined as ΔY , which is taken as the difference in the positive and negative χ'' values. For the overlapping Cr³⁺ and Ti³⁺ EPR signals in the photodoped Cr:SrTiO₃ NCs, we define the EPR intensity by the maximum positive χ'' and maximum negative χ'' values, respectively. The Cr³⁺ EPR signal in the Cr:SrTiO₃ NCs before photodoping increases to a maximum peak intensity at ~8 mW before decreasing and broadening at higher powers. In contrast, the EPR signal of Ti³⁺ in photodoped SrTiO₃ NCs steadily increases without saturating even >200 mW. The EPR signals for both Cr³⁺ and Ti³⁺ in the photodoped Cr:SrTiO₃ NCs display behavior similar to the Ti³⁺ defects in photodoped SrTiO₃ NCs; continuously increasing without saturating with increasing microwave power. These spectra confirm that the spin dynamics of the Cr³⁺ dopants are efficiently modulated by the presence of Ti³⁺ defects.

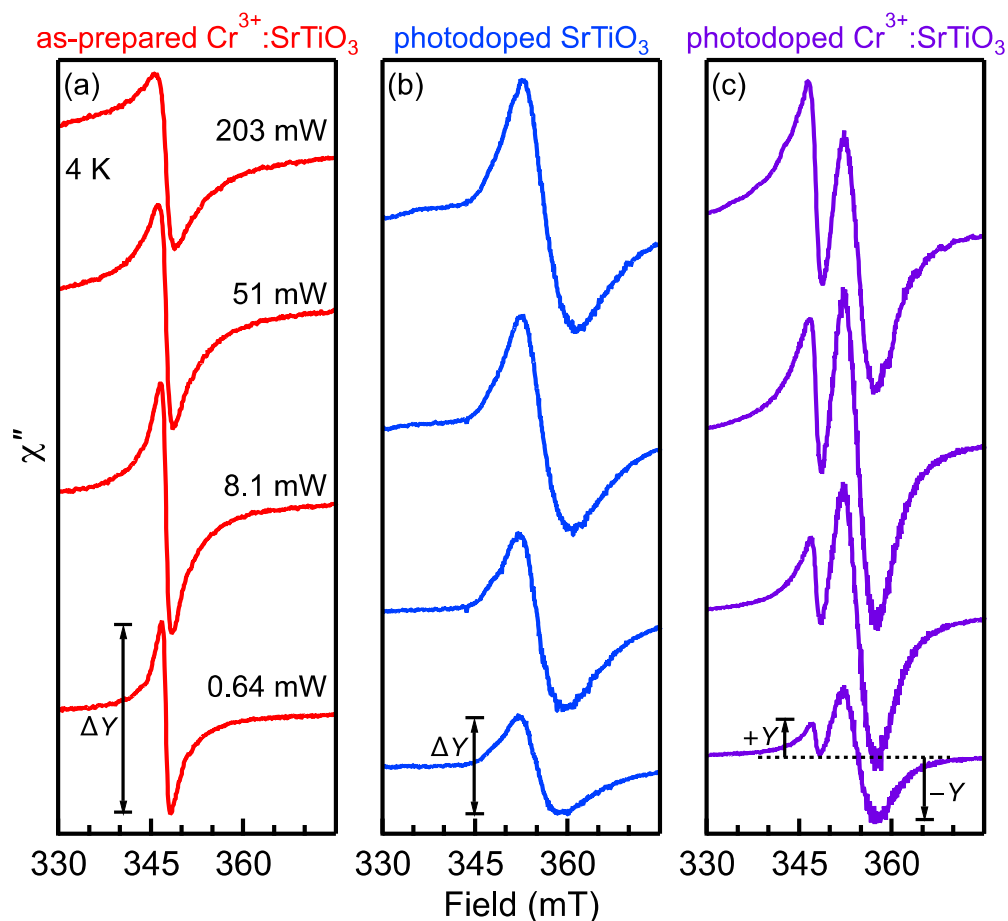


Figure 4.4. Representative CW-EPR spectra of (a) as-prepared Cr:SrTiO₃, (b) photodoped SrTiO₃, and (c) photodoped Cr:SrTiO₃ NCs at 4.2 K (frozen suspension) and selected microwave powers. Definitions for the signal intensities for the different EPR-active species in the different sets of spectra are included graphically in the panels.

The EPR signal intensities (ΔY or $|Y|$) at 4.2 K of the Cr³⁺ or Ti³⁺ ions in the different samples in figure 4.4 are plotted as a function of microwave power (h_1 , converted to Gauss units) in figure 4.5. For Cr:SrTiO₃ NCs before photodoping, the Cr³⁺ intensity exhibits typical saturation and rollover behavior; increasing steadily with increasing power until saturating at $h_1 \sim 0.06$ G and then decreasing with increasing h_1 . The temperature dependence of this saturation behavior for the Cr³⁺ signal in Cr:SrTiO₃ NCs before photodoping shows a steady increase in the saturation power with increasing temperature (see figure 4.8). However, the peak intensities of Ti³⁺ in photodoped SrTiO₃ and Ti³⁺ and

Cr³⁺ in photodoped Cr:SrTiO₃ both increase with increasing microwave power, but do not saturate even at 4.2 K.

The data in figure 4.5 were used to estimate the magnitude of the total spin dynamics according to eq 4.1.

$$\Delta Y \text{ or } |Y| = c \cdot h_1 \left(1 + \frac{(h_1)^2}{P_2} \right)^{-\varepsilon} \quad (4.1a)$$

$$P_2 = (\gamma_e^2 T_1 \cdot T_2)^{-1} \quad (4.1b)$$

where c is a scalar and ε is a measure of line homogeneity. P_2 is proportional to the product of the spin-lattice and spin-spin relaxation rates ($1/T_1$ and $1/T_2$, respectively), and γ_e is the electron gyromagnetic ratio (see eq 4.1b).

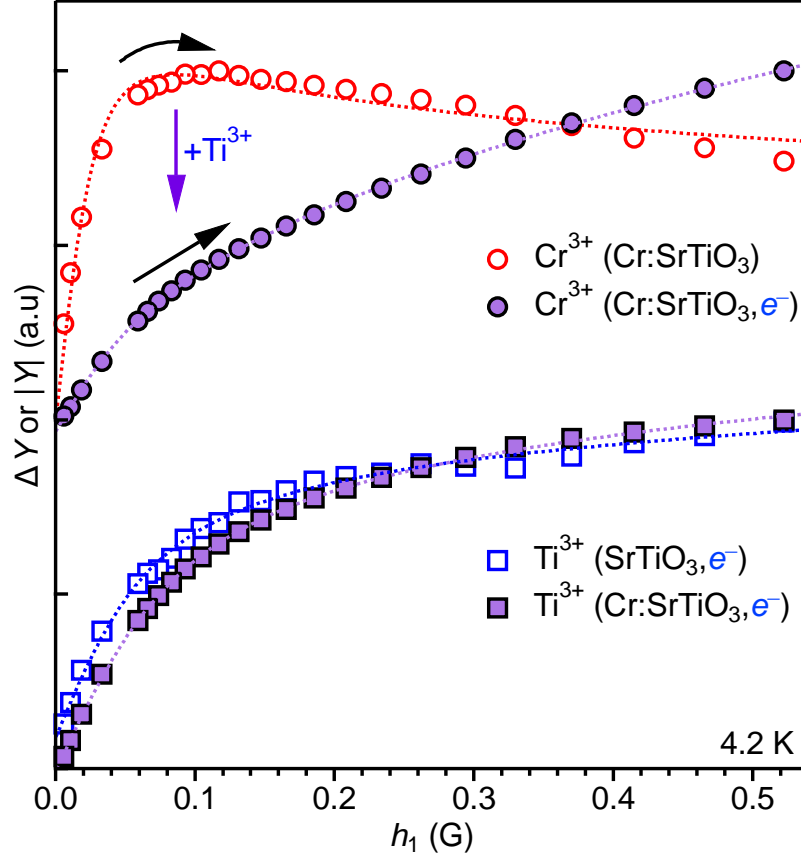


Figure 4.5. Normalized CW-EPR intensities (ΔY or $|Y|$) as a function of incident microwave power (h_1) at 4.2 K for Cr^{3+} (red) and Ti^{3+} (blue) EPR signals in the following samples: Cr^{3+} in as-prepared $\text{Cr}:\text{SrTiO}_3$ (empty circles), Ti^{3+} in photodoped SrTiO_3 (empty squares), and the Cr^{3+} and Ti^{3+} signals in photodoped $\text{Cr}:\text{SrTiO}_3$ (filled circles and squares, respectively). The dashed curves through the data points are best fits to eq 1a (shaded regions are error bars on the fits).

The values of P_2 obtained from the experimental fits to the power-dependence of the EPR intensities are plotted as a function of temperature in figure 4.6. The relaxation dynamics of the Cr^{3+} spins increase by at least a factor of two below 50 K when Ti^{3+} defects are also present in the NC. In addition, the Ti^{3+} relaxation dynamics show an even larger increase in the photodoped SrTiO_3 NCs when Cr^{3+} is present. This latter result could be caused by the relative distributions of Cr^{3+} dopants and Ti^{3+} defects in the ensemble of SrTiO_3 NCs. Furthermore, the density, speciation, and proximity of Ti^{3+} defects to surfaces, other Ti^{3+} centers and Cr^{3+} dopants is largely unknown.

While there is variability in the temperature dependence of the spin relaxation, the trend is consistent with regards to temperature and relaxation rates: (1) the relaxation rate is slowest for Cr^{3+} in SrTiO_3 NCs before photodoping and increases upon photodoping; and (2) the Ti^{3+} relaxation rate increases with the presence of Cr^{3+} .

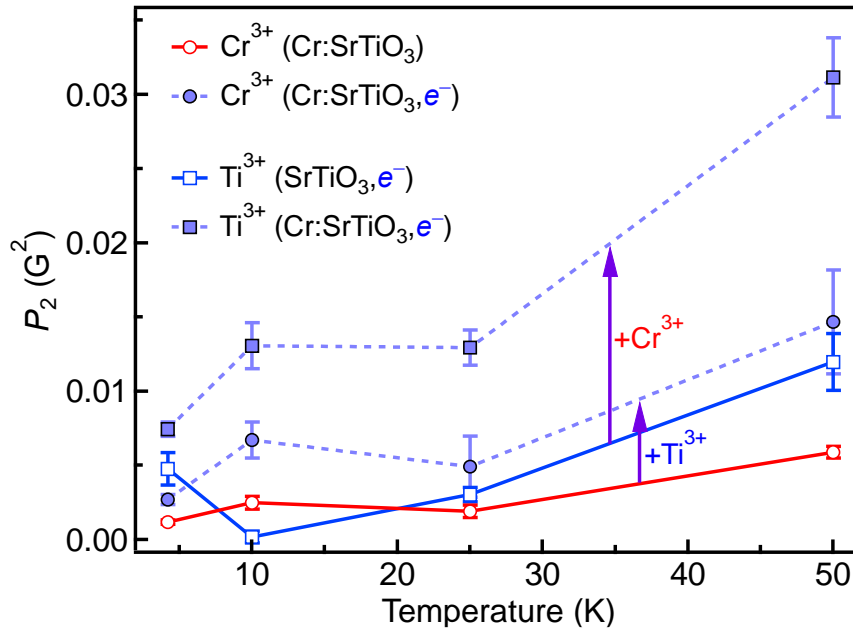


Figure 4.6. Temperature dependence of P_2 , for Cr^{3+} (circles) and Ti^{3+} (squares) in before (open) and after (filled) photodoping either $\text{Cr}:\text{SrTiO}_3$ or SrTiO_3 NCs. Both signals have an increase in the spin dynamics overall relaxation rates increase when Ti^{3+} is present in the lattice. Lines are guides to the eye.

Systematic studies of spin relaxation rates of isovalent Cr^{3+} and Ti^{3+} in Al_2O_3 date back to the early 1960s.²⁷⁻²⁸ Prokhorov first demonstrated that the spin-lattice relaxation times of $(\text{Al}_{1-x}\text{M}_x)_2\text{O}_3$ differ by many orders of magnitude at cryogenic temperatures for $\text{M} = \text{Cr}^{3+}$ or Ti^{3+} . Spin-lattice relaxation times at 4.2 K for $\text{Cr}:\text{Al}_2\text{O}_3$ is ~ 50 ms, whereas for $\text{Ti}:\text{Al}_2\text{O}_3$ $T_1 = \sim 0.1$ ms.²⁷ These reported times are also sensitive to temperature and dopant concentration (self or resonant cross-relaxation).²⁸ Here, the difference in P_2 between Cr^{3+}

in Cr:SrTiO₃ NCs and Ti³⁺ in photodoped SrTiO₃ NCs is much smaller than in Al₂O₃. This deviation is possibly due to the polaronic nature²⁹⁻³⁰ of the self-trapped electron of Ti³⁺ in SrTiO₃ versus the localized 3d¹ Ti³⁺ ion in Al₂O₃. Future work to address the effect of the Cr³⁺:Ti³⁺ ratio on the spin relaxation dynamics are currently underway.

In the absence of pulsed EPR measurements to directly determine relaxation rates, we estimated T_2 by analysis of the EPR linewidth. The EPR spectra of Cr³⁺ in Cr:SrTiO₃ before photodoping at 4.2 K and microwave powers well below saturation were fit to the first-derivative of a pseudo-Voigt line profile (linear combination of a Lorentzian and Gaussian function). For Cr³⁺ in Cr:SrTiO₃ before photodoping, the Lorentzian linewidth is found to be $\Gamma_L = 6.4$ G (see table 4.1), which equates to $T_2 \approx 18$ ns by the relation,³¹ $T_2 = 2/(\gamma_e \Gamma_L)$. This value of T_2 at 4.2 K is similar to reported values for Cr³⁺ in bulk Al₂O₃.³² Using eq 4.1b and the experimental P_2 value, $T_1 \approx 150$ μ s. A strong concentration-dependence results in a range of T_1 values between 170 μ s and 110 ms for Cr³⁺ in bulk Al₂O₃ at 4.2 K.³²⁻³³ A similar study of the concentration dependence of T_1 has not been performed for Cr³⁺ in bulk SrTiO₃, but for a Cr concentration of 0.05% the value at 4.2 K is $T_1 \approx 1$ -5 ms.³⁴ The faster spin-lattice relaxation of the Cr³⁺ dopants in SrTiO₃ NCs before photodoping could arise from heterogeneity in dopant location and proximity to NC surfaces.³⁵

Unfortunately, accurate deconvolution of the linewidths for the photodoped Cr:SrTiO₃ samples were complicated due to the overlapping signals of Cr³⁺ and Ti³⁺. If we assume that the T_2 value of Cr³⁺ is unchanged after photodoping, then we estimate an accelerated $T_1 \approx 70$ μ s for the Cr³⁺ dopants in photodoped Cr:SrTiO₃ NCs at 4.2 K. Prior

studies of cross-relaxation in $\text{Cr}^{3+}, \text{Ti}^{3+}$ codoped Al_2O_3 have similar reductions in T_1 -values of the Cr^{3+} dopants at low temperatures when Ti^{3+} is present.²⁸

Previously, some of us demonstrated the introduction of Ti^{3+} defects could also be achieved in bulk Cr^{3+} -doped SrTiO_3 (and related Sr_2TiO_4) powders using NaBH_4 .³⁶⁻³⁷ After this chemical reduction, the Cr^{3+} concentration increases by an order of magnitude according to quantitative EPR measurements due to the *reduction* of EPR-silent Cr species to Cr^{3+} prior to formation of Ti^{3+} defects. No such increase in the Cr^{3+} EPR signal is observed at the start of photodoping (see figure 4.13). In addition, the EPR linewidth of Cr^{3+} significantly broadens after lattice Ti^{3+} defects are formed. We tentatively attributed this broadening to a magnetic interaction between Cr^{3+} and Ti^{3+} , however, we were limited due to inhomogeneous distributions of Ti^{3+} and V_{O} in the bulk material. This clear interaction in the current study suggests that similar broadening through cross-relaxation is also active in the reduced $\text{Cr}:\text{SrTiO}_3$, but the Ti^{3+} defects are limited to the (sub-)surface layers of the bulk powders.

4.3 Conclusions

We report the efficient and reversible modulation of the spin relaxation of Cr^{3+} dopants in colloidal SrTiO_3 NCs. This spin phenomenon results in the disappearance of the Cr^{3+} EPR signal at room temperature and can reappear either by (1) reoxidizing the Ti^{3+} defects in the NCs with air, or (2) lowering the sample temperature. The latter scenario also confirms the presence of paramagnetic Ti^{3+} defects. Power saturation rollover experiments at 4.2 K confirms the origin of the accelerated spin dynamics of Cr^{3+} in photodoped $\text{Cr}:\text{SrTiO}_3$ to an efficient, near-resonant, cross-relaxation involving Ti^{3+} defects.

While similar cross-relaxation processes are evident between the Cr^{3+} and Ti^{3+} defects in these SrTiO_3 NCs and similar bulk lattices, these changes are quantitatively reversible by using only UV photons and mild oxidants. The facile generation of many Ti^{3+} defects within a single SrTiO_3 NC via photodoping ensures that every Cr^{3+} dopant is in spatial proximity for near-resonant cross-relaxation processes to dominate the Cr^{3+} spin dynamics even at room temperature. This discovery introduces an interesting spin-based phenomenon in colloidal semiconductor NCs. We are currently investigating the generality of cross-relaxation to other EPR-active isovalent and heterovalent dopants in SrTiO_3 .

4.4 Supplementary Information

4.4.1 Materials. Strontium hydroxide (99%, Alfa Aesar), titanium(IV) bis(ammonium lactate)dihydroxide (TiALH 50% wt in water, Alfa Aesar), tetramethylammonium hydroxide (NMe₄OH, Acros Organics), chromium(III) nitrate (Crystalline Certified, Fisher Chemical), hydrazine hydrate (N₂H₄·H₂O, 99% Acros Organics), oleic acid (90% Fisher Chemical), hexanes (optima, Fisher Chemical), ethanol (200 proof, PHARMCO-AAPER) and reverse-osmosis deionized (RO/DI) water.

4.4.2 Preparation of anaerobic undoped and chromium doped SrTiO_3 colloidal nanocrystals. Undoped SrTiO_3 and 0.1% $\text{Cr}^{3+}:\text{SrTiO}_3$ colloidal nanocrystals (NCs) were prepared using previously reported methods (with hydrazine hydrate).¹² To prepare anaerobically suspended colloidal NCs for photodoping experiments, a suspension of NCs were precipitated with ethanol, centrifuged, and the pellet was transferred into a N₂-filled glovebox. Two short pump/purge cycles with N₂ were done to remove any oxygen and moisture from the sample. Once inside the glovebox, the samples were suspended in 4 mL

of degassed hexanes and 0.4 mL of ethanol. The resulting suspension of NCs was transferred to either an air-free cuvette, an air-free EPR tube, or a KBr demountable cell with a 0.05 mm pathlength for subsequent photodoping measurements. Reoxidation of the photodoped samples was done by exposing the solution to air.

4.4.3 Physical Methods. Photodoping experiments were performed by irradiating the sample (in a cuvette, EPR tube, or demountable KBr cell) with light from a 75-W or 1000-W Xe arc lamp for various times. Electronic absorption measurements were collected on a Cary 50 Bio. EPR measurements were collected on a Bruker Elexsys E-500 fitted with an ER 4116 dual-mode X-band cavity (in perpendicular mode). Mid-infrared absorption spectra were collected on a Varian 670 Fourier transform spectrometer using a KBr beam splitter and DLaTGS detector.

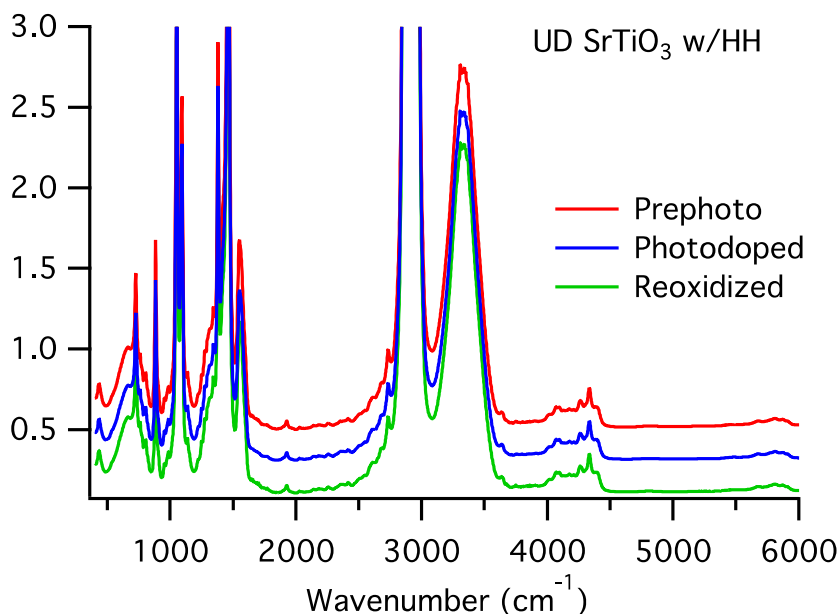


Figure 4.7. Mid IR spectra of UD STO-A before and after photo-irradiation. There is no change in the absorption spectra after irradiating the sample in a KBr demountable cell with a 0.05 mm path length using a 1000 W lamp for 1 hr.

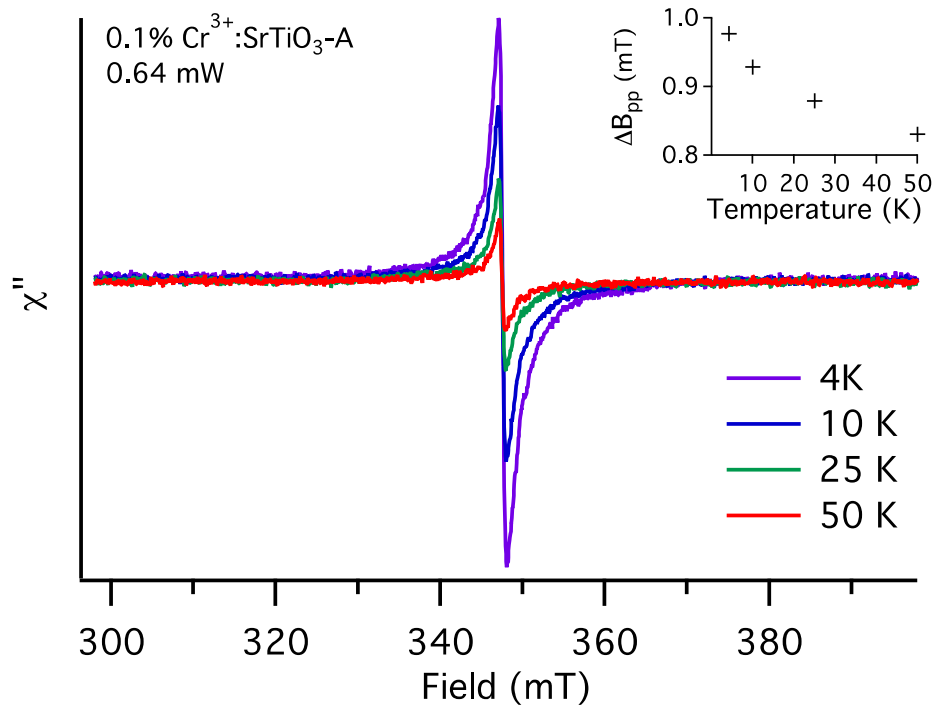


Figure 4.8. EPR spectra of AP-nominal 0.1% Cr: SrTiO₃ as a function of temperature. The inset shows the temperature dependence of the total peak to peak line width.

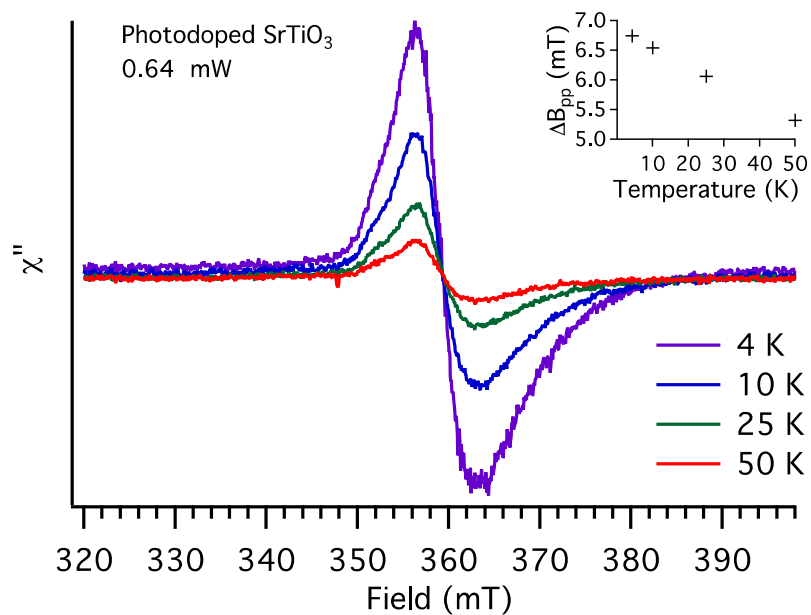


Figure 4.9. EPR spectra of photodoped undoped SrTiO₃ showing the Ti³⁺ signal as a function of temperature. The inset shows the temperature dependence of the total peak to peak line width.

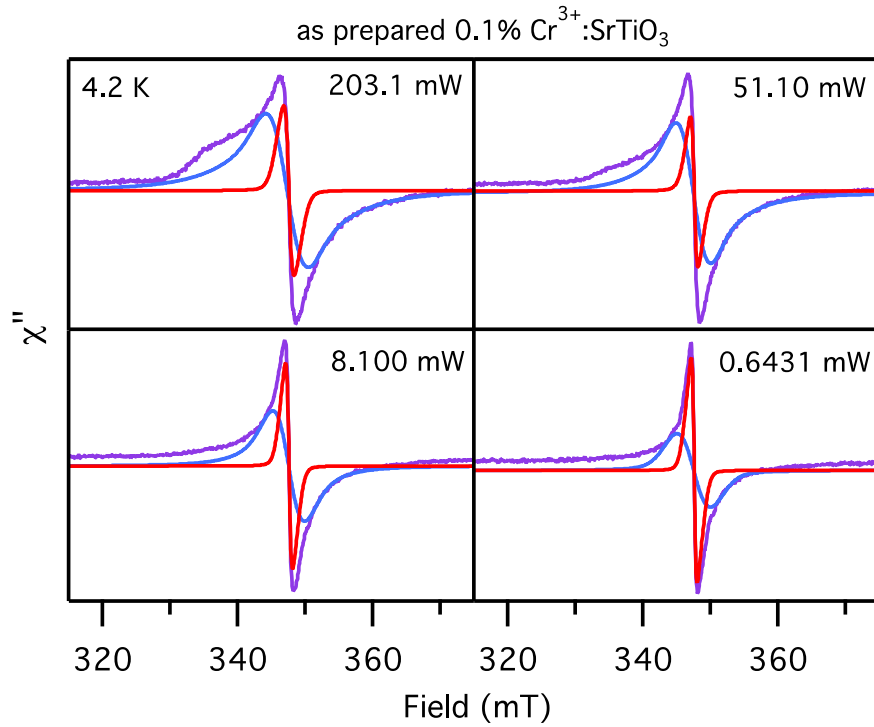


Figure 4.10. EPR spectra of 0.1% Cr:SrTiO₃ NCs collected at 4.2 K before photodoping as a function of microwave power. The red and blue lines are the partitioned signals obtained from fitting the spectra to a double pseudo-Voigt. The Lorentzian widths obtained from red lines were used to calculate the actual T_2 .

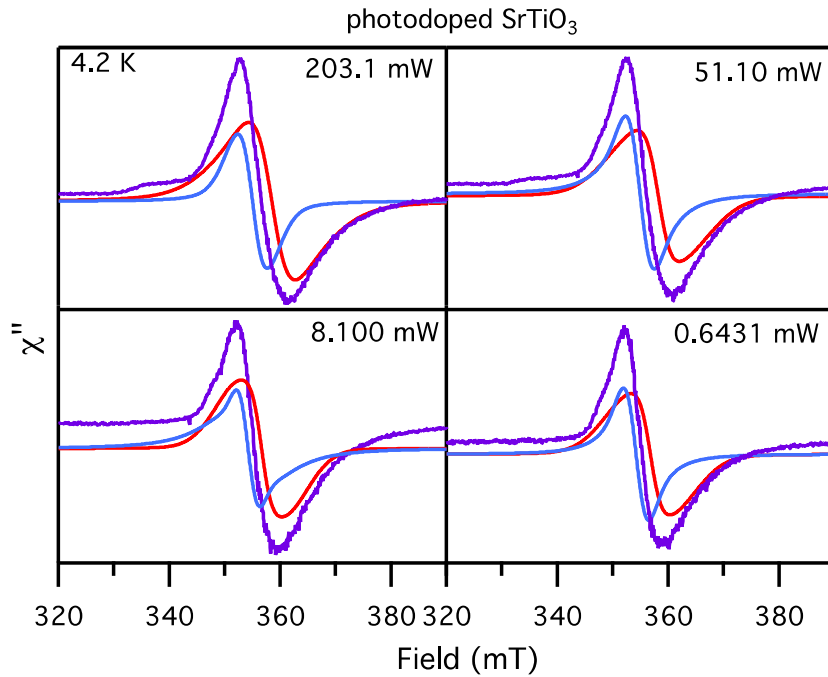


Figure 4.11. EPR spectra collected at 4.2 K of photodoped SrTiO₃ as a function of microwave power. The red and blue lines are the partitioned signals obtained from fitting

the spectra to two pseudo-Voigt profiles to account for the g -anisotropy of the distorted Ti^{3+} defect. The Lorentzian widths obtained from red lines were used to calculate the actual T_2 .

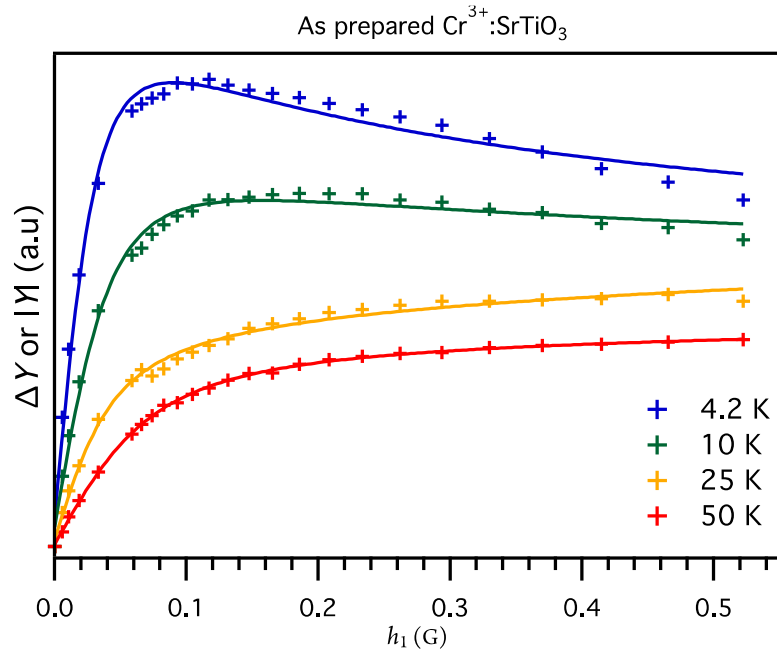


Figure 4.12. EPR signal intensity of Cr^{3+} before photodoping as a function of microwave power at different temperatures. The microwave power in which the signal saturates increases with temperature.

Table 4.1: Temperature dependence of the spin-spin relaxation time (T_2) using the deconvoluted Lorentzian width from fitting each CW EPR spectra to a first derivative pseudo-Voigt line profile.

Temp. (K)	Γ_L, Cr^{3+} (G)	T_2, Cr^{3+} (ns)	Γ_L, Ti^{3+} (G)	T_2, Ti^{3+} (ns)
4.2	6.36 ± 0.13	17.8 ± 0.4	60.6 ± 5.2	1.87 ± 0.16
10	6.29 ± 0.16	18.0 ± 0.5	53.4 ± 3.9	2.13 ± 0.16
25	5.42 ± 0.001	21.0 ± 0.004	34.9 ± 1.6	3.26 ± 0.15
50	5.14 ± 0.17	22.1 ± 0.7	37.2 ± 1.9	3.05 ± 0.16

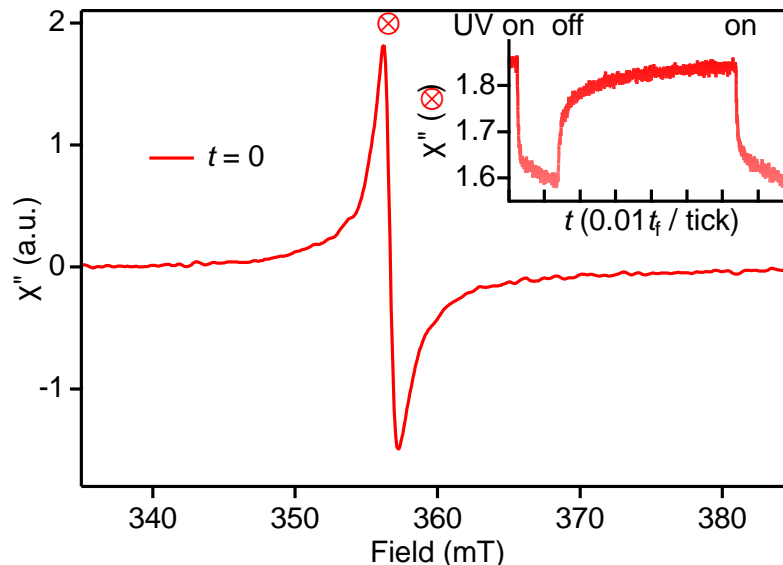


Figure 4.13. Room temperature EPR spectra of 0.1% Cr³⁺:SrTiO₃ nanocrystals in hexanes before (red) and after (blue) UV irradiation. Inset: reversible EPR intensity of the Cr³⁺ maximum at 356 mT under aerobic conditions in the EPR spectrometer. Note the initial *decrease* of Cr³⁺ EPR intensity begins immediately upon light irradiation. This experiment is also done for short irradiation times, which does not result in total disappearance of the Cr³⁺ EPR signal (the y-axes of the main spectrum and inset are the equivalent). This result is consistent with initial formation of Ti³⁺ and not with reduction of EPR-silent and higher-valent Cr ions such as Cr⁴⁺ or Cr⁶⁺.

4.5 References

1. Berezovsky, J.; Mikkelsen, M. H.; Stoltz, N. G.; Coldren, L. A.; Awschalom, D. D., Picosecond coherent optical manipulation of a single electron spin in a quantum dot. *Science* **2008**, *320*, 349-352.
2. Imamoglu, A.; Awschalom, D. D.; Burkard, G.; DiVincenzo, D. P.; Loss, D.; Sherwin, M.; Small, A., Quantum Information Processing Using Quantum Dot Spins and Cavity QED. *Phys. Rev. Lett.* **1999**, *83*, 4204-4207.
3. Clark, S. M.; Fu, K. M.; Ladd, T. D.; Yamamoto, Y., Quantum computers based on electron spins controlled by ultrafast off-resonant single optical pulses. *Phys. Rev. Lett.* **2007**, *99*, 040501.
4. Beaulac, R.; Schneider, L.; Archer, P. I.; Bacher, G.; Gamelin, D. R., Light-induced spontaneous magnetization in doped colloidal quantum dots. *Science* **2009**, *325*, 973-976.

5. Shim, M.; Guyot-Sionnest, P., n-type colloidal semiconductor nanocrystals. *Nature* **2000**, *407*, 981-983.
6. Liu, W. K.; Whitaker, K. M.; Kittilstved, K. R.; Gamelin, D. R., Stable photogenerated carriers in magnetic semiconductor nanocrystals. *J. Am. Chem. Soc.* **2006**, *128*, 3910-3911.
7. Schimpf, A. M.; Gunthardt, C. E.; Rinehart, J. D.; Mayer, J. M.; Gamelin, D. R., Controlling Carrier Densities in Photochemically Reduced Colloidal ZnO Nanocrystals: Size Dependence and Role of the Hole Quencher. *J. Am. Chem. Soc.* **2013**, *135*, 16569-16577.
8. Schimpf, A. M.; Thakkar, N.; Gunthardt, C. E.; Masiello, D. J.; Gamelin, D. R., Charge-Tunable Quantum Plasmons in Colloidal Semiconductor Nanocrystals. *ACS Nano* **2014**, *8*, 1065-1072.
9. Ochsenein, S. T.; Feng, Y.; Whitaker, K. M.; Badaeva, E.; Liu, W. K.; Li, X. S.; Gamelin, D. R., Charge-controlled magnetism in colloidal doped semiconductor nanocrystals. *Nat. Nanotechnol.* **2009**, *4*, 681-687.
10. Schimpf, A. M.; Rinehart, J. D.; Ochsenein, S. T.; Gamelin, D. R., Charge-State Control of Mn²⁺ Spin Relaxation Dynamics in Colloidal n-Type Zn_{1-x}Mn_xO Nanocrystals. *J. Phys. Chem. Lett.* **2015**, *6*, 1748-1753.
11. Brozek, C. K.; Zhou, D. M.; Liu, H. B.; Li, X. S.; Kittilstved, K. R.; Gamelin, D. R., Soluble Supercapacitors: Large and Reversible Charge Storage in Colloidal Iron-Doped ZnO Nanocrystals. *Nano Lett.* **2018**, *18*, 3297-3302.
12. Harrigan, W. L.; Michaud, S. E.; Lehuta, K. A.; Kittilstved, K. R., Tunable Electronic Structure and Surface Defects in Chromium-Doped Colloidal SrTiO_{3-δ} Nanocrystals. *Chem. Mater.* **2016**, *28*, 430-433.
13. Blasse, G.; de Korte, P. H. M.; Mackor, A., The colouration of titanates by transition-metal ions in view of solar energy applications. *J. Inorg. Nucl. Chem.* **1981**, *43*, 1499-1503.
14. Zuo, F.; Wang, L.; Wu, T.; Zhang, Z.; Borchardt, D.; Feng, P., Self-doped Ti³⁺ enhanced photocatalyst for hydrogen production under visible light. *J. Am. Chem. Soc.* **2010**, *132*, 11856-11857.
15. Tan, H.; Zhao, Z.; Zhu, W. B.; Coker, E. N.; Li, B.; Zheng, M.; Yu, W.; Fan, H.; Sun, Z., Oxygen Vacancy Enhanced Photocatalytic Activity of Perovskite SrTiO₃. *ACS Appl. Mater. Interfaces* **2014**, *6*, 19184-19190.

16. Khomenko, V. M.; Langer, K.; Rager, H.; Fett, A., Electronic absorption by Ti^{3+} ions and electron delocalization in synthetic blue rutile. *Phys. Chem. Minerals* **1998**, *25*, 338-346.
17. Schrauben, J. N.; Hayoun, R.; Valdez, C. N.; Braten, M.; Fridley, L.; Mayer, J. M., Titanium and zinc oxide nanoparticles are proton-coupled electron transfer agents. *Science* **2012**, *336*, 1298-1301.
18. Kölle, U.; Moser, J.; Grätzel, M., Dynamics of interfacial charge-transfer reactions in semiconductor dispersions. Reduction of cobaltoceniumdicarboxylate in colloidal titania. *Inorg. Chem.* **1985**, *24*, 2253-2258.
19. Bahnemann, D.; Henglein, A.; Lilie, J.; Spanhel, L., Flash photolysis observation of the absorption spectra of trapped positive holes and electrons in colloidal titanium dioxide. *J. Phys. Chem.* **1984**, *88*, 709-711.
20. Henglein, A., Colloidal TiO_2 Catalyzed Photo- and Radiation Chemical Processes in Aqueous Solution. *Ber. Bunsenges. Phys. Chem.* **1982**, *86*, 241-246.
21. Mitra, C.; Lin, C.; Robertson, J.; Demkov, A. A., Electronic structure of oxygen vacancies in $SrTiO_3$ and $LaAlO_3$. *Phys. Rev. B* **2012**, *86*, 155105.
22. Rice, W. D.; Ambwani, P.; Bombeck, M.; Thompson, J. D.; Haugstad, G.; Leighton, C.; Crooker, S. A., Persistent optically induced magnetism in oxygen-deficient strontium titanate. *Nat. Mater.* **2014**, *13*, 481-487.
23. De Trizio, L.; Buonsanti, R.; Schimpf, A. M.; Llordes, A.; Gamelin, D. R.; Simonutti, R.; Milliron, D. J., Nb-Doped Colloidal TiO_2 Nanocrystals with Tunable Infrared Absorption. *Chem. Mater.* **2013**, *25*, 3383-3390.
24. Peper, J. L.; Vinyard, D. J.; Brudvig, G. W.; Mayer, J. M., Slow Equilibration between Spectroscopically Distinct Trap States in Reduced TiO_2 Nanoparticles. *J. Am. Chem. Soc.* **2017**, *139*, 2868-2871.
25. Müller, K. A., hyperfine and g-values for Cr^{3+} in $SrTiO_3$. In *Proceedings of the First International Conference I, Paramagnetic Resonance*, Low, W., Ed. Academic Press: New York, 1963; p 17.
26. Howe, R. F.; Grätzel, M., EPR observation of trapped electrons in colloidal titanium dioxide. *J. Phys. Chem.* **1985**, *89*, 4495-4499.
27. Manenkov, A. A.; Prokhorov, A. M., Spin-lattice relaxation and cross-relaxation interactions in chromium corundum. *Sov. Phys. JETP* **1962**, *15*, 54-59.
28. Nisida, Y., Spin-Lattice Relaxation of Cr^{3+} in Coexistence with Ti^{3+} in Al_2O_3 . *J. Phys. Soc. Japan* **1965**, *20*, 1390-1399.

29. Janotti, A.; Franchini, C.; Varley, J. B.; Kresse, G.; Van de Walle, C. G., Dual behavior of excess electrons in rutile TiO₂. *Phys. Status Solidi RRL* **2013**, *7*, 199-203.
30. Hao, X.; Wang, Z.; Schmid, M.; Diebold, U.; Franchini, C., Coexistence of trapped and free excess electrons in SrTiO₃. *Phys. Rev. B* **2015**, *91*, 085204.
31. Whitaker, K. M.; Ochsenbein, S. T.; Smith, A. L.; Echodu, D. C.; Robinson, B. H.; Gamelin, D. R., Hyperfine Coupling in Colloidal n-Type ZnO Quantum Dots: Effects on Electron Spin Relaxation. *J. Phys. Chem. C* **2010**, *114*, 14467-14472.
32. Manenkov, A. A.; Prokhorov, A. M., Spin-lattice relaxation in chromium corundum. *Sov. Phys. JETP* **1960**, *11*, 527-530.
33. Mims, W. B.; McGee, J. D., Cross Relaxation in Ruby. *Phys. Rev.* **1960**, *119*, 1233-1237.
34. Azamat, D. V.; Dejneka, A.; Lancok, J.; Trepakov, V. A.; Jastrabik, L.; Badalyan, A. G., Pulse-electron paramagnetic resonance of Cr³⁺ centers in SrTiO₃. *J. Appl. Phys.* **2013**, *113*, 174106.
35. Schimpf, A. M.; Ochsenbein, S. T.; Gamelin, D. R., Surface Contributions to Mn²⁺ Spin Dynamics in Colloidal Doped Quantum Dots. *J. Phys. Chem. Lett.* **2015**, *6*, 457-463.
36. Lehuta, K. A.; Kittilstved, K. R., Reversible control of the chromium valence in chemically reduced Cr-doped SrTiO₃ bulk powders. *Dalton. Trans.* **2016**, *45*, 10034-10041.
37. Lehuta, K. A.; Haldar, A.; Zhou, D.; Kittilstved, K. R., Spectroscopic Study of the Reversible Chemical Reduction and Reoxidation of Substitutional Cr Ions in Sr₂TiO₄. *Inorg. Chem.* **2017**, *56*, 9177-9184.

CHAPTER 5

CONCLUSIONS AND FUTURE DIRECTIONS

Doped perovskites such as SrTiO₃ have gained increased attention due to the vast potential in a wide variety of applications based on dopant induced properties. The main focus of this work was to investigate dopant speciation and defect formation in colloidal NCs compared to bulk analogs. Another focus of this work was on understanding the interactions between photoinduced electrons and the interactions with intrinsic and extrinsic defects in colloidal NCs.

Using two modified hydrothermal methods, with and without hydrazine corresponding to methods A and B respectively, the incorporation of Cr³⁺ into colloidal SrTiO₃ was studied. Highly crystalline phase pure doped colloidal SrTiO₃ was synthesized via these methods. Cr³⁺ was confirmed to be internally doped for Ti⁴⁺ through the use of electronic absorption spectroscopy, EPR spectroscopy, and low-temperature emission. For method A, the ⁴A₂→⁴T₂ and ⁴A₂→⁴T₁(F) ligand field transitions of Cr³⁺ in an octahedral ligand field were observed. In contrast, the ligand field transitions were not observed for method B, but rather a broad featureless absorption tailing into the visible region was observed. Regardless of the method, both showed internal doping of Cr³⁺ in EPR from the calculated g and hyperfine A values (g=1.978 and A=16.2 x 10⁻⁴ cm⁻¹). Different defects were observed depending on the method used and if Cr³⁺ was used. The use of hydrazine (HH) yielded specific surface defects (O₂⁻ when HH omitted) and when Cr was used (O⁻) identified through EPR.

Mn-doped colloidal SrTiO₃ NCs were also synthesized and investigated. Mn⁴⁺, isoelectronic with Cr³⁺ should have no need for charge compensation and therefore should

induce or omit certain defects. In both methods, Mn dopes into colloidal SrTiO₃ NCs with mixed valency, exclusively at the Ti⁴⁺ site. This was confirmed through intensive EPR spectroscopic analyses, with corresponding the calculated g and hyperfine values to literature reports. There was no spectroscopic evidence of Mn²⁺ substituting for Sr²⁺ in the colloidal NCs. The variation in the synthesized Mn-SrTiO₃ colloids, evidenced by EPR concluded that the Mn dopants are very easily photosensitized. Compared to high-temperature reductions with long annealing times, this is a facile way to reversibly change the oxidation state of Mn. The product of this photo-induced reduction has been tentatively assigned to a Mn²⁺-v_o complex.

To gain a better understanding of how photo-induced electrons interact with dopants and defects, a photodoping technique was used. In Cr-doped SrTiO₃, Cr only exists as Cr³⁺ when doped into SrTiO₃, as we do not see an increase in EPR intensity at the early stages of the photodoping process. A reduction of Ti⁴⁺ to Ti³⁺ was observed under anaerobic conditions when a hole quencher, ethanol was used. This was verified through the deep blue color of the suspensions upon photoirradiation, a non-shifting near-infrared absorption peak centered around 900 nm, and the Ti³⁺ EPR signal that only appeared below 105 K. The generation of Ti³⁺ caused a disappearance of the Cr³⁺ EPR signal at room temperature. Upon cooling the sample down to low temperatures, both the Cr³⁺ signal and Ti³⁺ signal reappeared. The photochemically added electron did not reduce Cr³⁺ to a lower oxidation state. Instead, it was found through power saturation experiments and line width analyses, that a cross relaxation mechanism between Ti³⁺ and Cr³⁺ was responsible. The linewidth analysis provided the spin-spin relaxation time, T₂ and the power saturation experiments provided P₂, the product of T₁ and T₂. The spin-lattice relaxation time, T₁ could then be

calculated. The linewidth analysis yielded a $T_2 \approx 18$ ns and the power saturation experiments provided the spin-lattice relaxation time, $T_1 \approx 150$ μ s in the absence of Ti^{3+} . In the presence of Ti^{3+} , T_1 was calculated to be 70 μ s. The decrease in the calculated T_1 time in the presence of Ti^{3+} shows that Ti^{3+} is cross-relaxing Cr^{3+} , explaining why the Cr^{3+} EPR signal disappeared at room temperature.

Insight into dopant incorporation of two dopant ions, Cr and Mn and the corresponding defects were studied in a colloidal $SrTiO_3$ NC following a modified hydrothermal synthesis. Different defects were observed depending on whether a dopant was used, if hydrazine was used or when $SrTiO_3$ was photo-irradiated. The ICP data showed an increase in the concentration of Cr^{3+} when hydrazine was used compared to when hydrazine was omitted during the synthesis. The correlation between dopant incorporation and hydrazine use is evident, but the nature of hydrazine is still unknown. Literature reports simply state the importance of the use of hydrazine in the hydrothermal synthesis to only have structural influences. The use of hydrazine was reported to have control over individual nanocube formation and without it, only irregular large aggregated particles were formed. The results of this work showed there may also be electronic influences on $SrTiO_3$ with the use of hydrazine evidence from the different defects observed. Hydrazine is a known reducing agent and oxygen scavenger. The use of hydrazine could be creating an oxygen deficient environment, favorable for oxygen vacancy formation. The extent or validity of this oxygen vacancy formation mechanism is unclear and would bring light into increasing dopant or oxygen vacancy incorporation to $SrTiO_3$. Looking into the role hydrazine plays during the synthesis would provide further understanding on defect formation when doping colloidal $SrTiO_3$.

Photo-induced electrons play a huge role in the chemical reactions behind photocatalysis. Modulating the defects or dopants is important for the functionality of the material and its designated application. Photodoping is one way to probe the nature of dopants and defects in colloidal NCs. Photodoping Cr-doped SrTiO₃ showed interesting spin-based phenomena that were reversible only through light and air. A cross relaxation mechanism between localized Cr³⁺ dopants and Ti³⁺ was found to dominate at room temperature. Applying this cross-relaxation mechanism to other isovalent and heterovalent such as manganese for the generality of the cross relaxation mechanism would allow a better understanding of the extent of this observed spin-based phenomena. Mn is a widely used dopant for magnetic applications in spin-based systems. To be able to modulate the relaxation time in this system is a step forward in spintronics. The photodoping of electrons to form Ti³⁺ would be a facile and reversible way to exhibit control over the spin relaxation dynamics.

The problem with photodoping is the need for air free to observe the effect due to the detriment of holes for long relaxation times. The use of La³⁺ doping could potentially facilitate long spin relaxation times due to the introduction of free carriers without holes. Reports with other n-type dopants such as Nb⁵⁺ indicate a reversible temperature-dependent switch between free charge carriers and localization of conduction band electrons on Ti⁴⁺ forming Ti³⁺. La³⁺, another n-type dopant, could facilitate a similar effect without competition for doping at the same site as Nb⁵⁺. Therefore, co-doping La³⁺ and Cr³⁺ could allow a temperature dependent modulation over spin dynamics in air compared to the limitations of anaerobic photodoping mentioned earlier. Apart from focusing on modulating spin dynamics in these La, Cr co-doped systems, another direction is to better

understand the differences in dopant induced defects for donor dopants compared to the aliovalent acceptor dopants Cr and Mn that have been focused on thus far. Donor dopants such as La^{3+} or Nb^{5+} inject extra electrons into the lattice or form strontium vacancies as charge compensation when La^{3+} substitutes for Sr^{2+} and Nb^{5+} substitutes for Ti^{4+} in SrTiO_3 . As such, the defects introduced should differ from the acceptor dopants previously studied. It is still uncertain whether ion vacancies form in these colloidal NCs compared to the bulk analogs. In the event ion vacancies do not form, the extra positive charge would have to be compensated by injecting an extra electron. The electrons injected through from charge compensation mechanisms for La^{3+} or Nb^{5+} doping should behave differently compared to photodoped electrons as seen in this study. Investigating co-doping an A-site dopant such as La^{3+} simultaneously with a B-site dopant already well studied, Cr^{3+} should self-compensate itself with no further need for other defects. The use of La^{3+} could potentially function the same way as hydrazine in the synthesis and increase the amount of Cr incorporated into the NCs, giving more control over doping efficiency.

BIBLIOGRAPHY

- Alvarado, S. F.; La Mattina, F.; Bednorz, J. G., Electroluminescence in SrTiO₃:Cr single-crystal nonvolatile memory cells. *Appl. Phys. A* **2007**, *89* (1), 85-89.
- Awschalom, D. D.; Kikkawa, J. M., Electron Spin and Optical Coherence in Semiconductors. *Phys. Today* **1999**, *52* (6), 33-38.
- Azamat, D. V.; Dejneka, A.; Lancok, J.; Trepakov, V. A.; Jastrabik, L.; Badalyan, A. G., Pulse-electron paramagnetic resonance of Cr³⁺ centers in SrTiO₃. *J. Appl. Phys.* **2013**, *113*, 174106.
- Azzoni, C. B.; Mozzati, M. C.; Paleari, A.; Massarotti, V.; Bini, M.; Capsoni, D., Magnetic evidence of different environments of manganese ions in Mn-substituted strontium titanate. *Solid State Commun.* **2000**, *114* (12), 617-622.
- Badalyan, A. G.; Azamat, D.; Babunts, R. A.; Neverova, E. V.; Dejneka, A.; Trepakov, V. A.; Jastrabik, L. EPR study of charge compensation of chromium centers in the strontium titanate crystal. *Phys. Solid State* **2013**, *55*, 1454-1458.
- Badalyan, A. G.; Azzoni, C. B.; Galinetto, P.; Mozzati, M. C.; Trepakov, V. A.; Savinov, M.; Deyneka, A.; Jastrabik, L.; Rosa, J., Impurity centers and host microstructure in weakly doped SrTiO₃:Mn crystals: new findings. *J Phys. Conf. Ser.* **2007**, *93*.
- Badalyan, A. G.; Syrnikov, P. P.; Azzoni, C. B.; Galinetto, P.; Mozzati, M. C.; Rosa, J.; Trepakov, V. A.; Jastrabik, L., Manganese oxide nanoparticles in SrTiO₃:Mn. *J. Appl. Phys.* **2008**, *104* (3).
- Bahnemann, D.; Henglein, A.; Lilie, J.; Spanhel, L., Flash photolysis observation of the absorption spectra of trapped positive holes and electrons in colloidal titanium dioxide. *J. Phys. Chem.* **1984**, *88*, 709-711.
- Baibich, M. N.; Broto, J. M.; Fert, A.; Nguyen Van Dau, F.; Petroff, F.; Etienne, P.; Creuzet, G.; Friederich, A.; Chazelas, J., Giant magnetoresistance of (001) Fe/(001) Cr magnetic superlattices. *Phys. Rev. Lett.* **1988**, *61* (21), 2472-2475.
- Balachandran, U., Electrical Conductivity in Lanthanum-Doped Strontium Titanate. *J. Electrochem. Soc.* **1982**, *129* (5).
- Balaya, P.; Ahrens, M.; Kienle, L.; Maier, J.; Rahmati, B.; Lee, S. B.; Sigle, W.; Pashkin, A.; Kuntscher, C.; Dressel, M., Synthesis and Characterization of Nanocrystalline SrTiO₃. *J. Am. Ceram. Soc.* **2006**, *0* (0), 2804-2811.

- Barnaś, J.; Fuss, A.; Camley, R. E.; Grünberg, P.; Zinn, W., Novel magnetoresistance effect in layered magnetic structures: Theory and experiment. *Phys. Rev. B* **1990**, *42* (13), 8110-8120.
- Baumert, B. A.; Chang, L. H.; Matsuda, A. T.; Tsai, T. L.; Tracy, C. J.; Gregory, R. B.; Fejes, P. L.; Cave, N. G.; Chen, W.; Taylor, D. J.; Otsuki, T.; Fujii, E.; Hayashi, S.; Suu, K., Characterization of sputtered barium strontium titanate and strontium titanate-thin films. *J. Appl. Phys.* **1997**, *82* (5), 2558-2566.
- Beaulac, R.; Schneider, L.; Archer, P. I.; Bacher, G.; Gamelin, D. R., Light-induced spontaneous magnetization in doped colloidal quantum dots. *Science* **2009**, *325*, 973-976.
- Berezovsky, J.; Mikkelsen, M. H.; Stoltz, N. G.; Coldren, L. A.; Awschalom, D. D., Picosecond coherent optical manipulation of a single electron spin in a quantum dot. *Science* **2008**, *320*, 349-352.
- Binnig, G.; Baratoff, A.; Hoenig, H. E.; Bednorz, J. G., Two-Band Superconductivity in Nb-Doped SrTiO₃. *Phys. Rev. Lett.* **1980**, *45* (16), 1352-1355.
- Blasse, G.; de Korte, P. H. M.; Mackor, A., The colouration of titanates by transition-metal ions in view of solar energy applications. *J. Inorg. Nucl. Chem.* **1981**, *43*, 1499-1503.
- Böttcher, R.; Klimm, C.; Michel, D.; Semmelhack, H. C.; Völkel, G.; Gläsel, H. J.; Hartmann, E., Size effect in Mn²⁺-doped BaTiO₃ nanopowders observed by electron paramagnetic resonance. *Phys. Rev. B* **2000**, *62* (3), 2085-2095.
- Brozek, C. K.; Zhou, D. M.; Liu, H. B.; Li, X. S.; Kittilstved, K. R.; Gamelin, D. R., Soluble Supercapacitors: Large and Reversible Charge Storage in Colloidal Iron-Doped ZnO Nanocrystals. *Nano Lett.* **2018**, *18*, 3297-3302.
- Brykhar, Z.; Trepakov, V.; Potůček, Z.; Jastrabík, L., Luminescence spectra of SrTiO₃:Mn⁴⁺. *J. Lumin.* **2000**, *87-89*, 605-607.
- Bykov, I.; Makarova, M.; Trepakov, V.; Dejneka, A.; Yurchenko, L.; Yurchenko, L.; Jäger, A.; Jastrabík, L. Intrinsic and Impurity Defects in Chromium-doped SrTiO₃ Nanopowders: EPR and NMR Study. *Phys. Status Solidi B* **2013**, *250*, 821-824.
- Cerletti, V.; Coish, W. A.; Gywat, O.; Loss, D., Recipes for spin-based quantum computing. *Nanotechnology* **2005**, *16* (4), R27-R49.
- Chen, D.; Jiao, X.; Zhang, M., Hydrothermal synthesis of strontium titanate powders with nanometer size derived from different precursors. *J. Eu. Ceram. Soc.* **2000**, *20* (9), 1261-1265.

- Choudhury, D.; Mukherjee, S.; Mandal, P.; Sundaresan, A.; Waghmare, U. V.; Bhattacharjee, S.; Mathieu, R.; Lazor, P.; Eriksson, O.; Sanyal, B.; Nordblad, P.; Sharma, A.; Bhat, S. V.; Karis, O.; Sarma, D. D., Tuning of dielectric properties and magnetism of SrTiO₃ by site-specific doping of Mn. *Phys. Rev. B* **2011**, *84* (12).
- Choudhury, D.; Pal, B.; Sharma, A.; Bhat, S. V.; Sarma, D. D., Magnetization in electron- and Mn-doped SrTiO₃. *Sci. Rep.* **2013**, *3*, 1433.
- Clark, S. M.; Fu, K. M.; Ladd, T. D.; Yamamoto, Y., Quantum computers based on electron spins controlled by ultrafast off-resonant single optical pulses. *Phys. Rev. Lett.* **2007**, *99*, 040501.
- Coey, J. M. D.; Viret, M.; von Molnár, S., Mixed-valence manganites. *Adv. Phys.* **1999**, *48* (2), 167-293.
- Crooker, S. A.; Awschalom, D. D.; Baumberg, J. J.; Flack, F.; Samarth, N., Optical spin resonance and transverse spin relaxation in magnetic semiconductor quantum wells. *Phys. Rev. B* **1997**, *56* (12), 7574-7588.
- Crooker, S. A.; Baumberg, J. J.; Flack, F.; Samarth, N.; Awschalom, D. D., Terahertz Spin Precession and Coherent Transfer of Angular Momenta in Magnetic Quantum Wells. *Phys. Rev. Lett.* **1996**, *77* (13), 2814-2817.
- da Silva, L. F.; Avansi, W.; Andres, J.; Ribeiro, C.; Moreira, M. L.; Longo, E.; Mastelaro, V. R., Long-range and short-range structures of cube-like shape SrTiO₃ powders: microwave-assisted hydrothermal synthesis and photocatalytic activity. *Phys. Chem. Chem. Phys.* **2013**, *15* (29), 12386-93.
- Dang, F.; Mimura, K.-i.; Kato, K.; Imai, H.; Wada, S.; Haneda, H.; Kuwabara, M. Growth of Monodispersed SrTiO₃ Nanocubes by Thermohydrolysis Method. *Cryst. Eng. Comm.* **2011**, *13*, 3878-3883.
- Das Sarma, S.; Fabian, J.; Hu, X.; Žutić, I., Spintronics: electron spin coherence, entanglement, and transport. *Superlattices Microstruct.* **2000**, *27* (5-6), 289-295.
- De Trizio, L.; Buonsanti, R.; Schimpf, A. M.; Llordes, A.; Gamelin, D. R.; Simonutti, R.; Milliron, D. J., Nb-Doped Colloidal TiO₂ Nanocrystals with Tunable Infrared Absorption. *Chem. Mater.* **2013**, *25*, 3383-3390.
- Eden, S.; Kapphan, S.; Hesse, H.; Trepakov, V.; Vikhnin, V.; Gregora, I.; Jastrabik, L.; Seglins, J. Observations of the Absorption, Infra-red Emission, and Excitation Spectra of Cr in BaTiO₃. *J. Phys.: Condens. Matter* **1998**, *10*, 10775-10786.

- Enterkin, J. A.; Subramanian, A. K.; Russell, B. C.; Castell, M. R.; Poepelmeier, K. R.; Marks, L. D., A homologous series of structures on the surface of SrTiO₃ (110). *Nat. Mater.* **2010**, *9* (3), 245-8.
- Ertekin, E.; Srinivasan, V.; Ravichandran, J.; Rossen, P. B.; Siemons, W.; Majumdar, A.; Ramesh, R.; Grossman, J. C., Interplay between intrinsic defects, doping, and free carrier concentration in SrTiO₃ thin films. *Phys. Rev. B* **2012**, *85* (19).
- Erwin, S. C.; Zu, L.; Haftel, M. I.; Efros, A. L.; Kennedy, T. A.; Norris, D. J., Doping semiconductor nanocrystals. *Nature* **2005**, *436* (7047), 91-4.
- Fabian, J.; Sarma, S. D., Spin relaxation of conduction electrons. *J. Vac. Sci. Technol., B*: **1999**, *17* (4).
- Fujinami, K.; Katagiri, K.; Kamiya, J.; Hamanaka, T.; Koumoto, K., Sub-10 nm strontium titanate nanocubes highly dispersed in non-polar organic solvents. *Nanoscale* **2010**, *2* (10), 2080-3.
- Furdyna, J. K., Diluted magnetic semiconductors. *J. Appl. Phys.* **1988**, *64* (4), R29-R64.
- Ghosh, S.; Sih, V.; Lau, W. H.; Awschalom, D. D.; Bae, S. Y.; Wang, S.; Vaidya, S.; Chapline, G., Room-temperature spin coherence in ZnO. *Appl. Phys. Lett.* **2005**, *86* (23).
- Guo, Y. Y.; Liu, H. M.; Yu, D. P.; Liu, J. M. Ferroelectricity and Superparamagnetism in Sr/Ti Nonstoichiometric SrTiO₃. *Phys. Rev. B* **2012**, *85*, 104108.
- Hanson, R.; Awschalom, D. D., Coherent manipulation of single spins in semiconductors. *Nature* **2008**, *453* (7198), 1043-9.
- Hanzig, J.; Abendroth, B.; Hanzig, F.; Stöcker, H.; Strohmeyer, R.; Meyer, D. C.; Lindner, S.; Grobosch, M.; Knupfer, M.; Himcinschi, C.; Mühle, U.; Munnik, F., Single crystal strontium titanate surface and bulk modifications due to vacuum annealing. *J. Appl. Phys.* **2011**, *110* (6).
- Hao, X.; Wang, Z.; Schmid, M.; Diebold, U.; Franchini, C., Coexistence of trapped and free excess electrons in SrTiO₃. *Phys. Rev. B* **2015**, *91*, 085204.
- Harrigan, W. L.; Michaud, S. E.; Lehuta, K. A.; Kittilstved, K. R., Tunable Electronic Structure and Surface Defects in Chromium-Doped Colloidal SrTiO_{3-δ} Nanocrystals. *Chem. Mater.* **2016**, *28* (2), 430-433.
- Henglein, A., Colloidal TiO₂ Catalyzed Photo- and Radiation Chemical Processes in Aqueous Solution. *Ber. Bunsenges. Phys. Chem.* **1982**, *86*, 241-246.

- Hermenau, J.; Ternes, M.; Steinbrecher, M.; Wiesendanger, R.; Wiebe, J., Long Spin-Relaxation Times in a Transition-Metal Atom in Direct Contact to a Metal Substrate. *Nano Lett.* **2018**, *18* (3), 1978-1983.
- Howe, R. F.; Grätzel, M., EPR observation of trapped electrons in colloidal titanium dioxide. *J. Phys. Chem.* **1985**, *89*, 4495-4499.
- Huang, Y.; Lü, H.; Guo, H.; Liu, L.; He, M.; Chen, Z.; Zhou, Y.; Zhao, K.; Jin, K.; Yang, G., Structure and electrical characteristics of Nb-doped SrTiO₃ substrates. *Chin. Sci. Bull.* **2006**, *51* (16), 2035-2037.
- Imamoğlu, A.; Awschalom, D. D.; Burkard, G.; DiVincenzo, D. P.; Loss, D.; Sherwin, M.; Small, A., Quantum Information Processing Using Quantum Dot Spins and Cavity QED. *Phys. Rev. Lett.* **1999**, *83*, 4204-4207.
- Ivanov, V. A.; Aminov, T. G.; Novotortsev, V. M.; Kalinnikov, V. T., Spintronics and spintronics materials. *Russ. Chem. Bull.* **2004**, *53* (11), 2357-2405.
- Iwase, A.; Ng, Y. H.; Ishiguro, Y.; Kudo, A.; Amal, R. Reduced Graphene Oxide as a Solid-State Electron Mediator in Z-Scheme Photocatalytic Water Splitting under Visible Light. *J. Am. Chem. Soc.* **2011**, *133*, 11054-11057.
- Jalan, B.; Engel-Herbert, R.; Mates, T. E.; Stemmer, S., Effects of hydrogen anneals on oxygen deficient SrTiO_{3-x} single crystals. *Appl. Phys. Lett.* **2008**, *93* (5).
- Janotti, A.; Franchini, C.; Varley, J. B.; Kresse, G.; Van de Walle, C. G., Dual behavior of excess electrons in rutile TiO₂. *Phys. Status Solidi RRL* **2013**, *7*, 199-203.
- Janousch, M.; Meijer, G. I.; Staub, U.; Delley, B.; Karg, S. F.; Andreasson, B. P. Role of Oxygen Vacancies in Cr-Doped SrTiO₃ for Resistance-Change Memory. *Adv. Mater.* **2007**, *19*, 2232-2235.
- Ju, L.; Sabergharesou, T.; Stamplecoskie, K. G.; Hegde, M.; Wang, T.; Combe, N. A.; Wu, H.; Radovanovic, P. V. Interplay between Size, Composition, and Phase Transition of Nanocrystalline Cr³⁺-doped BaTiO₃ as a Path to Multiferroism in Perovskite-Type Oxides. *J. Am. Chem. Soc.* **2011**, *134*, 1136-1146.
- Kan, D.; Kanda, R.; Kanemitsu, Y.; Shimakawa, Y.; Takano, M.; Terashima, T.; Ishizumi, A., Blue luminescence from electron-doped SrTiO₃. *Appl. Phys. Lett.* **2006**, *88* (19).
- Kang, H. W.; Park, S. B., H₂ evolution under visible light irradiation from aqueous methanol solution on SrTiO₃:Cr/Ta prepared by spray pyrolysis from polymeric precursor. *Int. J. Hydrogen Energy* **2011**, *36* (16), 9496-9504.

- Kato, H.; Kudo, A., Visible-Light-Response and Photocatalytic Activities of TiO₂ and SrTiO₃ Photocatalysts Codoped with Antimony and Chromium. *J. Phys. Chem. B* **2002**, *106* (19), 5029-5034.
- Khomenko, V. M.; Langer, K.; Rager, H.; Fett, A., Electronic absorption by Ti³⁺ ions and electron delocalization in synthetic blue rutile. *Phys. Chem. Minerals* **1998**, *25*, 338-346.
- Kolbe, W., Spin Relaxation Time of Conduction Electrons in Bulk Sodium Metal. *Phys. Rev. B* **1971**, *3* (2), 320-323.
- Kölle, U.; Moser, J.; Grätzel, M., Dynamics of interfacial charge-transfer reactions in semiconductor dispersions. Reduction of cobaltoceniumdicarboxylate in colloidal titania. *Inorg. Chem.* **1985**, *24*, 2253-2258.
- Kolodiazhnyi, T.; Petric, A., The Applicability of Sr-deficient n-type SrTiO₃ for SOFC Anodes. *J. Electroceram.* **2005**, *15* (1), 5-11.
- Konta, R.; Ishii, T.; Kato, H.; Kudo, A., Photocatalytic Activities of Noble Metal Ion Doped SrTiO₃ under Visible Light Irradiation. *J. Phys. Chem. B* **2004**, *108* (26), 8992-8995.
- Kou, J.; Gao, J.; Li, Z.; Yu, H.; Zhou, Y.; Zou, Z. Construction of Visible-Light-Responsive SrTiO₃ with Enhanced CO₂ Adsorption Ability: Highly Efficient Photocatalysts for Artificial Photosynthesis. *Catal. Lett.* **2014**, *145*, 640-646.
- Kozuka, Y.; Kim, M.; Ohta, H.; Hikita, Y.; Bell, C.; Hwang, H. Y., Enhancing the electron mobility via delta-doping in SrTiO₃. *Appl. Phys. Lett.* **2010**, *97* (22).
- Kutty, T. R. N. D., L. G.; Murugaraj, P. , The Change in Oxidation State of Mn Ions in Semiconducting BaTiO₃ and SrTiO₃ around the Phase Transition Temperatures. *Mater. Res. Bull.* **1986**, *21*, 1093-1102.
- La Mattina, F.; Bednorz, J. G.; Alvarado, S. F.; Shengelaya, A.; Müller, K. A.; Keller, H. Controlled Oxygen Vacancies and Space Correlation with Cr³⁺ in SrTiO₃. *Phys. Rev. B* **2009**, *80*, 075122.
- Laguta, V. V.; Kondakova, I. V.; Bykov, I. P.; Glinchuk, M. D.; Tkach, A.; Vilarinho, P. M.; Jastrabik, L., Electron spin resonance investigation of Mn₂₊ ions and their dynamics in Mn-doped SrTiO₃. *Phys. Rev. B* **2007**, *76* (5).
- Lehuta, K. A.; Haldar, A.; Zhou, D.; Kittilstved, K. R., Spectroscopic Study of the Reversible Chemical Reduction and Reoxidation of Substitutional Cr Ions in Sr₂TiO₄. *Inorg. Chem.* **2017**, *56*, 9177-9184.

- Lehuta, K. A.; Kittilstved, K. R. Speciation of Cr(III) in Intermediate Phases During the Sol–Gel Processing of Cr-doped SrTiO₃ Powders. *J. Mater. Chem. A* **2014**, *2*, 6138-6145.
- Lehuta, K. A.; Kittilstved, K. R., Reversible control of the chromium valence in chemically reduced Cr-doped SrTiO₃ bulk powders. *Dalton. Trans.* **2016**, *45*, 10034-10041.
- Leonelli, R.; Brebner, J. L. Time-resolved Spectroscopy of the Visible Emission Band in Strontium Titanate. *Phys. Rev. B* **1986**, *33*, 8649-8656.
- Li, H.; Yin, S.; Wang, Y.; Sekino, T.; Lee, S. W.; Sato, T., Roles of Cr³⁺ doping and oxygen vacancies in SrTiO₃ photocatalysts with high visible light activity for NO removal. *J. Catal.* **2013**, *297*, 65-69.
- Lin, Y.; Wen, J.; Hu, L.; McCarthy, J. A.; Wang, S.; Poepelmeier, K. R.; Marks, L. D., Electron-induced Ti-rich surface segregation on SrTiO₃ nanoparticles. *Micron.* **2015**, *68*, 152-7.
- Liu, W. K.; Whitaker, K. M.; Kittilstved, K. R.; Gamelin, D. R. Stable Photogenerated Carriers in Magnetic Semiconductor Nanocrystals. *J. Am. Chem. Soc.* **2006**, *128*, 3910-3911.
- Lunsford, J. H. ESR of Adsorbed Oxygen Species. *Catal. Rev.* **1974**, *8*, 135-157.
- Lunsford, J. H., ESR of Adsorbed Oxygen Species. *Catal. Rev.* **2006**, *8* (1), 135-157.
- Magarill, L. I.; Chaplik, A. V.; Éntin, M. V., Spin response of 2D electrons to a lateral electric field. *Semiconductors* **2001**, *35* (9), 1081-1087.
- Manenkov, A. A.; Prokhorov, A. M., Spin-lattice relaxation and cross-relaxation interactions in chromium corundum. *Sov. Phys. JETP* **1962**, *15*, 54-59.
- Manenkov, A. A.; Prokhorov, A. M., Spin-lattice relaxation in chromium corundum. *Sov. Phys. JETP* **1960**, *11*, 527-530.
- Matsumoto, Y., Room-Temperature Ferromagnetism in Transparent Transition Metal-Doped Titanium Dioxide. *Science* **2001**, *291* (5505), 854-856.
- Mavroides, J. G.; Kafalas, J. A.; Kolesar, D. F. Photoelectrolysis of Water in Cells with SrTiO₃ Anodes. *Appl. Phys. Lett.* **1976**, *28*, 241-243.
- McClure, D. S. Comparison of the Crystal Fields and Optical Spectra of Cr₂O₃ and Ruby. *J. Chem. Phys.* **1963**, *38*, 2289-2294.

- Meijer, G. I.; Staub, U.; Janousch, M.; Johnson, S. L.; Delley, B.; Neisius, T. Valence States of Cr and the Insulator-to-Metal Transition in Cr-doped SrTiO₃. *Phys. Rev. B* **2005**, *72*, 155102.
- Meyer, R.; Zurhelle, A. F.; De Souza, R. A.; Waser, R.; Gunkel, F., Dynamics of the metal-insulator transition of donor-doped SrTiO₃. *Phys. Rev. B* **2016**, *94* (11).
- Mims, W. B.; McGee, J. D., Cross Relaxation in Ruby. *Phys. Rev.* **1960**, *119*, 1233-1237.
- Mitra, C.; Lin, C.; Robertson, J.; Demkov, A. A., Electronic structure of oxygen vacancies in SrTiO₃ and LaAlO₃. *Phys. Rev. B* **2012**, *86*, 155105.
- Mochizuki, S.; Minami, S.; Fujishiro, F., The reversible UV-laser-light-induced spectral change and origin of the 2.4eV luminescence band in SrTiO₃. *J. Lumin.* **2005**, *112* (1-4), 267-270.
- Moos, R.; Bischoff, T.; Menesklou, W.; Hardtl, K. H., Solubility of lanthanum in strontium titanate in oxygen-rich atmospheres. *J. Mater. Sci.* **1997**, *32* (16), 4247-4252.
- Moos, R.; Hardtl, K. H., Defect Chemistry of Donor-Doped and Undoped Strontium Titanate Ceramics between 1000° and 1400°C. *J. Am. Ceram. Soc.* **2005**, *80* (10), 2549-2562.
- Müller, K. A. In *Proceedings of the First International Conference I, Paramagnetic Resonance*; Low, W., Ed.; Academic Press: New York, 1963; pp 17–43.
- Müller, K. A., hyperfine and g-values for Cr³⁺ in SrTiO₃. In *Proceedings of the First International Conference I, Paramagnetic Resonance*, Low, W., Ed. Academic Press: New York, 1963; p 17.
- Müller, K. A.; Berlinger, W.; Rubins, R. S., Observation of Two Charged States of a Nickel-Oxygen Vacancy Pair in SrTiO₃ by Paramagnetic Resonance. *Phys. Rev.* **1969**, *186* (2), 361-371.
- Naccache, C.; Meriaudeau, P.; Che, M.; Tench, A. J. Identification of Oxygen Species Adsorbed on Reduced Titanium Dioxide. *Trans. Faraday Soc.* **1971**, *67*, 506-512.
- Neagu, D.; Irvine, J. T. S., Enhancing Electronic Conductivity in Strontium Titanates through Correlated A and B-Site Doping. *Chem. Mater.* **2011**, *23* (6), 1607-1617.
- Nisida, Y., Spin-Lattice Relaxation of Cr³⁺ in Coexistence with Ti³⁺ in Al₂O₃. *J. Phys. Soc. Japan* **1965**, *20*, 1390-1399.
- Ochsenbein, S. T.; Feng, Y.; Whitaker, K. M.; Badaeva, E.; Liu, W. K.; Li, X. S.; Gamelin, D. R., Charge-controlled magnetism in colloidal doped semiconductor nanocrystals. *Nat. Nanotechnol.* **2009**, *4*, 681-687.

- Ohno, Y.; Young, D. K.; Beschoten, B.; Matsukura, F.; Ohno, H.; Awschalom, D. D., Electrical spin injection in a ferromagnetic semiconductor heterostructure. *Nature* **1999**, *402* (6763), 790-792.
- Ohtomo, A.; Hwang, H. Y. A High-Mobility Electron Gas at the LaAlO₃/SrTiO₃ Heterointerface. *Nature* **2004**, *427*, 423-426.
- Ouyang, S.; Tong, H.; Umezawa, N.; Cao, J.; Li, P.; Bi, Y.; Zhang, Y.; Ye, J., Surface-alkalinization-induced enhancement of photocatalytic H₂ evolution over SrTiO₃-based photocatalysts. *J. Am. Chem. Soc.* **2012**, *134* (4), 1974-7.
- Park, K.; Son, J. S.; Woo, S. I.; Shin, K.; Oh, M.-W.; Park, S.-D.; Hyeon, T. Colloidal Synthesis and Thermoelectric Properties of La-doped SrTiO₃ Nanoparticles. *J. Mater. Chem. A* **2014**, *2*, 4217-4224.
- Park, N.-H.; Wang, Y.; Seo, W.-S.; Dang, F.; Wan, C.; Koumoto, K., Solution synthesis and growth mechanism of SrTiO₃ mesocrystals. *Cryst. Eng. Comm.* **2013**, *15* (4), 679-685.
- Peper, J. L.; Vinyard, D. J.; Brudvig, G. W.; Mayer, J. M., Slow Equilibration between Spectroscopically Distinct Trap States in Reduced TiO₂ Nanoparticles. *J. Am. Chem. Soc.* **2017**, *139*, 2868-2871.
- Potáek, Z.; Trepakov, V.; Deyneka, A.; Bryknar, Z.; Galinetto, P.; Rossella, F., Luminescence and Absorption Spectroscopy of Weakly Mn-Doped SrTiO₃ Crystals. *Ferroelectrics* **2008**, *367* (1), 102-110.
- Prinz, G. A., Magnetoelectronics. *Science* **1998**, *282* (5394), 1660-1663.
- Rasband, W. S., ImageJ, U. S. National Institutes of Health, Bethesda, Maryland, USA, <http://imagej.nih.gov/ij/>, 1997-2015.
- Reunchan, P.; Ouyang, S.; Umezawa, N.; Xu, H.; Zhang, Y.; Ye, J., Theoretical design of highly active SrTiO₃-based photocatalysts by a codoping scheme towards solar energy utilization for hydrogen production. *J. Mater. Chem. A* **2013**, *1* (13).
- Reunchan, P.; Umezawa, N.; Ouyang, S.; Ye, J., Mechanism of photocatalytic activities in Cr-doped SrTiO₃ under visible-light irradiation: an insight from hybrid density-functional calculations. *Phys. Chem. Chem. Phys.* **2012**, *14* (6), 1876-80.
- Rice, W. D.; Ambwani, P.; Bombeck, M.; Thompson, J. D.; Haugstad, G.; Leighton, C.; Crooker, S. A. Persistent Optically Induced Magnetism in Oxygen-Deficient Strontium Titanate. *Nat. Mater.* **2014**, *13*, 481-487.

- Roduner, E., Size matters: why nanomaterials are different. *Chem. Soc. Rev.* **2006**, *35* (7), 583-92.
- Rubano, A.; Paparo, D.; Granozio, F. M.; Scotti di Uccio, U.; Marrucci, L., Blue luminescence of SrTiO₃ under intense optical excitation. *J. Appl. Phys.* **2009**, *106* (10).
- Salje, E. K. H.; Gallardo, M. C.; Jiménez, J.; Romero, F. J.; Cerro, J. d., The cubic-tetragonal phase transition in strontium titanate: excess specific heat measurements and evidence for a near-tricritical, mean field type transition mechanism. *J. Phys.: Condens. Matter.* **1998**, *10* (25), 5535-5543.
- Santander-Syro, A. F.; Fortuna, F.; Bareille, C.; Rodel, T. C.; Landolt, G.; Plumb, N. C.; Dil, J. H.; Radovic, M. Giant Spin Splitting of the Two-dimensional Electron Gas at the Surface of SrTiO₃. *Nat. Mater.* **2014**, *13*, 1085-1090.
- Sasaki, Y.; Nemoto, H.; Saito, K.; Kudo, A. Solar Water Splitting Using Powdered Photocatalysts Driven by Z-Schematic Interparticle Electron Transfer without an Electron Mediator. *J. Phys. Chem. C* **2009**, *113*, 17536-17542.
- Schimpf, A. M.; Gunthardt, C. E.; Rinehart, J. D.; Mayer, J. M.; Gamelin, D. R., Controlling Carrier Densities in Photochemically Reduced Colloidal ZnO Nanocrystals: Size Dependence and Role of the Hole Quencher. *J. Am. Chem. Soc.* **2013**, *135*, 16569-16577.
- Schimpf, A. M.; Ochsenbein, S. T.; Gamelin, D. R., Surface Contributions to Mn²⁺ Spin Dynamics in Colloidal Doped Quantum Dots. *J. Phys. Chem. Lett.* **2015**, *6*, 457-463.
- Schimpf, A. M.; Rinehart, J. D.; Ochsenbein, S. T.; Gamelin, D. R., Charge-State Control of Mn²⁺ Spin Relaxation Dynamics in Colloidal n-Type Zn_{1-x}Mn_xO Nanocrystals. *J. Phys. Chem. Lett.* **2015**, *6*, 1748-1753.
- Schimpf, A. M.; Thakkar, N.; Gunthardt, C. E.; Masiello, D. J.; Gamelin, D. R., Charge-Tunable Quantum Plasmons in Colloidal Semiconductor Nanocrystals. *ACS Nano* **2014**, *8*, 1065-1072.
- Schooley, J. F.; Hosler, W. R.; Cohen, M. L., Superconductivity in Semiconducting SrTiO₃. *Phys. Rev. Lett.* **1964**, *12* (17), 474-475.
- Schrauben, J. N.; Hayoun, R.; Valdez, C. N.; Braten, M.; Fridley, L.; Mayer, J. M., Titanium and zinc oxide nanoparticles are proton-coupled electron transfer agents. *Science* **2012**, *336*, 1298-1301.

- Serway, R. A.; Berlinger, W.; Müller, K. A.; Collins, R. W., Electron paramagnetic resonance of three manganese centers in reduced SrTiO₃. *Phys. Rev. B* **1977**, *16* (11), 4761-4768.
- Shim, M.; Guyot-Sionnest, P., n-type colloidal semiconductor nanocrystals. *Nature* **2000**, *407*, 981-983.
- Šimánek, E., Müller, K. A., Covalency and Hyperfine Structure constant A of Iron group Impurities in Crystals. *J. Phys. Chem. Solids* **1970**, *31*, 1027-1040.
- Soria, J.; Sanz, J.; Sobrados, I.; Coronado, J. M.; Fresno, F.; Hernández-Alonso, M. D. Magnetic Resonance Study of the Defects Influence on the Surface Characteristics of Nanosize Anatase. *Catal. Today* **2007**, *129*, 240-246.
- Stokowski, S.; Schawlow, A. Dielectric-Related Optical Line Shifts in SrTiO₃:Cr³⁺. *Phys. Rev.* **1969**, *178*, 464-470.
- Stokowski, S.; Schawlow, A. Spectroscopic Studies of SrTiO₃ Using Impurity-Ion Probes. *Phys. Rev.* **1969**, *178*, 457-464.
- Sun, X.; Lin, J., Synergetic Effects of Thermal and Photo-Catalysis in Purification of Dye Water over SrTi_{1-x}Mn_xO₃ Solid Solutions. *J. Phys. Chem. C* **2009**, *113* (12), 4970-4975.
- Szot, K.; Speier, W., Surfaces of reduced and oxidized SrTiO₃ from atomic force microscopy. *Phys. Rev. B* **1999**, *60* (8), 5909-5926.
- Szot, K.; Speier, W.; Carius, R.; Zastrow, U.; Beyer, W., Localized metallic conductivity and self-healing during thermal reduction of SrTiO₃. *Phys. Rev. Lett.* **2002**, *88* (7), 075508.
- Tan, H.; Zhao, Z.; Zhu, W. B.; Coker, E. N.; Li, B.; Zheng, M.; Yu, W.; Fan, H.; Sun, Z. Oxygen Vacancy Enhanced Photocatalytic Activity of Perovskite SrTiO₃. *ACS Appl. Mater. Interfaces* **2014**, *6*, 19184-19190.
- Ternes, M., Spin excitations and correlations in scanning tunneling spectroscopy. *New J. Phys.* **2015**, *17* (6).
- Tkach, A.; Vilarinho, P. M.; Kholkin, A. L., Dependence of dielectric properties of manganese-doped strontium titanate ceramics on sintering atmosphere. *Acta Mater.* **2006**, *54* (20), 5385-5391.
- Tkach, A.; Vilarinho, P. M.; Kholkin, A. L., Structure–microstructure–dielectric tunability relationship in Mn-doped strontium titanate ceramics. *Acta Mater.* **2005**, *53* (19), 5061-5069.

- Tonda, S.; Kumar, S.; Anjaneyulu, O.; Shanker, V., Synthesis of Cr and La-codoped SrTiO₃ nanoparticles for enhanced photocatalytic performance under sunlight irradiation. *Phys. Chem. Chem. Phys.* **2014**, *16* (43), 23819-28.
- Townsend, T. K.; Browning, N. D.; Osterloh, F. E. Nanoscale Strontium Titanate Photocatalysts for Overall Water Splitting. *ACS Nano* **2012**, *6*, 7420-7426.
- Trepakov, V. A.; Potucek, Z.; Makarova, M. V.; Dejneka, A.; Sazama, P.; Jastrabik, L.; Brykhar, Z. SrTiO₃:Cr Nanocrystalline Powders: Size Effects and Optical Properties. *J. Phys. Condens. Matter* **2009**, *21*, 375303.
- Valant, M.; Kolodiazny, T.; Arčon, I.; Aguesse, F.; Axelsson, A.-K.; Alford, N. M., The Origin of Magnetism in Mn-Doped SrTiO₃. *Adv. Funct. Mater.* **2012**, *22* (10), 2114-2122.
- van Benthem, K.; Elsässer, C.; French, R. H. Bulk Electronic Structure of SrTiO₃: Experiment and Theory. *J. Appl. Phys.* **2001**, *90*, 6156-6164.
- Wan, T.; Qu, B.; Du, H.; Lin, X.; Guan, P.; Lin, Q.; Chen, N.; Teck Tan, T.; Hang, T.; Chu, D., Tunable resistance switching in solution processed chromium-doped strontium titanate nanoparticles films. *J. Colloid Interface Sci.* **2017**, *494*, 178-184.
- Wang, D.; Ye, J.; Kako, T.; Kimura, T. Photophysical and Photocatalytic Properties of SrTiO₃ Doped with Cr Cations on Different Sites. *J. Phys. Chem. B* **2006**, *110*, 15824-15830.
- Wang, X.; Gu, M.; Yang, B.; Zhu, S.; Cao, W., Hall effect and dielectric properties of Mn-doped barium titanate. *Microelectron. Eng.* **2003**, *66* (1-4), 855-859.
- Warusawithana, M. P.; Cen, C.; Sleasman, C. R.; Woicik, J. C.; Li, Y.; Kourkoutis, L. F.; Klug, J. A.; Li, H.; Ryan, P.; Wang, L. P.; Bedzyk, M.; Muller, D. A.; Chen, L. Q.; Levy, J.; Schlom, D. G. A Ferroelectric Oxide Made Directly on Silicon. *Science* **2009**, *324*, 367-370.
- Whitaker, K. M.; Ochsenbein, S. T.; Smith, A. L.; Echodu, D. C.; Robinson, B. H.; Gamelin, D. R., Hyperfine Coupling in Colloidal n-Type ZnO Quantum Dots: Effects on Electron Spin Relaxation. *J. Phys. Chem. C* **2010**, *114*, 14467-14472.
- Wolf, S. A.; Awschalom, D. D.; Buhrman, R. A.; Daughton, J. M.; von Molnar, S.; Roukes, M. L.; Chtchelkanova, A. Y.; Treger, D. M., Spintronics: a spin-based electronics vision for the future. *Science* **2001**, *294* (5546), 1488-95.
- Wolf, S. A.; Chtchelkanova, A. Y.; Treger, D. M., Spintronics—A retrospective and perspective. *IBM J. Res. Dev.* **2006**, *50* (1), 101-110.

- Wrighton, M. S.; Ellis, A. B.; Wolczanski, P. T.; Morse, D. L.; Abrahamson, H. B.; Ginley, D. S. Strontium Titanate Photoelectrodes. Efficient Photoassisted Electrolysis of Water at Zero Applied Potential. *J. Am. Chem. Soc.* **1976**, *98*, 2774-2779.
- Wu, M. W.; Jiang, J. H.; Weng, M. Q., Spin dynamics in semiconductors. *Phys. Rep.* **2010**, *493* (2-4), 61-236.
- Yang, H.; Kan, K.; Ouyang, J.; Li, Y., Solvothermal synthesis and optical properties of Mn²⁺-doped SrTiO₃ powders. *J. Alloys Compd.* **2009**, *485* (1-2), 351-355.
- Yu, H.; Ouyang, S.; Yan, S.; Li, Z.; Yu, T.; Zou, Z., Sol-gel hydrothermal synthesis of visible-light-driven Cr-doped SrTiO₃ for efficient hydrogen production. *J. Mater. Chem.* **2011**, *21* (30).
- Yuan, G. L.; Liu, J. M.; Baba-Kishi, K.; Chan, H. L. W.; Choy, C. L.; Liu, Z. G., Possible mechanism for tunneling magnetoresistance in La_{0.9}Ba_{0.1}MnO₃/Nb-doped SrTiO₃ p-n junctions. *Solid State Commun.* **2004**, *131* (6), 383-387.
- Yumashev, K. V.; Prokoshin, P. V.; Malyarevich, A. M.; Mikhailov, V. P., Transient bleaching/induced absorption in reduced SrTiO₃ under picosecond excitation. *J. Opt. Soc. Am. B: Opt. Phys.* **1997**, *14* (2).
- Zhan, H.; Chen, Z.-G.; Zhuang, J.; Yang, X.; Wu, Q.; Jiang, X.; Liang, C.; Wu, M.; Zou, J., Correlation between Multiple Growth Stages and Photocatalysis of SrTiO₃ Nanocrystals. *J. Phys. Chem. C* **2015**, *119* (7), 3530-3537.
- Zhang, W. F.; Yin, Z.; Zhang, M. S.; Du, Z. L.; Chen, W. C. Roles of Defects and Grain Sizes in Photoluminescence of Nanocrystalline SrTiO₃. *J. Phys.: Condens. Matter* **1999**, *11*, 5655-5660.
- Zhou, X.; Shi, J.; Li, C., Effect of Metal Doping on Electronic Structure and Visible Light Absorption of SrTiO₃ and NaTaO₃ (Metal = Mn, Fe, and Co). *J. Phys. Chem. C* **2011**, *115* (16), 8305-8311.
- Zorko, A.; Pregelj, M.; Luetkens, H.; Axelsson, A. K.; Valant, M., Intrinsic paramagnetism and aggregation of manganese dopants in SrTiO₃. *Phys. Rev. B* **2014**, *89* (9).
- Zuo, F.; Wang, L.; Wu, T.; Zhang, Z.; Borchardt, D.; Feng, P., Self-doped Ti³⁺ enhanced photocatalyst for hydrogen production under visible light. *J Am Chem Soc* **2010**, *132* (34), 11856-7.
- Žutić, I.; Fabian, J.; Das Sarma, S., Spintronics: Fundamentals and applications. *Rev. Mod. Phys.* **2004**, *76* (2), 323-410.